

# Optimal Control of the Strong-Field Laser Ionization of Clusters in Helium Droplets

DISSERTATION

zur Erlangung des akademischen Grades  
*doctor rerum naturalium (Dr. rer. nat.)*  
der Mathematisch-Naturwissenschaftlichen Fakultät  
der Universität Rostock

vorgelegt von

Nguyen Xuan Truong  
aus Hai Duong, Vietnam

Januar 2011

**Universität  
Rostock**



Traditio et Innovatio

Betreuer: Prof. Dr. Karl-Heinz Meiwes-Broer, Univ. Rostock  
Dr. habil. Josef Tiggesbäumker, Univ. Rostock

Gutachter: Prof. Dr. Karl-Heinz Meiwes-Broer, Univ. Rostock  
Prof. Dr. Marc Vrakking, Max-Born-Institut Berlin  
Prof. Dr. Dieter Bauer, Univ. Rostock

Verteidigung: 08.04.2011

*To my dearest Mom and Dad!*



## **Abstract**

The strong-field ionization dynamics of silver and xenon clusters embedded in helium droplets are studied using the femtosecond pulse shaping techniques. By adaptively tailoring the temporal shapes of the laser pulses, the coupling of the energy into the silver clusters can be controlled, leading to a maximum yield of highly charged atomic ions and an enhancement of the highest atomic charge states. The corresponding optimized laser fields allow to unravel the plasmon-enhanced ionization dynamics in metallic clusters. For xenon clusters, fitness landscape scans of the laser parameters show that a simple two-step ionization scheme gives rise to an extreme charging of the clusters. Three-pulse sequences obtained in an optimization experiment are even more effective and result in maximum yields of different selected charge states of xenon clusters. The findings are in good agreement with simulations.

## **Zusammenfassung**

Die Ionisationsdynamik von Silber- und Xenonclustern in Heliummatrix in starken Laserfeldern werden mit Hilfe der Methode der Pulsformung untersucht. Durch Anpassung der zeitlichen Form des Laserfeldes kann die Kopplung der Energie in die Silbercluster angesteuert werden, was zu einer maximalen Ausbeute von hochgeladenen atomaren Ionen und eine Erhöhung des höchsten gemessenen Ladungszustandes führt. Die zugehörigen optimierten Laserfelder zeigen dass die plasmonverstärkte Ionisationsdynamik zu extreme Materiezustände in metallischen Clustern führt. Es wurde festgestellt, dass bei Dreifach-Pulssequenzen das System noch stärker absorbiert und eine maximale Ausbeute ausgewählter Ladungszustände in Xenonclustern erreicht wird. Diese Ergebnisse sind in guter Übereinstimmung mit Simulationen.



# Contents

<b>Abstract / Zusammenfassung</b>	<b>i</b>
<b>Contents</b>	<b>iv</b>
<b>1 Introduction</b>	<b>1</b>
<b>2 Control of Ultrashort Laser Pulses</b>	<b>5</b>
2.1 Fundamentals of Ultrashort Laser Pulses . . . . .	5
2.1.1 Representations . . . . .	5
2.1.2 Control and Optimization . . . . .	11
2.1.3 Characterization . . . . .	15
2.2 Reviewed Data on the Control of Ultrashort Laser Pulses . . . . .	19
2.2.1 Experimental Details . . . . .	20
2.2.2 Pulse-Precompression . . . . .	26
2.2.3 Removal of the Time-Ambiguity in SHG FROG . . . . .	27
2.2.4 Tailoring of Colored Double Pulses . . . . .	30
2.2.5 Tailoring of Intense Colored Pulse Trains . . . . .	34
<b>3 Optimal Control of Intense Laser-Cluster Interactions</b>	<b>39</b>
3.1 Fundamentals of Clusters in Intense Laser Fields . . . . .	39
3.1.1 Generation of Cluster Beams . . . . .	39
3.1.2 Clusters in Intense Laser Fields . . . . .	40
3.1.3 Dynamics of Clusters in Helium Nanodroplets . . . . .	46
3.2 Reviewed Data on the Control of Intense Laser-Cluster Interactions . . . . .	48
3.2.1 Silver Clusters . . . . .	48
3.2.2 Xenon Clusters exposed to Intense Colored Multipulses . . . . .	53
<b>4 Conclusions and Outlook</b>	<b>65</b>
<b>Bibliography</b>	<b>66</b>
<b>A Publications</b>	<b>83</b>
A.1 Publications within the Thesis . . . . .	85
A.1.1 Removal of the direction-of-time ambiguity in SHG FROG . . . . .	85
A.1.2 Generation of intense colored pulse trains . . . . .	87
A.1.3 Charging of metal clusters in Intense Laser Fields . . . . .	89
A.1.4 Resolving the Ion and Electron Dynamics in Finite Systems . . . . .	91
A.1.5 Optimal control of the strong-field ionization of silver clusters . . . . .	93

A.1.6	Tailored Laser Pulses for Intense Laser-Cluster Studies . . . . .	95
A.1.7	Global Chirp Dependence of Intense Laser-Cluster Interactions . . . . .	97
A.1.8	Charge State Bleaching in Intense Laser-Cluster Interactions . . . . .	99
A.2	Surrounding Publications . . . . .	101
A.2.1	Thomson scattering from near-solid density plasmas . . . . .	101
A.2.2	Line spectroscopy of warm dense aluminum plasma . . . . .	103
A.2.3	Soft X-Ray Thomson Scattering in Warm Dense Matter . . . . .	105
A.2.4	Using FEL radiation for probing near-solid density plasmas . . . . .	107
<b>B</b>	<b>Supporting Materials</b>	<b>109</b>
B.1	Generation of Ultrashort Laser Pulses . . . . .	109
B.2	Ultrashort Laser Pulse Parameters . . . . .	110
B.3	Nonlinear Optics . . . . .	114
B.3.1	Wave Equations . . . . .	114
B.3.2	Second-order Susceptibility . . . . .	116
B.3.3	Third-order Susceptibility . . . . .	123
B.4	AOPDF: A Mathematical Approach . . . . .	125
B.4.1	Coupled-wave Analysis . . . . .	125
B.4.2	Group-Delay Control . . . . .	128
B.4.3	Amplitude-and-Phase Tailoring with AOPDF . . . . .	128
B.5	Evolutionary Operators . . . . .	130
B.5.1	Selection . . . . .	130
B.5.2	Recombination . . . . .	132
B.5.3	Crossover . . . . .	132
B.5.4	Mutation . . . . .	134
	<b>List of Publications</b>	<b>135</b>
	<b>Curriculum vitae</b>	<b>138</b>
	<b>Declaration</b>	<b>139</b>
	<b>Acknowledgements</b>	<b>141</b>



# Chapter 1

## Introduction

Over the last decade, the study of the interaction of nanoparticles with intense femtosecond ( $10^{-15}$  s) laser pulses has become an important field of research. It has significantly contributed to the understanding of response of matter to strong laser fields [1], particularly the laser-induced plasma physics [2]. Considered as novel state of matter on the nanometer scale, *clusters* are aggregates of atoms or molecules, ranging from a few to over millions atoms [3]. When used as targets, clusters offer unique properties to investigate the fundamental laser-matter interaction processes such as collective excitations and laser energy absorption mechanisms. By changing the size of clusters the transition region from atoms to bulk of these processes can be studied.

A remarkable feature of clusters under strong laser fields is their extremely high absorption efficiency. For instance, an absorption efficiency of almost 100% has been demonstrated for xenon clusters in a molecular beam [4]. This leads to the production of energetic (multi-keV) electrons [5] and (MeV) ions [6], as well as EUV and soft X-ray emission [7]. Highly charged atomic ions  $\text{Xe}^{q+}$  up to  $q = 40$  are also generated at a moderate laser peak intensity  $2 \times 10^{16} \text{ W cm}^{-2}$  [6].

Such laser-heated clusters have many promising applications. The resulting highly energetic ions for instance have been used to trigger nuclear reactions in large deuterium clusters [8,9,10], giving rise to prospects for a tabletop accelerator or even neutron source. Further, pulsed debris-free femtosecond x-ray sources [11] from laser-driven clusters can provide an alternative to synchrotron radiation sources, making them affordable for widespread use in research laboratories and hospitals. This opens the possibility for singleshot ultrafast extreme-ultraviolet (EUV) lithography and microscopy [12]. Finally, rare gas clusters can also be used to create plasma waveguides [13,14], suitable for high-field applications such as laser wakefield accelerators [15], X-ray lasers and high-harmonic generation [16].

It has generally been well accepted that, in the visible and infrared spectral range, a plasmon-enhanced coupling of a transient nanoplasma [17] with intense laser fields

is responsible for the efficient energy absorption of clusters. Within this model, cluster heating goes along with a temporary resonant collective oscillation of quasifree electrons (Mie-plasmon [18]). The corresponding eigenfrequency, the so-called Mie-frequency  $\omega_{\text{Mie}} \propto \sqrt{\rho_{\text{ion}}(t)}$ , depends on the ionic background density  $\rho_{\text{ion}}$ , typically being in the UV and thus well beyond the laser photon energy of 1.54 eV (800 nm). Upon excitation with intense laser pulses, the cluster expands, leading to a redshift of  $\omega_{\text{Mie}}$ . When the Mie-frequency eventually matches the laser frequency, a resonant absorption occurs, which efficiently heats up the cluster leading to a Coulomb explosion.

Extensive effort has been devoted to *control* and *optimize* the strong-field ionization of clusters. One approach is to tune the preparation conditions of cluster sources such as distribution of cluster sizes [19], clusters species [20] and constituents of the cluster target [21, 22]. An alternative way is varying the laser parameters such as pulse duration [23, 24, 25, 26, 27], sign of chirp [28, 29], delay-variable dual pulse [30, 31], wavelength [32, 33, 34], or even polarization state [5, 19, 31, 35, 36, 37]. In particular, in an experiment on xenon clusters  $\text{Xe}_N$  (with  $\langle N \rangle \simeq 4 \times 10^4$ ) using stretched pulses, a maximum of X-ray yield at 4.4 keV has been observed for an optimum pulse duration of 250 fs [38]. Fukuda *et al.* [28] have achieved 60% enhancement of the mean ion energy for a negatively chirped 500 fs pulse, compared to that for a positive chirp. Time-resolved experiments which relied on dual-pulse schemes have also found an optimum optical delay for maximum ion yields [30] and kinetic energies of electrons [31], indicating the efficient collective heating mechanism. An effect of simple temporal pulse shapes on the ion energies has been identified in experiments by Mendham *et al.* [29], in which remarkable enhancements (up to factor of two) in the energies of the ions have been obtained for a strong main pulse with a weak additional shoulder in the leading edge.

Recent advances in laser technology [39, 40] have made it possible to perform *optimal feedback control* experiments on clusters. Femtosecond pulse shaping combined with self-learning algorithms in a closed-loop optimization scheme [41] has been employed to maximize the highest- $q$  ion yields from the Coulomb explosion of xenon clusters  $\text{Xe}_N$  exposed to laser intensities  $\sim 10^{15} \text{ W cm}^{-2}$  [42]. The obtained optimal pulse breaks into two 120 fs-pulses with an optical delay of 500 fs, as in the controlled dual-pulse experiments [30]. In a similar approach, Moore *et al.* [20] optimized the yield of X-ray ( $h\nu > 500 \text{ eV}$ ) from argon clusters and got an optimal double-pulse with a 220 fs delay. Along this line, semiclassical molecular dynamics simulations by Martchenko *et al.* [43] predicted that ionization may be optimized by a sequence of two or three pulses, depending on the particular combination of cluster size, laser intensity, and wavelength.

So far, however, we are far from a complete theoretical understanding of the complex dynamics driven by shaped laser pulses for following major reasons. First, the strongly nonlinear response of clusters under strong laser fields [44] leads to dramatic changes of

the ionization dynamics even with small variations of cluster or applied laser conditions. Second, as well-known in coherent quantum control, the interpretation of the adaptively determined pulses is not always straightforward. This is often due to the complex structures of the optimized pulses, or the presence of several possible pathways, which might result in similar feedback values [45]. Third, the free clusters used in earlier optimal experiments [20, 42] have certain size distributions, which actually are not really stable during the optimization search, making the analysis of the optimal pulses further challenging.

Within the framework of the project A5<sup>1</sup> of the Sonderforschungsbereich (SFB) 652, the present thesis addresses to the issue of optimal control over the strong-field ionization dynamics in clusters, using an amplitude-and-phase pulse shaper combined with an evolutionary algorithm. We will extend the earlier optimal control studies [20, 42, 43] to both metallic and rare gas systems, i.e., Ag<sub>N</sub> and Xe<sub>N</sub>.

To cope with the current challenges we will introduce a number of significant improvements with respect to (i) the cluster source, (ii) modulation and characterization of intense ultrashort laser pulses, and (iii) optimal control techniques. First, in collaboration with Sebastian Göde [46], we will make use of clusters embedded in helium nanodroplets using the pick-up source [47] which has shown an extremely long-term stability and a well-controlled cluster distribution, suitable for optimization experiments.

Second, a pulse shaper placed in between a femtosecond oscillator and an amplifier allows for the control of shaped laser pulses with peak intensities greater than  $10^{16}$  Wcm<sup>-2</sup> at a 1 kHz-repetition rate. In addition, strong-field cluster dynamics have shown evidences of the time-frequency coupling effect [20, 28]. Therefore to determine the corresponding information, the tailored laser pulses will be fully characterized with the *frequency-resolved optical gating* (FROG) technique [48].

Finally, based on the pulse shaper a number of laser parameters such as chirp, laser intensity, and double-pulse delay, can be probed together in a single scan (the *open-loop* control scheme). This step permits to link (or classify) different excitation processes simultaneously occurring during the intense laser-cluster interaction, giving rise to buildup of the corresponding *knowledge-toolkits* towards unrestricted optimization. Furthermore, a *closed-loop* feedback control scheme limited to simple pulse shapes will be applied to reduce the complexity and accelerate the optimization search. A combination of both schemes could pave the way for the use of femtosecond pulse shaping not only to control but also to serve as an *analytic tool* for the study of the dynamics of complex systems.

Within the program of the SFB 652, collaboration with other projects on related themes has been made. On the one hand, a project<sup>2</sup> to develop a mass-selected trapped cluster source is under way, which may serve for optimal control experiments on single-size clusters in the near future. On the other hand, to unravel the underlying physics delivered

<sup>1</sup>Project A5: "Controlled strong-field excitation of clusters and particles by shaped laser pulses"

<sup>2</sup>Project A3: "Correlated processes in laser-excited trapped cluster ions"

by the determined optimal fields, analysis of the experimental results will be supported with adaptive control simulations based on a modified nanoplasma model [49].<sup>3</sup> Additionally, at high laser intensities the He environment might be also ionized and consequently lead to multiple resonances in the core-shell system [50, 51]. This issue will be taken into account by a microscopic approach [52].<sup>4</sup>

The thesis proceeds in a cumulative manner as follows.

- *Chapter 2* covers the control of ultrashort laser pulses with the use of a pulse shaper combined with computer self-learning algorithms. Different control techniques will be introduced and tested on well-documented optical systems, preparing a solid basis for optimal control study of the ionization dynamics in clusters. More details about characterization and control of ultrashort pulses can be found in the Publications (A.1.1, A.1.2, and A.1.5).
- *Chapter 3* reviews the experimental results on the study of the strong-field ionization dynamics in He-embedded silver and xenon clusters, employing the femtosecond pulse shaping techniques introduced in chapter 2. Discussion in terms of the theoretical models is provided in detail. The issues in this chapter are mostly included in the Publications (A.1.3 to A.1.8).
- *Chapter 4* sums up the main achievements of the present work and outlines some suggestions for future experiments.
- *Publications A.1* presents in detail the published results which have been provided in a systematical but brief view in chapter 2 and 3. The surrounding work related to the project A2<sup>5</sup> is covered in Publications A.2.

---

<sup>3</sup>Project A6: "Absorption, ionization and control of dense Coulomb systems in laser fields"

<sup>4</sup>Project A8: "Microscopic description of atomic clusters in intense laser fields"

<sup>5</sup>Project A2: "Thomson scattering and correlations in warm dense matter"

# Chapter 2

## Control of Ultrashort Laser Pulses

Understanding of the characteristics of ultrashort laser pulses is the key to generate and control them. In optimal control experiments on complex systems, the ultimate mission is to find the optimal pulse shape which leads to the optimum of a process of interest. This pulse is close to the optimal solution and in turn hints at the possible underlying dynamics in the system under investigation. The present chapter describes the basics of intense ultrashort laser pulses and represents the experimental results on the strong-field control which have served as the major tools to study clusters introduced in chapter 3. Part of the results have been published and can be found in the Publications ([A.1.1](#), [A.1.2](#) and [A.1.5](#)).

### 2.1 Fundamentals of Ultrashort Laser Pulses

Femtosecond (fs) light pulses are electromagnetic wave packets and can be completely described by the time and space dependent electric field. Within the frame of a semi-classical picture, the propagation of such fields and their interaction with matter are defined by Maxwell-equations with a macroscopic polarization as the material response. In this section, we will first summarize the key characteristics of ultrashort laser pulses and then present the techniques to fully characterize and control them. Further fundamentals involving femtosecond laser pulses are given in Appendix B.

#### 2.1.1 Representations of Ultrashort Laser Pulses

Simply speaking, an ultrashort laser pulse is a very short burst of electromagnetic energy and can be defined as function of space and time. Depending on specific problems, a pulse can be described in either the time- or frequency domain, or both (joint time-frequency domain) [53].

## Time-Domain Representation

We consider first the temporal dependence of an electric field  $E(t)$  suppressing its spatial and polarization dependence for clarity. It is convenient to describe the electric field by a complex analytic signal  $\tilde{E}(t)$ , whose amplitude and phase can be obtained from measurements:

$$\tilde{E}(t) = \frac{1}{2}\mathcal{E}(t) e^{i\Gamma(t)}. \quad (2.1)$$

The real electric field can be expressed in terms of this complex quantity as

$$E(t) = \tilde{E}(t) + \tilde{E}^*(t). \quad (2.2)$$

In most practical cases of interest in this work, the laser spectrum will be centered around a mean frequency  $\omega_0$  and will have appreciable values only in a frequency interval  $\Delta\omega$  small compared to  $\omega_0$ . It is therefore desired to introduce a *carrier angular frequency*  $\omega_0$  and describe  $\tilde{E}(t)$  as

$$\tilde{E}(t) = \frac{1}{2}\mathcal{E}(t) e^{-i\varphi(t)} e^{i\omega_0 t} = \frac{1}{2}\tilde{\mathcal{E}}(t) e^{i\omega_0 t}, \quad (2.3)$$

where  $\mathcal{E}(t)$  ( $\tilde{\mathcal{E}}(t)$ ) is termed as the real (complex) field envelope and  $\varphi(t)$  is the time-dependent or temporal phase.

The concept of an envelope and the carrier angular frequency defined in Eq. (2.3) is valid in the cases where the bandwidth is only a small fraction of the carrier angular frequency, namely:

$$\frac{\Delta\omega}{\omega_0} \ll 1. \quad (2.4)$$

This treatment is also called the **Slowly Varying Envelope Approximation**<sup>1</sup> (SVEA) [53], which requires the temporal variations of  $\mathcal{E}(t)$  and  $\varphi(t)$  within an optical cycle  $T = 2\pi/\omega_0$  to be small.

The choice of carrier angular frequency  $\omega_0$  and phase  $\varphi(t)$  is not unique as clearly seen from Eq. (2.1). The most useful choice of the carrier angular frequency should be one that ensures the minimum variation of the phase during the intense portion of the pulse. In practice the angular frequency at the pulse peak is usually the choice for  $\omega_0$ . In general a better definition, which is consistent in both the time and frequency domains, is to use the *intensity-weighted average frequency*

$$\langle\omega_0\rangle = \frac{\int_{-\infty}^{\infty} |\tilde{\mathcal{E}}(t)|^2 \omega(t) dt}{\int_{-\infty}^{\infty} |\tilde{\mathcal{E}}(t)|^2 dt}. \quad (2.5)$$

---

<sup>1</sup>For much shorter (down to the single-cycle regime) pulses, the *slowly-evolving-wave approximation* (SEWA) has to be used to describe the light pulse propagation [54].

It is a common practice to write the temporal phase term as a Taylor series about the time  $t = 0$ :

$$\varphi(t) = \varphi_0 + t\varphi_1 + t^2\varphi_2/2 + \dots, \quad (2.6)$$

where only the first few terms are required to describe *well-behaved* pulses.

The pulse's instantaneous angular frequency is defined as the first derivative of the phase factor  $\Gamma(t)$ :

$$\omega(t) = \omega_0 - d\varphi/dt. \quad (2.7)$$

For  $d\varphi/dt = \varphi_1 \equiv \text{const.}$ , a nonzero value of  $\varphi_1$  means a shift of the carrier frequency towards  $\omega'_0 = \omega_0 - \varphi_1$ . This is also a consequence of the inverse Fourier transform shift theorem [55], which says that:  $\tilde{E}(\omega - \omega_0)$  inverse-Fourier-transforms to  $\tilde{E}(t)e^{i\omega_0 t}$ . Thus a linear term in the temporal phase corresponds to a shift in frequency. For  $d\varphi/dt \neq \text{const.}$ , the carrier angular frequency is a time-dependent quantity, and the corresponding pulse is said to be frequency-modulated or *chirped*. If  $d^2\varphi/dt^2 > (<)0$  in the vicinity of the pulse maximum, the pulse is then called down (up) chirped. An example of an ultrashort Gaussian pulse is displayed in Fig. 2.1. The intensity  $I(t) \propto |\tilde{E}(t)|^2$  is introduced in Appendix B.2.

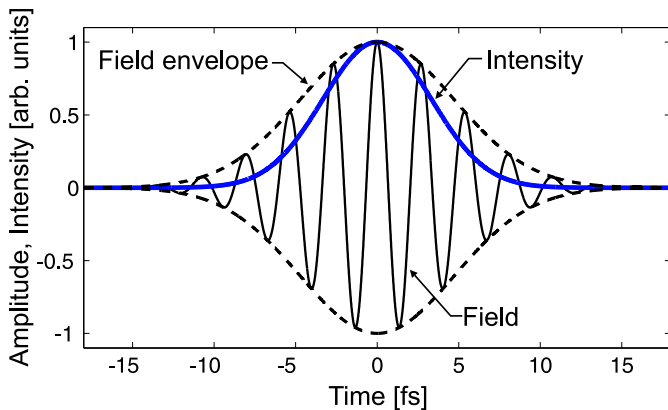


**Figure 2.1:** The electric field, field envelope and intensity of an ultrashort Gaussian pulse. The corresponding temporal phase  $\varphi(t) = 0$  is not plotted.

## Frequency-Domain Representation

The complex-valued spectrum  $\tilde{E}(\omega)$  is obtained from the Fourier inversion theorem of  $\tilde{E}(t)$ ,

$$\tilde{E}(\omega) = \int_{-\infty}^{\infty} \tilde{E}(t) e^{-i\omega t} dt. \quad (2.8)$$

Similar to the time-domain representation, the complex field can be decomposed into *spectral* amplitude and phase as

$$\tilde{E}(\omega) = |\tilde{E}(\omega)| e^{-i\phi(\omega)}, \quad (2.9)$$

where  $|\tilde{E}(\omega)|$  is the spectral amplitude,  $\phi(\omega)$  is the spectral phase containing time-versus-

frequency information. It is usually helpful to expand the spectral phase into a Taylor series about the carrier angular frequency  $\omega_0$ ,

$$\phi(\omega) = \sum_{n=0}^{\infty} \frac{\phi_n}{n!} (\omega - \omega_0)^n, \quad (2.10)$$

where

$$\phi_n = \left. \frac{d^n \phi(\omega)}{d\omega^n} \right|_{\omega_0}, \quad (2.11)$$

are the spectral phase coefficients of  $n^{\text{th}}$ -order. For description of well-behaved pulses, only the first (up to the fourth order) terms are typically needed.

While the laser spectrum (see Appendix B.2) can be simply acquired with a suitable spectrometer, the measurement of the spectral phase was quite tricky until some special techniques, e.g., FROG<sup>2</sup> or SPIDER,<sup>3</sup> have been introduced [40, 56, 57]. In the following, we will discuss the spectral phase in terms of the Taylor series (see Eq. (2.10)) to give a simple picture of the impact of the spectral phase onto the pulse structure. We however note that several complex spectral phase functions, such as the steplike or triangular shapes in Fig. 2.2(d) and (e), respectively, could not be expressed by a Taylor expansion.

#### *Zero-order Phase: The Absolute Phase*

The zero-order phase term,  $\phi_0$ , is known as the absolute phase and often termed as the *carrier-envelope phase* (CEP). It is the offset between the maximum of the electric field and its peak envelope [58]. When the pulse is about few-cycle long, its envelope changes almost as fast as the electric field and the value of CEP really matters. In the present work the shortest involved pulse duration is over ten-cycle long and hence the influence of CEP is not important.

#### *First-order Phase: A Shift in Time*

According to the Fourier transform shift theorem [55], the Fourier transform of  $E(t - \tau)$  gives  $\tilde{E}(\omega) \exp(-i\omega\tau)$ . So a linear spectral phase function,  $\phi = \tau\omega$ , leaves the field envelope unchanged, but shifts the pulse in the time domain. Generally, we care only about the pulse structure (shape), not when it arrives. But in femtosecond pulse shaping this property has successfully been employed to generate tailored pulse trains by addressing different parts (colors) of the laser spectrum with different values of  $\tau$  (see Refs. [59, 60] and also Publications A.1.2). An example of a colored double-pulse created through tailoring a triangular phase function is displayed in Fig. 2.2(e).

<sup>2</sup>FROG: Frequency-Resolved Optical Gating.

<sup>3</sup>SPIDER: Spectral Phase Interferometry for Direct Electric-field Reconstruction.



### Second-order Phase: Linear Chirp

From Eq. (2.7), a quadratic variation of  $\varphi(t)$ , i.e., corresponding to a nonzero value of  $\varphi_2$  (or also  $\phi_2$  in the frequency domain), results in a linear ramp of the instantaneous frequency vs. time and the pulse is then called *linearly chirped*. When applied to a Fourier-transform-limited pulse, a linear chirp results in lengthening of the pulse duration. An example of a linearly chirped Gaussian pulse is given Fig. 2.2(b) and considered in detail in Appendix B.2.

### Higher-order Phases

Optical materials introduce higher-order dispersion and thus induce higher-order phase distortions. Third-order (cubic) spectral phase, for instance, leads to the oscillations after or before the main pulse depending on a positive or negative value of the third-order coefficient  $\phi_3$ , respectively (see, Fig. 2.2(c)). Higher-order terms, produced, e.g., by propagation through an optical fiber [61] or through filamentation in the air [53], can yield additional distortions, giving rise to extremely complex pulse structures.

## Joint Time-Frequency Representations

Time- and frequency-domain representations have usually been proven to be useful in complete description of ultrashort laser pulses. In the cases where both time and frequency properties are strongly coupled, for instance, see Refs. [20, 28] and Publications (A.1.5, A.1.6, A.1.7, and A.1.8) for experiments on clusters, *joint time-frequency* distributions are desired to provide an intuitive view of the pulses [62, 63, 64]. Such functions were already introduced by Wigner [65] and Husimi [66] and have widely been applied to, e.g., quantum mechanics and quantum optics [63, 67].

The *Wigner distribution* of an electric field  $\tilde{E}(t)$  is defined by<sup>4</sup>

$$\mathcal{W}(\tau, \Omega) = \int_{-\infty}^{\infty} \tilde{E}\left(\tau + \frac{t}{2}\right) \tilde{E}^*\left(\tau - \frac{t}{2}\right) e^{-i\Omega t} dt \quad (2.12)$$

$$= \frac{1}{2\pi} \int_{-\infty}^{\infty} \tilde{E}\left(\Omega + \frac{\omega}{2}\right) \tilde{E}^*\left(\Omega - \frac{\omega}{2}\right) e^{i\tau\omega} d\omega. \quad (2.13)$$

Although it contains the complete information on the pulse and often intuitively represents complex pulse, the Wigner function can sometimes be difficult to interpret by complicated interference fringes and by its negative values.

A more intuitive alternative, which will be used throughout the text, is the *Husimi spectrogram*  $\mathcal{H}(\tau, \Omega)$ , obtained by smoothing the Wigner distribution with a Gaussian function:

$$\mathcal{H}(\tau, \Omega) = \left| \int_{-\infty}^{\infty} g(t - \tau) \tilde{E}(t) e^{-i\Omega(t-\tau)} dt \right|^2. \quad (2.14)$$

<sup>4</sup>Here  $\tau$  and  $\Omega$  are conjugated variables as in the Fourier transforms.

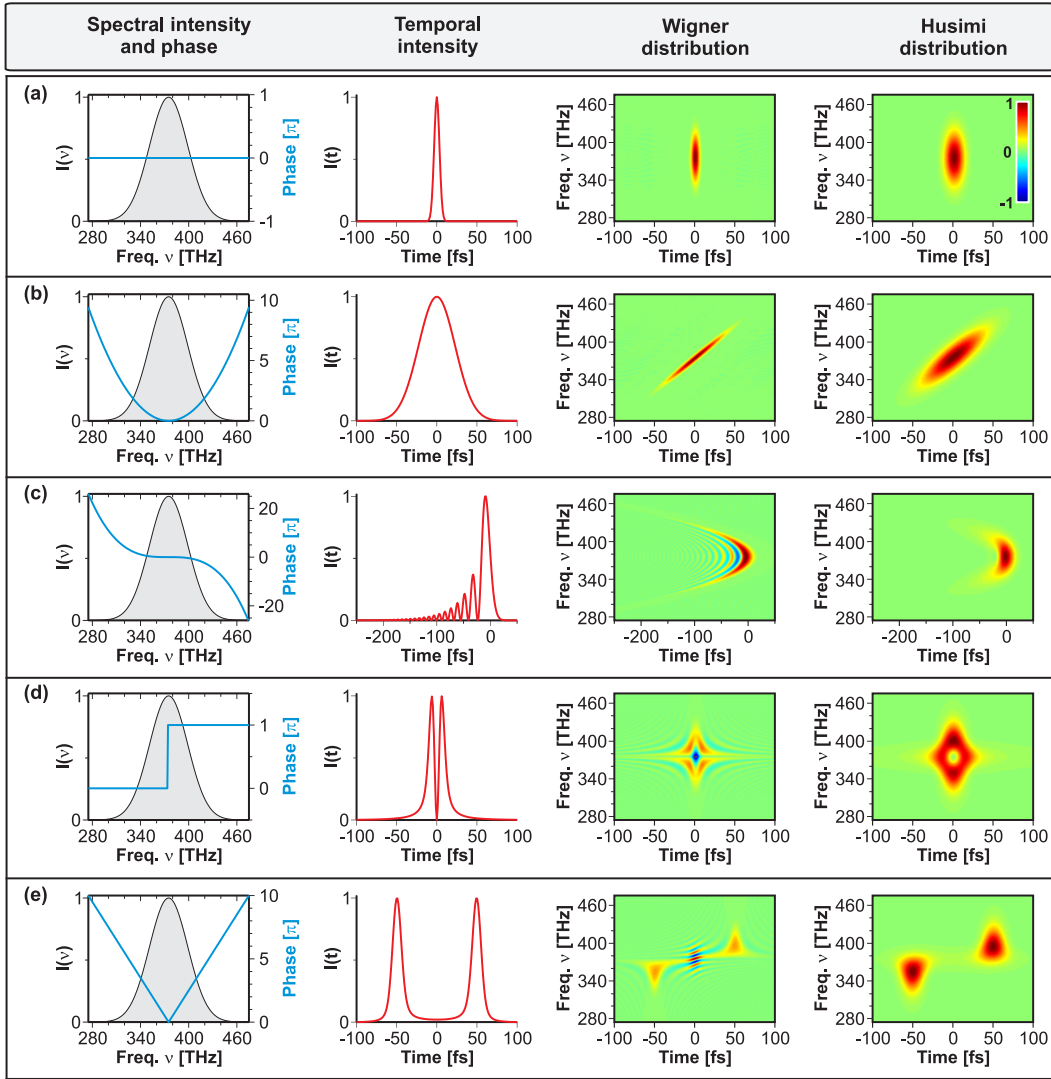


**Figure 2.2:** Examples of various pulse shapes represented by different methods as indicated. (a) Fourier-transform-limited pulse. (b) Linearly chirped ( $\phi_2 = 150 \text{ fs}^2$ ) pulse. (c) Cubic ( $\phi_3 = -2000 \text{ fs}^3$ ) phase. (d) Steplike spectral phase function. (e) Triangular spectral phase function. For the calculation of the Husimi functions, a gate constant  $\sigma = 10 \text{ fs}$  is chosen. Note the negative values delivered by the Wigner distributions.

The window function  $g(t)$  is given as

$$g(t) = \exp[-t^2/(2\sigma^2)]/\sqrt{2\pi\sigma^2}, \quad (2.15)$$

where  $\sigma$  is a time constant, usually set to the bandwidth-limited pulse width of the given spectrum. The Husimi function  $\mathcal{H}(\tau, \Omega)$  tells us at which time  $\tau$  a certain frequency  $\Omega$  is present in the original signal  $\tilde{E}(t)$ . Examples of Wigner and Husimi distributions for various pulse shapes are depicted in Fig. 2.2.

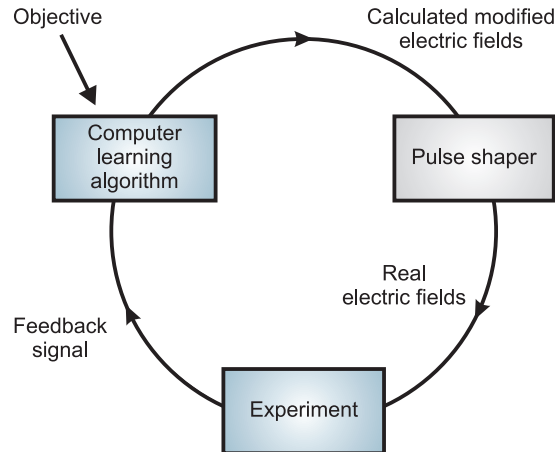


**Figure 2.3:** Basic layout of a closed-loop feedback control scheme. Adapted from [78]

### 2.1.2 Control and Optimization of Ultrashort Laser Pulses

Over the last two decades, advances in femtosecond pulse shaping technology have enabled unprecedented control over ultrashort waveforms for ultrafast spectroscopy, nonlinear optics and high-field physics [68, 69]. Within this context, two main approaches have been demonstrated. On the one hand, a *closed-loop feedback control* scheme [41, 70, 71, 72, 73, 74, 75, 76, 77] has been employed to find the optimal pulse shapes: different pulse shapes are evaluated by a self-learning (evolutionary) algorithm to create an improved pulse shape, which leads to an efficient excitation, without insight into the physical mechanism. This concept is often termed as ”adaptive femtosecond quantum control,” ”closed-loop control,” or ”optimal control experiment,” and schematically shown in Fig. 2.3.

On the other hand, the impact of pulse shapes on complex systems can be systematically studied within an *open-loop scheme* [79, 80, 81, 82, 83, 84]. It consists of reaching a specific goal, e.g., manipulation of the temporal response of a system excited by an optical pulse, without any experimental feedback. For small and well-understood systems, physical analysis of the process allows one to predetermine the theoretical pulse shape which yields the desired result. It is then tested experimentally.

Pulse shaping techniques presented here in brief are based on the linear, time-invariant filter, which can be described either in the time domain or in the frequency domain (see, Fig. 2.4). In the time domain, the filter is characterized by an impulse response function  $h(t)$ . The output electric field  $E_{\text{out}}(t)$  is given by the convolution of an input field  $E_{\text{in}}(t)$  and the impulse response  $h(t)$ :

$$E_{\text{out}}(t) = E_{\text{in}}(t) \otimes h(t) = \int dt' E_{\text{in}}(t') h(t - t'), \quad (2.16)$$

where  $\otimes$  denotes convolution. However, due to their short duration, femtosecond laser

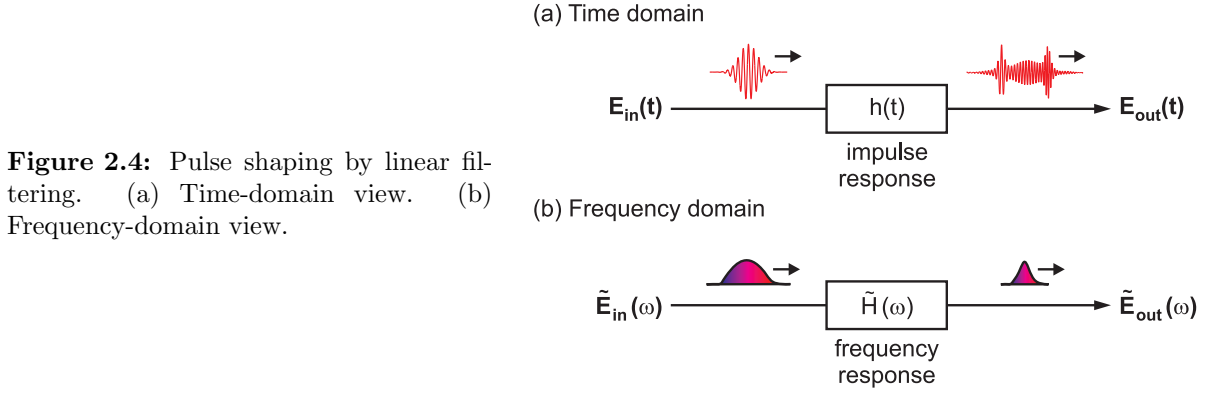


**Figure 2.4:** Pulse shaping by linear filtering. (a) Time-domain view. (b) Frequency-domain view.

pulses cannot be directly shaped in the time domain. Most of the pulse shaping devices therefore operate in the frequency domain and the output pulse is given as

$$\tilde{E}_{out}(\omega) = \tilde{H}(\omega)\tilde{E}_{in}(\omega), \quad (2.17)$$

where the frequency response function  $\tilde{H}(\omega) = R(\omega) \exp[-i\Phi(\omega)]$ , with the spectral amplitude response  $R(\omega)$  and the spectral phase transfer function  $\Phi(\omega)$ .

There are two major approaches to realize a pulse shaper, based on (i) the Fourier transform synthesis or the  $4f$ -setup [68] and (ii) the acousto-optic interaction [85] termed as the acousto-optic programmable dispersive filter (AOPDF). The former makes use of liquid-crystal spatial light modulators, deformable mirrors, and acousto-optic modulators as the linear filter [40, 68, 86]. Depending on specific design of the linear filter, tailoring of the phase [68], both phase and amplitude [87] or even the polarization state [88] of ultrashort optical pulses has been demonstrated. Due to its complex setup, a  $4f$ -based pulse shaper is not an optimal solution for high-power laser chains.

The latter is able to modulate both the spectral phase and amplitude of a femtosecond optical pulse by controlling the acousto-optic interaction in an acousto-optic crystal [85]. It has been used in the control experiments on clusters presented in chapter 3. Further detail is given in the following.

## Acousto-Optic Programmable Dispersive Filters

### Introduction

First introduced by Tournoir in the late 1990s [89], AOPDF offers a new alternative to the  $4f$ -approach, requiring neither dispersive elements (gratings or prisms) nor a telescope. The device is based on the acousto-optic interaction between ultrashort optical pulses with an acoustic wave in a birefringent crystal [85]. AOPDFs are now available for wavelength ranging from UV to near-IR (0.2-4  $\mu\text{m}$ ) [90, 91, 92], and possibly extending to the mid-IR of up to 20  $\mu\text{m}$  [93].

Widespread applications of AOPDFs have been demonstrated over the last decade.

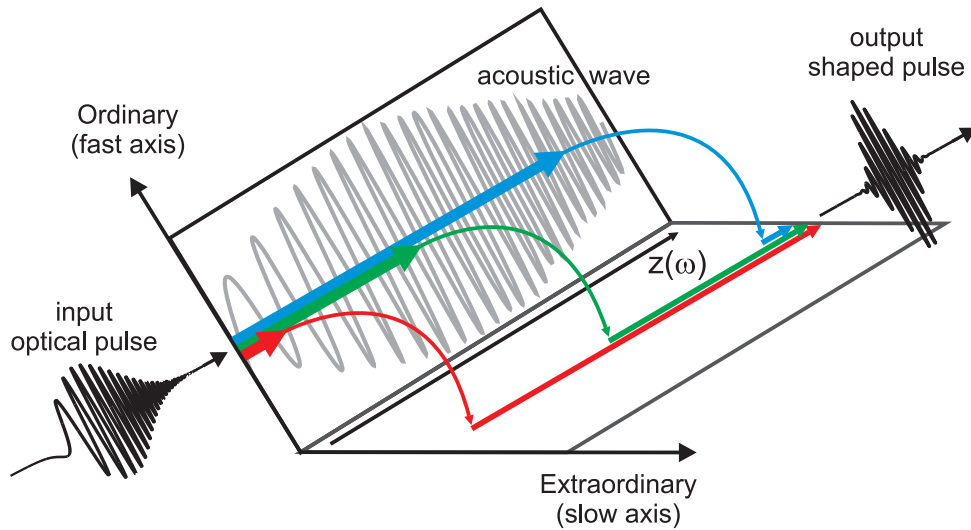


**Figure 2.5:** Schematic view of the AOPDF principle. By diffraction on the acoustic grating at the phase-matching conditions, the different wavelengths (indicated with colors) of the ultrashort optical pulse can be switched to the extraordinary axis at different locations in the crystal, and thus experience different spectral phases.

The compact design of AOPDFs makes them very stable and easily implementable in an amplifier laser chain or in a pump-probe scheme with only slight adjustments. They have been proven to be useful to compensate for high-order dispersion or spectral gain narrowing in high-power (OP)CPA systems [94, 95, 96, 97], to control the spectral phase and amplitude of ultrashort pulses in, e.g., coherent control experiments [98, 99, 100], or even in characterization setups [101, 102]. Additionally, it has been reported recently that AOPDF can be used to stabilize the carrier-envelope phase drift of amplified femtosecond laser pulses [103] leading to the generation of intense CEP-controlled few-cycle pulses. We will present the working principles of an AOPDF in a phenomenological approach. Further mathematical details can be found in Appendix B.4.

### *Phenomenological Approach*

In AOPDF, an acoustic wave is launched in an acousto-optic crystal by an rf (radio frequency) transducer (see Fig. 2.5). When propagating along the  $z$  axis, the acoustic wave reproduces spatially the temporal shape of the rf signal. Due to the slow velocity of the acoustic wave compared to that of optical waves and due to their ultrashort pulse duration, the incident optical pulses will see a fixed dielectric grating inside the acousto-optic device<sup>5</sup> and will be diffracted into optical modes described by the plane-wave approximation [85].

Let us now assume that the rf signal is chirped, i.e., its instantaneous frequency is a time-dependent function. The acoustic wave will then recreate this behavior spatially, and its local spatial frequency will also be chirped. It is well-known that two optical modes can

<sup>5</sup>Here, we neglect the small Doppler frequency shift that is always present with acousto-optic interactions.

be coupled efficiently by an acousto-optic interaction only in the case of *phase-matching* conditions [85]. Therefore, different frequency  $\omega$  of an optical pulse will be diffracted at different position  $z(\omega)$  in the crystal.

When phase-matching conditions occur for a particular optical frequency, part of its energy in mode 1 (fast axis) is switched into mode 2 (slow axis) with a different polarization<sup>6</sup> as indicated in Fig. 2.5. The optical pulse leaving the crystal on mode 2 consists of all frequencies that have been diffracted at various locations. If the optical velocities of the two modes are different, then each frequency will experience a different time delay (or also optical path). Arbitrary phase modulation can thus be achieved by controlling the phase-matching, or, equivalently, by properly choosing the temporal form of the rf signal. In addition, the local acoustic amplitude defines the intensity of the diffracted wave and therefore corresponds to an amplitude modulation.

## Evolutionary Algorithms

Evolutionary algorithms (EAs) have become widely-used tools for search, optimization, machine learning and design [104]. In physics, for instance, EAs have found various applications in, e.g., quantum mechanical calculations of atoms and small molecules, thermodynamics, and astronomy [105], as well as in quantum control [69, 106, 107].

Among different types of evolutionary algorithms, *genetic algorithms* (GA) and *evolution strategies* (ES) appear as the most basic forms. While GAs were initially developed in the US by John Holland and his students [108, 109], ESs were independently started in the early 1970's at the Technical University of Berlin by Ingo Rechenberg and Hans-Paul Schwefel and their co-workers [110]. GAs have long been employed as multipurpose techniques with application in search, optimization, design and machine learning. On the other hand, ESs have been mostly used in optimization. Historically, ESs are generally applied to real-valued representations of optimization problems, and emphasize mutation over crossover (recombination). The latter supports the *exploration* of the ES search instead of *exploitation*.

Evolutionary algorithms contain a population of structures (individuals) that evolve according to rules of *selection* and perturbation operators such as *recombination* and *mutation*. Each individual is evaluated, giving the feedback as its *fitness value* in the environment. Through the selection procedure, individuals with higher fitness have more chance to "survive" and are able to pass their "genes" to the new-produced individuals (offspring). Selection therefore tends to exploit the available fitness information. Recombination and mutation, on the other hand, concentrate on the general heuristics for exploration by perturbing those individuals. Though quite simplistic from the biological viewpoint, EAs are sufficiently complex to give robust and powerful adaptive search

---

<sup>6</sup>For simplicity, the polarizations of the two modes are assumed orthogonal.

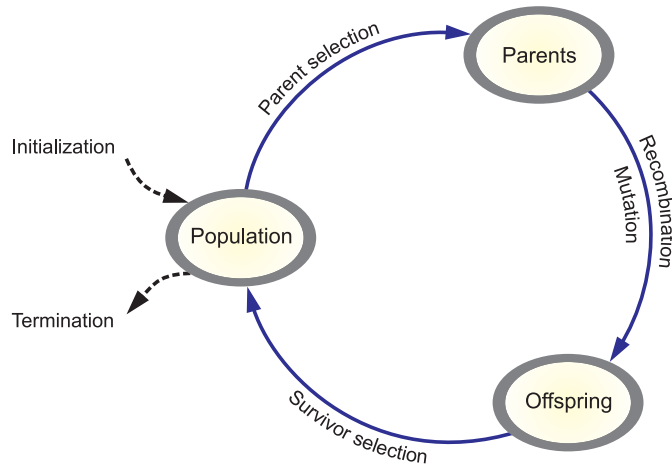


**Figure 2.6:** A standard scheme of an evolutionary algorithm.

mechanisms.

A standard flow-chart of evolutionary algorithms is displayed in Fig. 2.6. An evolutionary algorithm typically starts by creating an *initial population* randomly although seeded initialization with pre-knowledge of the studied system might be sometime helpful. *Evaluation* provides the fitness of each individual, which can be a calculated value of a mathematical function or an elaborate simulation, or a measured signal in experiments. Selection is a mix of two different concepts, i.e., the parent- and survivor-selection. Based on the fitness, the "good" parents are chosen for reproduction by exchanging their information. Through mutation, their children are further perturbed with a certain mutation probability and then evaluated again. Finally, the survival step decides who survives in the population.

The evolutionary algorithm used for optimal control experiments in the present work is a combination of genetic algorithm and evolution strategy, and can be switched between them. The fidelity and robustness of this EA have been proven and reported in our recent papers [98, 111, 112]. Details about the basic operators including selection, recombination (crossover) and mutation are provided in Appendix B.5, following the textbook of Pohlheim [113].

### 2.1.3 Characterization of Ultrashort Laser Pulses

One of the main tasks in optimal-control experiments on complex systems in strong laser fields is to (completely) characterize the electric field of the tailored ultrashort pulses. It has been shown that both intensity and phase play decisive roles in several phenomena such as high-harmonic generation processes [114], wave-packet motion in organic molecules [115], the direction of chemical reactions [76, 77], or intense laser-cluster interactions [29, 44, 111, 116, 117].

A number of techniques have been developed to measure ultrashort pulses and de-

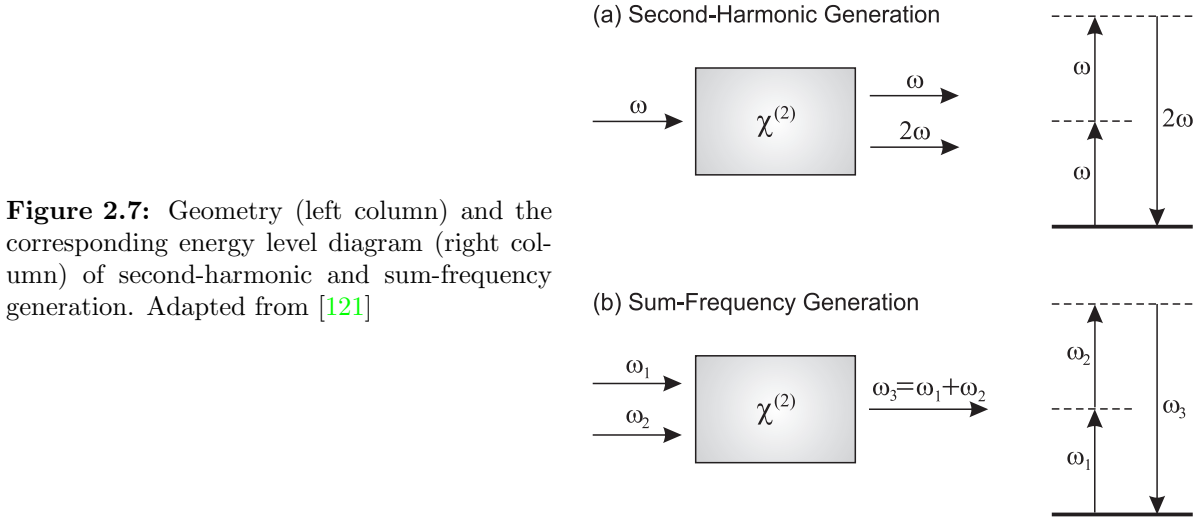


**Figure 2.7:** Geometry (left column) and the corresponding energy level diagram (right column) of second-harmonic and sum-frequency generation. Adapted from [121]

scribed in great detail elsewhere [40, 48, 53, 86, 118, 119]. In the present work we used two methods to characterize the pulses. The first one is the *intensity-autocorrelation* technique which quickly delivers the temporal intensity with a high-dynamic range. The other uses *frequency-resolved optical gating* (FROG) which provides both intensity and phase information.

Most characterization methods make use of nonlinear optics. Before the invention of the laser [120], some classes of nonlinear optical effects were already discovered such as Pockels and Kerr electrooptic effects [121] or light-induced resonant absorption saturation [122]. Systematic studies of nonlinear optical phenomena however became possible only after the realization of lasers, especially short laser pulses. The first nonlinear optical experiment with laser was demonstrated by Franken *et al.* [123] in 1961 to demonstrate the *second-harmonic generation* (SHG), i.e., the output light has a double frequency as the incident one.

Nowadays, with the development of modern laser technologies providing ultrashort and intense laser pulses, the nonlinear optical phenomena become more and more popular and diversified. To describe the optical nonlinearity more precisely, we follow Boyd [121] by writing the induced polarization  $\tilde{P}(t)$  as function of an applied optical field  $\tilde{E}(t)$ :

$$\begin{aligned} \tilde{P}(t) &= \epsilon_0[\chi^{(1)}\tilde{E}(t) + \chi^{(2)}\tilde{E}^2(t) + \chi^{(3)}\tilde{E}^3(t) + \dots] \\ &\equiv \tilde{P}^{(1)}(t) + \tilde{P}^{(2)}(t) + \tilde{P}^{(3)}(t) + \dots, \end{aligned} \quad (2.18)$$

where  $\chi^{(2)}$  and  $\chi^{(3)}$  denote the second- and third-order nonlinear optical susceptibilities, respectively.

Within the context of this work,  $\chi^{(2)}$  is responsible for the second-harmonic generation (SHG,  $\omega + \omega$ ) and the sum-frequency generation (SFG,  $\omega_1 + \omega_2$ ) as shown in Fig. 2.7. These processes are used in the intensity autocorrelator and SHG FROG, and the third-harmonic generation (THG,  $\omega + 2\omega \rightarrow 3\omega$ ) described later. Instead,  $\chi^{(3)}$  accounts for



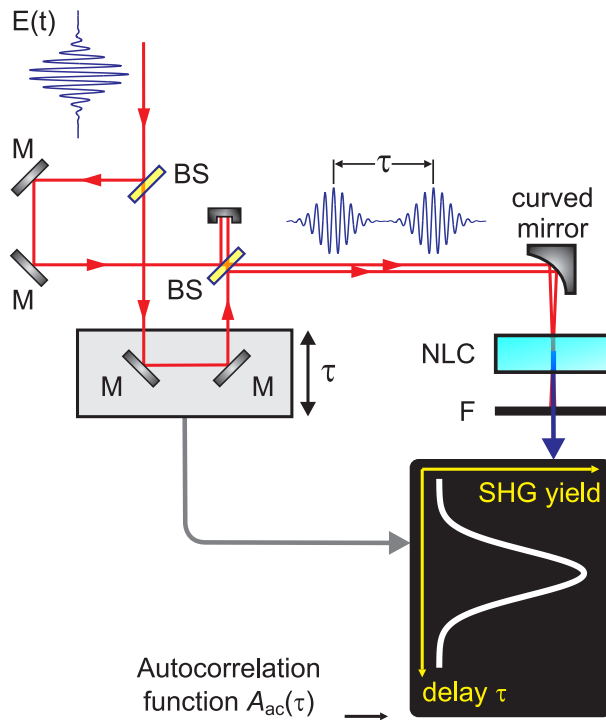


**Figure 2.8:** Basic layout of a SHG-based intensity autocorrelator. The input pulse  $E(t)$  is split into two replicas, which are relatively delayed and then recombined and focused on a  $\chi^{(2)}$  nonlinear crystal (NLC) to create the second-harmonic generation. The SHG-signal as function of the optical delay gives the autocorrelation function  $A_{ac}(\tau)$ . BS: beamsplitter. M: flat mirror. F: SHG-filter blocking the fundamental beams.

the third-order processes employed in other FROG geometries [48] such as polarization-gating, self-diffraction, third harmonic-generation (THG,  $\omega + \omega + \omega \rightarrow 3\omega$ ) and transient gating FROG mentioned below. More details about these processes can be found in Appendix B.3.

### Intensity Autocorrelator

The temporal profile  $I(t)$  of an optical pulse can be determined by measuring its intensity autocorrelation:

$$A_{ac}(\tau) = \int I(t)I(t - \tau) dt. \quad (2.19)$$

Its corresponding Fourier-transform is then given as

$$\tilde{A}_{ac}(\Omega) = |\tilde{I}(\Omega)|^2, \quad (2.20)$$

where  $\tilde{I}(\Omega)$  is the Fourier-transform of  $I(t)$ . Equation (2.20) shows that  $\tilde{A}_{ac}(\Omega)$  is a real-valued function, indicating the corresponding autocorrelation symmetric in time,  $A_{ac}(\tau) = A_{ac}(-\tau)$ . The technique has widely been used to quickly deliver the temporal shape of ultrashort laser pulses. It however contains no phase information and has an ambiguity in the direction of time. By assuming a pulse shape (generally a  $\text{sech}^2$ - or a Gaussian shape, see Table B.1) the pulse duration can also be extracted. A SHG-based intensity autocorrelator is illustrated in Fig. 2.8. For further details see, e.g., Refs. [48, 53, 124].

## Frequency-Resolved Optical Gating Methods

A complete characterization can be obtained by measuring a spectrogram of the pulse in the joint time-frequency domain, involving both temporal and spectral resolutions simultaneously [125]. An intuitive example of such a measurement is the musical score, which plots a sound wave's shot-time spectrum as function of time, with additional information on the top indicating intensity. A mathematical description of the musical score is the spectrogram [126]:

$$S(\omega, \tau) = \left| \int_{-\infty}^{\infty} E(t)g(t - \tau) \exp(-i\omega t) dt \right|^2, \quad (2.21)$$

with a variable-delay gate function  $g(t - \tau)$ . The full information of  $E(t)$  can be reconstructed from the spectrogram, except for an absolute phase term  $\phi_0$  (see Eq. (2.10)). The FROG technique includes measuring the spectrogram of the pulse and then retrieving both phase and amplitude information from the experimental spectrogram [48].

By modifying a SHG-based intensity autocorrelator (see Fig. 2.8), for instance, a simple version of FROG, called SHG FROG, can be obtained. While in the autocorrelator the signal intensity is measured, in SHG FROG measurement the signal pulse is spectrally resolved as a function of optical delay resulting in the spectrogram or the FROG trace:

$$I_{\text{FROG}}^{\text{SHG}}(\omega, \tau) = \left| \int_{-\infty}^{\infty} E(t)E(t - \tau) \exp(-i\omega t) dt \right|^2 \quad (2.22)$$

$$= \left| \int_{-\infty}^{\infty} E_{\text{sig}}(t, \tau) \exp(-i\omega t) dt \right|^2, \quad (2.23)$$

where  $E_{\text{sig}}(t, \tau)$  gives the signal-field. 2D-phase retrieval algorithms [48, 56, 127, 128] are then introduced to provide the phase and amplitude information of the pulse. A *FROG error* [48] is given to measure the success of a retrieved procedure.

Different nonlinear processes can also be employed leading to alternative types of spectrograms. The other most commonly used geometries are *polarization gate* (PG-), *self-diffraction* (SD-), *third-harmonic generation* (THG-), and *transient grating* (TG-) FROG as shown in Fig. 2.9. Their corresponding mathematical forms of the signal field can be described in terms of the input pulse  $E(t)$  as

$$E_{\text{sig}}(t, \tau) \propto \begin{cases} E(t)|E(t - \tau)|^2 & \text{for PG FROG} \\ E(t)^2 E^*(t - \tau) & \text{for SD FROG} \\ E(t)E(t - \tau) & \text{for SHG FROG} \\ E(t)^2 E(t - \tau) & \text{for THG FROG} \end{cases} \quad (2.24)$$

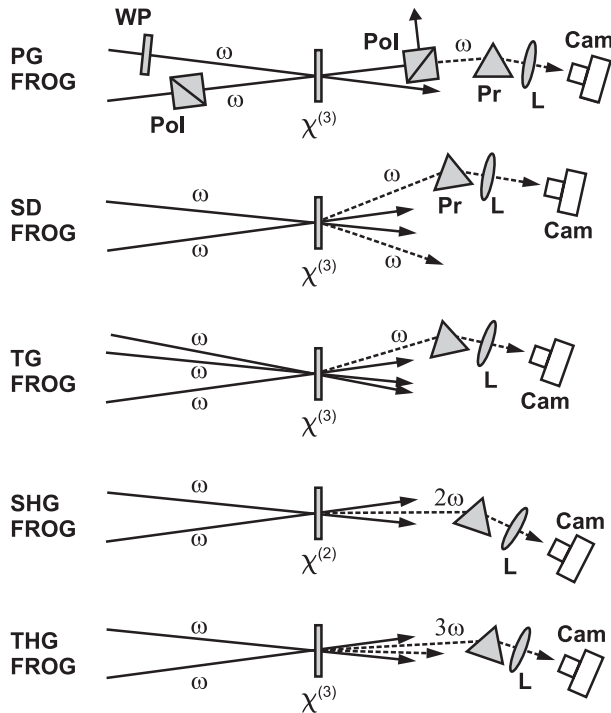


**Figure 2.9:** Different beam geometries for FROG measurements of ultrashort laser pulses. Top to bottom: polarization gate, self-diffraction, transient grating, second-harmonic generation, and third-harmonic generation FROG. Solid lines: input pulses, and dashed lines: signal pulses. The prism-lens combination represents an optical spectrometer. The nonlinearity of the nonlinear medium is displayed with either  $\chi^{(2)}$  or  $\chi^{(3)}$ . The frequencies shown ( $\omega$ ,  $2\omega$ ,  $3\omega$ ) denote the carrier frequencies of the involved pulses, revealing whether the signal pulse has the same carrier frequency as the input pulse or is shifted, as in SHG and THG. Pol: polarizer. WP: waveplate. Pr: prism. L: lens. Cam: camera. Adapted from [48, 56]

Note that the expression for TG FROG is omitted since it has the same expression as either PG- or SD FROG, depending on which of the two replicas is temporally varied [48]. PG- and SHG FROG have been extensively used in this work and will be discussed in more details in section 2.2.1.

## 2.2 Reviewed Data on the Control of Ultrashort Laser Pulses

This section includes the main experimental results on control of ultrashort laser pulses, which have served as useful tools to *perform* experiments as well as to *analyze* the experimental findings on clusters introduced in the subsequent chapter. We first briefly introduce the experimental setups, including an amplified laser chain and a number of optical and diagnostic arrangements. Then the results will be presented in fourth categories: (i) Generation of bandwidth-limited pulses as a simple illustration of the closed-loop feedback control approach; (ii) Shaper-assisted removal of the time-ambiguity in SHG FROG; (iii) The colored double-pulse fitness landscape technique as an open-loop control scheme to study the strong-field response of clusters; and (iv) Colored pulse trains for restricted closed-loop adaptive control. Part of the results have been published in refereed journals and can be found in the Publications (A.1.1, A.1.2, and A.1.5).

## 2.2.1 Experimental Details

### CPA Laser System

In the following we introduce the commercial high-power laser system used for all experiments presented in this thesis. A sketch of the laser chain is shown in Fig. 2.10, including three main parts: (i) a femtosecond oscillator, (ii) a pulse shaper, and (iii) an CPA-based laser amplifier.

#### *Femtosecond Oscillator*

The Ti:sapphire-based oscillator<sup>7</sup> is a commercial device designed similar to the setup described in Appendix B.1. A 5 W diode-pumped Nd:YVO<sub>4</sub> laser<sup>8</sup> at 532 nm is utilized as an optical pump. The presence of a pair of translation-controlled prisms is to manage the intracavity dispersion. The cavity can operate in either a cv-mode or pulsed mode, depending on the positions of the end-mirrors.<sup>9</sup> Typically, the cv-mode is usually first applied to optimize the laser power. By moving one of the end-mirrors to a specific position and then slightly slapping onto one of the prisms, the pulsed mode can be initiated through the Kerr-lens mode-locking (see also Fig. B.6). The oscillator potentially provides sub-12 fs seed pulses with a 4 nJ pulse energy at a central wavelength 800 nm and a 94 MHz repetition rate.

#### *Pulse Shaper*

Prior to amplification, the seed pulses enter an acousto-optic device, the acousto-optic programmable dispersive filter<sup>10</sup> (AOPDF), introduced in detail in section 2.1.2 and Appendix B.4. The AOPDF is based on a 25 mm-long TeO<sub>2</sub> crystal which allows for a maximum accessible group delay of about 3 ps with a spectral resolution of  $\sim 0.6$  nm [90].

Spectral phase and amplitude can simultaneously be modulated by a delivered software, either in a manual or automatic manner. Simple modulation procedures of, e.g., Gaussian profiles or Taylor phase terms  $\phi_n$  (Eq. (2.10)) can be manually addressed from the software interface. Due to possible damage to the AO device, arbitrary modulation of the pulse has to be fulfilled through a so-called remote mode in the program. In this mode, the controlled program continuously loads a *computed* phase-and/or-amplitude information from a certain memory in the computer and sends it to the rf-generator to insert the desired modulation onto the pulse.

The installation of the pulse shaper before an amplifier allows for modulation of ultrashort pulses at high intensities ( $> 10^{16}$  W cm<sup>-2</sup>). We however note that some restrictions for the amplitude modulation need to be taken into account because too narrow-

---

<sup>7</sup>Model MTS, KMLabs.

<sup>8</sup>Model Millennia Vs, Spectra-Physics.

<sup>9</sup>For an explanation about this mechanism, see, e.g., Ref. [129].

<sup>10</sup>Model Dazzler, Fastlite.

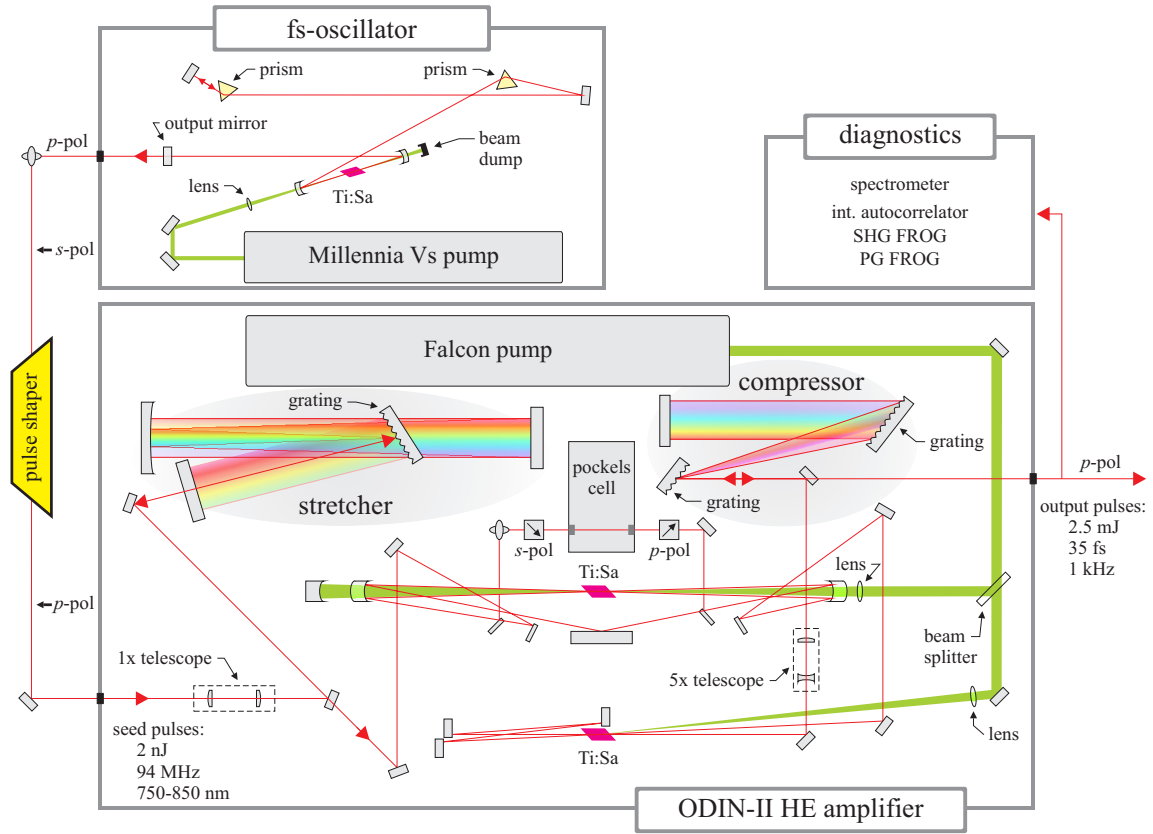


**Figure 2.10:** Schematic view of the chirped pulse amplification laser system (ODIN-II HE). See text for more details.

bandwidth ( $\ll 5$  nm-FWHM) pulses might cause damage in the subsequently situated amplifier. Additionally, nonlinear distortions of the tailored pulses in the CPA might occur resulting in nonlinear pulse shaping as detailed in Publications A.1.1.

### Amplified Laser System

After the acousto-optic pulse shaper, the seed pulses are fed into a chirped pulse amplification laser system,<sup>11</sup> including three main setups: an optical pulse stretcher, a double stage amplification, and an optical pulse compressor. Details on modern CPA designs can be found in, e.g., Refs. [53, 129, 130]. Briefly, the seed pulses are stretched in the pulse stretcher by a factor of about  $10^4$  in duration resulting in a peak intensity below thresholds of optical damages and nonlinear effects in the subsequent amplification stages.

Leaving the pulse stretcher with a duration of about 200 ps, the pulses are then amplified in Ti:Sa crystals through two stages. A 25 W Nd:YLF laser with a central wavelength 527 nm is used to pump for both stages, 22% of the pump power for the first and the rest for the second. The first stage is an eight-pass *high-gain* amplification which amplifies the pulse energy by  $\sim 10^7$ , i.e., from 2-4 nJ to  $\sim 200$   $\mu$ J. After the first four passes, the repetition rate of the system is reduced to 1 kHz by using a combination of a pockel's

<sup>11</sup>Model ODIN II-HE, Quantronix.

cell and a polarizer-analyzer pair. For further suppression of the amplified spontaneous emission [131], an eight-hole spatial filter is installed in between a curved mirror and the laser medium.

The second two-pass *high-power* amplification further boosts the pulse energy up to about 4 mJ. After compressing with a double-grating based pulse compressor, the system delivers amplified pulses having an energy of up to 2.5 mJ, sub-40 fs duration (FWHM) and a repetition rate of 1 kHz at about  $\lambda_0 = 810$  nm central wavelength. Nonlinear effects such as self-phase modulation, gain-narrowing, and gain-saturation might occur through the amplifier leading to the accumulation of high-order dispersion of the pulses, which could not completely be compensated by a standard pulse compressor. In our system, pulses shorter than  $\sim 30$  fs can be obtained by first (i) applying a suitable spectral filter to the input spectrum and then (ii) employing a closed-loop optimization scheme to precompensate for the residual dispersion in the CPA [90].

The over 15 m-long air-propagation of the intense ultrashort laser pulses to the location of the experiments leads to serious self-focusing and self-phase modulation (see Appendix B.3). It is therefore desired to skip the internal compressor and compress the amplified pulses right before the interaction chamber. An external grating (1200 grooves/mm, incident angle  $23^\circ$ ) compressor with a similar design as the commercial one (Fig. 2.10) is built for this aim. With the use of the home-built compressor, laser pulses as short as 35 fs have been routinely achieved.

We note here some practical methods to optimize the external optical compressor. First, high-order dispersion can be compensated to a certain extent by slightly rotating both the grating parallel together from their standard angular settings (relative deviation  $< 2^\circ$ ). Second, by focusing the compressed pulse in the air with a short focal length mirror and varying the distance between the two gratings to find the brightest plasma emission, the compressor setting for shortest-possible durations can be roughly determined. Further fine precompensation of dispersion can be achieved with help of the pulse shaper combined with an open-loop or closed-loop control scheme as presented in section 2.2.2.

### Double-pulse Based Third-Harmonic Generation Setup

In sections 2.2.4 and 2.2.5, we will introduce the generation of colored pulse trains, which have extensively been used in open-loop as well as closed-loop control schemes for the studies in this text. To demonstrate the impact of the colored multipulses, we have chosen a well-documented optical system for the third-harmonic generation. First introduced by Vogt *et al.* [45], the system has some special features: (i) a double-pulse with an appropriate optical delay results in a maximum THG yield; (ii) the corresponding leading pulse is remarkably more intense than the trailing; and (iii) under certain phase-mismatches occurring in the nonlinear crystals the trailing pulse is either red- or blue-shifted.

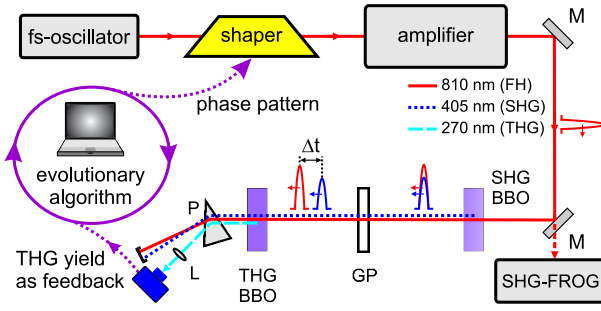


**Figure 2.11:** Experimental setup for double-pulse based third-harmonic generation. A glass plate (GP) was used to temporally separate the first (810 nm) and second-harmonic (405 nm) by about  $(310 \pm 20)$  fs. Thus, for sum-frequency mixing ( $\omega + 2\omega \rightarrow 3\omega$ ), double pulses are necessary to create the third-harmonic (270 nm) efficiently. See text for additional details. M: flat mirrors. P: prism. L: lens. BBO: Beta-Barium-Borate crystals.

In our approach, the experimental setup was slightly simplified as sketched in Fig. 2.11. In brief, the fundamental (FH, 810 nm) optical pulse from the CPA laser was frequency doubled in a SHG-crystal.<sup>12</sup> After leaving the frequency-doubler, the fundamental and SHG (405 nm) pulses temporally and spatially overlapped to generate the third-harmonic (270 nm) light in a frequency-tripler.<sup>13</sup> A piece of glass GP<sup>14</sup> was inserted in between the nonlinear crystals to shift the 810 nm pulse about  $\Delta t \approx 310 \pm 20$  fs ahead of the 405 nm pulse. This significantly reduced their temporal overlap, leading to a decrease in the THG yield. The third-harmonic was then spatially separated from the other beams by a prism P ( $60^\circ$ , quartz) and detected by a high resolution spectrometer HR4000.<sup>15</sup> The integrated THG signal served as the feedback value for the closed-loop adaptive control experiments described later.

## Polarization-Gate FROG

Polarization-gate (PG) FROG uses the polarization-gate beam geometry as shown in Figs. 2.9 and 2.12(a), and described in great detail in Refs. [48, 56]. Briefly, the pulse to be measured is split into two replicas. One replica (the *probe*) is sent through a pair of crossed polarizers and then fed into a spectrometer, while the other (the *gate*) is sent through a  $\lambda/2$ -waveplate to achieve a  $\pm 45^\circ$  linear polarization with respect to the probe. Both pulses are then spatially overlapped in a third-order nonlinear medium, e.g., a piece of fused silica. In the nonlinear medium, the gate pulse induces a birefringence through the *electronic* Kerr effect [121] which results in a slight rotation of the probe pulse's polarization allowing light to be transmitted through the analyzer. By recording the spectrum of the signal pulse as function of the probe-gate optical delay, a PG FROG trace is measured and given as

$$I_{\text{FROG}}^{\text{PG}}(\omega, \tau) = \left| \int_{-\infty}^{\infty} E(t) |E(t - \tau)|^2 \exp(-i\omega t) dt \right|^2. \quad (2.25)$$

<sup>12</sup>A type-I BBO crystal ( $\omega + \omega \rightarrow 2\omega$ ), thickness  $100 \mu\text{m}$ , phase-matching (PM) angles  $\theta = 29.2^\circ$  and  $\varphi = 0^\circ$ .

<sup>13</sup>A type-II BBO crystal ( $\omega + 2\omega \rightarrow 3\omega$ ), thickness  $150 \mu\text{m}$ , PM angles  $\theta = 55.5^\circ$  and  $\varphi = 30^\circ$ .

<sup>14</sup>Quartz SQ1, thickness  $\sim (2.0 \pm 0.1)$  mm.

<sup>15</sup>Model HR4000, Ocean Optics.

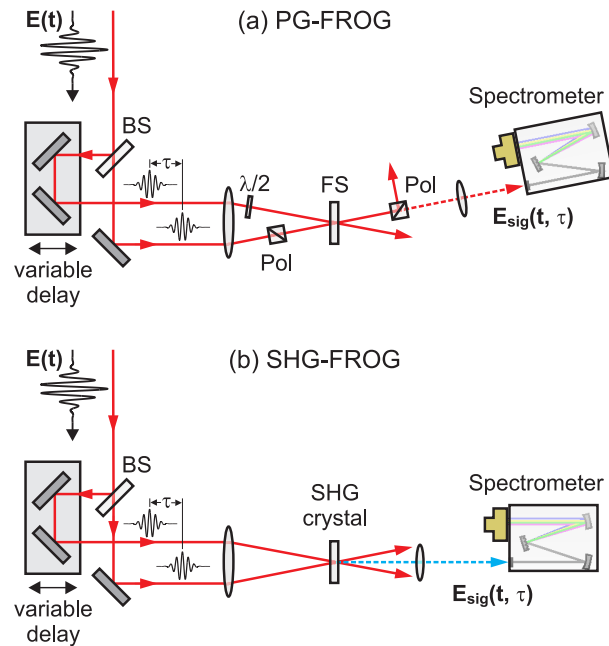


**Figure 2.12:** Experimental setups of a PG FROG (a) and SHG FROG (b). Adapted from [48]

Note that the gate function in PG FROG,  $|E(t-\tau)|^2$ , is a real quantity and hence adds no phase information to the gated slice of the probe pulse. Consequently, PG FROG traces are very intuitive, illustrating quite accurately the joint time-frequency representation of the pulse (section 2.1.1).

PG FROG however has some undesirable drawbacks. It requires extreme high-quality polarizers with an extinction coefficient better than  $10^{-5}$  over a broad wavelength range. Such high-quality polarizers, which are not available for reflecting optical elements and in the deep UV ( $< 250$  nm), introduce a substantial material dispersion into the probe pulse. Furthermore the input and signal pulses have the same carrier frequency causing a low signal-to-noise ratio.

In our *home-built* multishot PG FROG apparatus, a broadband  $2\ \mu\text{m}$ -thick beamsplitter<sup>16</sup> is used to create pulse replicas. To minimize material dispersion, a pair of crossed thin-film polarizers<sup>17</sup> is used. Additionally, an out-of-plane optical path [48, 132] is implemented to achieve the  $\pm 45^\circ$  polarization-rotating for the gate, instead the use of a transmitting  $\lambda/2$ -waveplate. The pulses are then spatially overlapped and focused with a parabolic mirror ( $f = 15$  cm) on a  $150\ \mu\text{m}$ -thick piece of fused silica. Finally, the signal is spectrally resolved with the high-resolution spectrometer HR4000.

With a slight change this setup can also be employed for a SHG FROG or an intensity autocorrelator. An example of PG FROG measurements performed with the device is illustrated in Fig. 2.13. Further details can be found in Publications A.1.1.

<sup>16</sup>Pellicle, Thorlabs (Wavelength range 700-900 nm; Transmission 55%; Reflectance 45%).

<sup>17</sup>LPNIR050-MP, Thorlabs (a linear polarizer, wavelength range 650-2000 nm, thickness  $220 \pm 50\ \mu\text{m}$ , with an extinction coefficient of better than  $10^{-6}$  in the spectral range of interest).



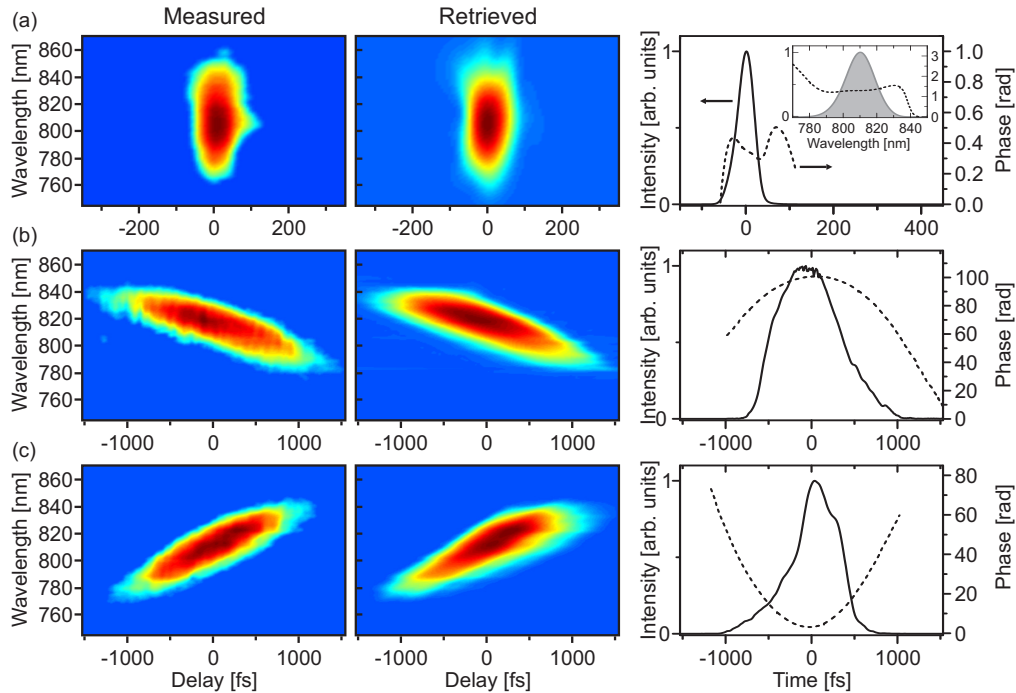


**Figure 2.13:** Example of PG FROG measurements of (a) a 35 fs bandwidth-limited pulse, (b) a positively chirped ( $+7500 \text{ fs}^2$ ) pulse and (c) a negatively chirped ( $-4500 \text{ fs}^2$ ) pulse. Left column: measured traces. Middle column: computed traces of the corresponding retrieved pulses. Right column: retrieved intensities (solid) and phases (dashed) vs. time. Inset: retrieved spectrum and spectral phase for the case (a). All FROG errors  $< 0.01$ . Note the changes in scale of the time and phase axes.

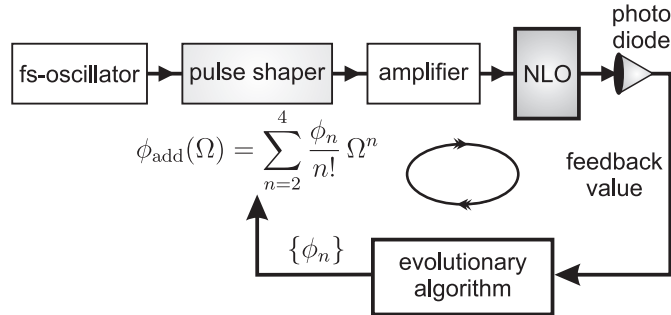
## Second-Harmonic Generation FROG

Although providing intuitive traces, PG FROG geometry is not dispersion- and signal-to-noise ratio optimized. On the other hand, a simple version of FROG, as called earlier the SHG FROG, can be obtained from an available PG FROG setup by (i) simply removing the polarizers and the  $\lambda/2$ -waveplate and (ii) replacing the piece of fused silica with a SHG-crystal,<sup>18</sup> e.g., an BBO- or KDP crystal. The signal pulse now has a doubled-frequency as the input one. Like intensity autocorrelation, SHG FROG trace is a symmetric function of optical delay  $\tau$  and given by Eq. (2.22).

SHG FROG has several advantages as discussed in detail by Trebino [48]. For the serve of SHG FROG in this work, we briefly introduce the most important points which make SHG FROG our choice. First, SHG FROG is very sensitive compared to other FROG geometries [48], making use of the second-order, rather than third-order, nonlinearity. Further, the signal pulse has a different color and polarization from the input light allowing for effective background suppression. This gives SHG FROG a higher dynamics range than any other characterization technique available to date. Second, the simple SHG FROG setup allows to exactly measure laser pulse, even precisely at the position of the sample by interchanging the sample with a nonlinear medium for optical gating. The

<sup>18</sup>In our setup, a type I-BBO crystal is used (thickness  $20 \mu\text{m}$ , PM angles  $\theta = 29.2^\circ$  and  $\varphi = 0^\circ$ ).

**Figure 2.14:** Closed-loop adaptive control setup to precompensate for the dispersion in the CPA laser system. The nonlinear optical signal NLO (e.g., SHG or PG-yield) measured with a photodiode is assigned as feedback value. Here,  $\Omega = \omega - \omega_0$  is the relative frequency about the carrier frequency  $\omega_0$ .



only optical element changing the pulse in the SHG FROG geometry turns out to be the beamsplitter used to produce the replicas. But ultrathin beamsplitters (down to  $2\ \mu\text{m}$ ) are now available commercially minimizing material dispersions.

There are however two main classes of ambiguities present in SHG FROG traces. First, it has a relative-phase ambiguity for two (or more) well-separated pulses. For instance, the relative phases,  $\phi$  and  $\phi + \pi$ , give the same SHG FROG trace and thus cannot be distinguished. This ambiguity can easily be resolved by analyzing the knowledge of the fundamental spectrum in addition. Second, SHG FROG has an ambiguity in the direction of time: A pulse and its time-reversed replica yield the same SHG FROG trace. As a result, for a measured SHG FROG trace there are two possible retrieved solutions. There are a number of ways to remove this time ambiguity described elsewhere [48, 101, 133]. In this work, two practical methods based on a pulse shaper have been developed and will be described in section 2.2.3.

## 2.2.2 Pulse-Precompression with Closed-Loop Feedback Control

This section demonstrates a simple example of a closed-loop feedback control experiment to achieve the shortest-possible (bandwidth-limited) pulses. The technique makes use of the PG FROG setup<sup>19</sup> described above and assigns the PG yields as feedback values for the closed-loop optimization (section 2.1.2). By adaptively adding a spectral phase function<sup>20</sup>

$$\phi_{\text{add}}(\omega) = \sum_{n=2}^4 \frac{\phi_n}{n!} (\omega - \omega_0)^n \quad (2.26)$$

to the amplified pulse to precompensate for the residual spectral phase  $\phi_{\text{res}}$ , and hence to maximize the PG yield, bandwidth-limited pulses can be obtained. The experimental setup is sketched in Fig. 2.14.

An optimization search method based on an evolutionary algorithm (EA) [111, 113] was used to attain the spectral phase function giving the maximum PG yield. Briefly, an

<sup>19</sup>We note however that SHG, THG, or any other nonlinear processes can also be used for this purpose.

<sup>20</sup>Typically, up to fourth-order terms in the Taylor series are necessary.

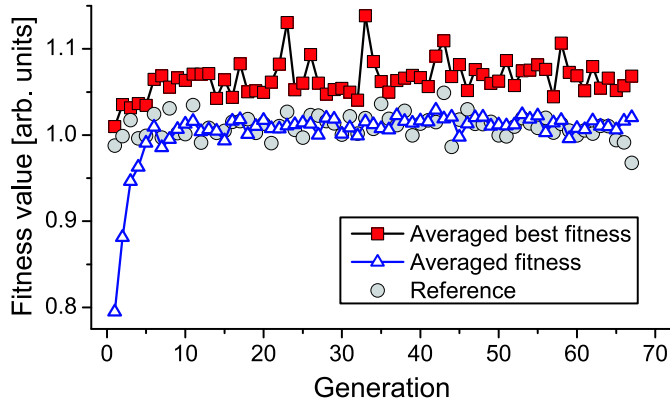


**Figure 2.15:** Evolution of averaged fitness values vs. generation in the closed-loop adaptive optimization of the PG yield. After each generation, the average of the fitness values over the ten best individuals gives the averaged best fitness and over the whole population (50 individuals) is the averaged fitness. The reference signal is measured with the start pulse (60 fs) that is depicted in Fig. 2.16(c) and (d).

initial population consists of 50 arbitrary individuals  $\{\phi_{\text{add}}^{(k)}\}$  (with  $k = 1, 2, \dots, 50$ ). Each individual is encoded by a set of the Taylor coefficients  $\{\phi_n\}$  (with  $n = 2, 3, 4$ ) according to Eq. (2.26). After each evolutionary step, a new population is created by selection and subsequent modification with recombination (crossover) and mutation operators (see Appendix. B.5 and Ref. [113] for details).

To monitor the search, an averaged fitness value of the *ten best individuals* after each cycle is extracted. The evolution of this value vs. generation is displayed in Fig. 2.15, in comparison with the reference value recorded at the start of each generation as well as with the fitness value averaged over the whole population. Typically, the algorithm converges after 20-50 generations. Figure 2.16 shows the adaptively determined pulse (top), which is shorter in time and has almost no chirp in comparison with the start pulse (bottom).

### 2.2.3 Shaper-assisted removal of the time-ambiguity in SHG FROG traces

In optimal control experiments on laser-matter interactions, it is crucial to completely characterize the tailored pulses, i.e., in both amplitude and phase. Among other diagnostic techniques, SHG FROG provides full information of the pulse but has a direction-of-time ambiguity (DOTA) due to its symmetric trace with respect to the optical delay. This problem can be solved if we know in advance some features of the pulse such as its chirp (positive or negative) or its temporal structure (with pre- or postpulses). In this section two pulse shaper-based methods to solve the problem will be presented, i.e., the *phase-only* and *amplitude-and-phase* approaches. Additional details about the latter can also be found in Publications A.1.2.

#### Phase-only Approach

If the amplified pulse is initially precompensated,  $\psi_{\text{ini}}(\omega) \approx 0$ , as introduced above, then the spectral phase  $\psi_{\text{exp}}(\omega)$  of the later phase-only tailored pulse can be approximated

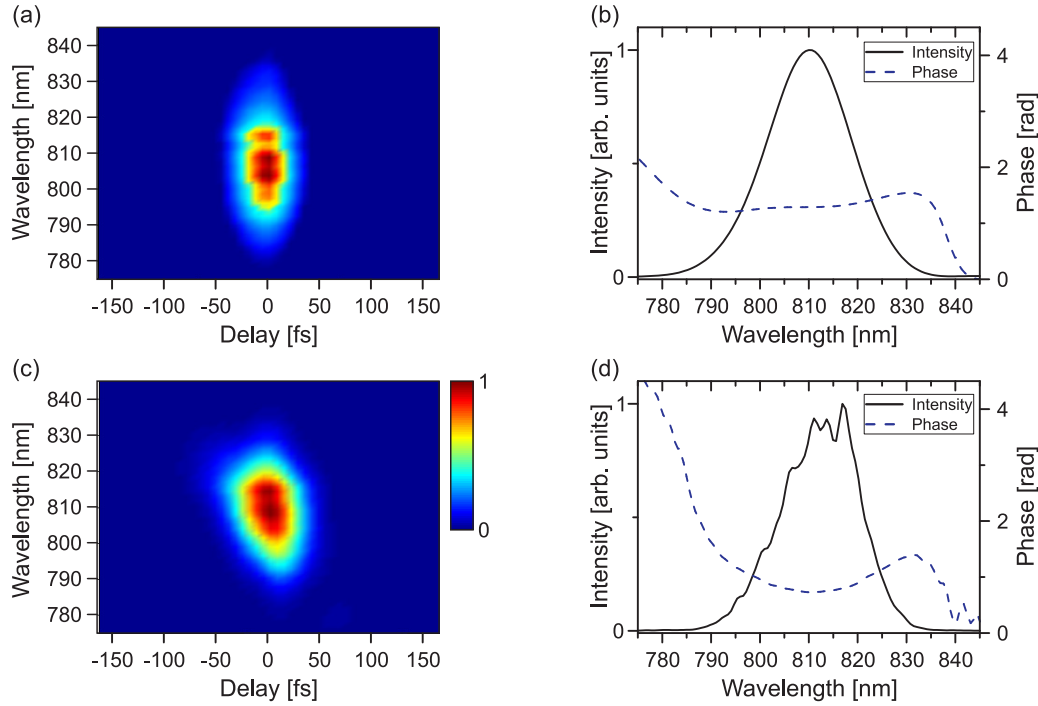


**Figure 2.16:** Bandwidth-limited pulse (top,  $\tau_{\text{opt}} = 35$  fs) obtained through the closed-loop optimization of dispersion in the CPA system. The start pulse (bottom,  $\tau_{\text{ini}} = 60$  fs) is positively chirped and displayed for comparison. Left column: the corresponding measured PG FROG traces; right column: the respective intensities and phases vs. wavelength.

to the programmable spectral phase function  $\Phi_{\text{sh}}(\omega)$  added by the pulse shaper to the original pulse shape, i.e.,  $\psi_{\text{exp}}(\omega) \approx \Phi_{\text{sh}}(\omega)$ . This approximation is based on the fact that the programmed spectral phase function almost preserves its shape through the amplification stage as proven in Refs. [134, 135] and Publications A.1.1. Therefore, the electric field calculated from the measured spectrum and the spectral phase  $\Phi_{\text{sh}}(\omega)$  gives a close reference to the pulse to be measured.

To demonstrate the method, we show in Fig. 2.17 a pulse measured with SHG FROG and its corresponding calculated one. The pulse is quite complex and was determined in an optimal control experiment on xenon clusters. Due to its similarity to the measured pulse as clearly seen in Fig. 2.17, the computed pulse in both representations (time- and Husimi domains) gives an intuitive reference to choose the correct solution (Fig. 2.17(a), solid) delivered by the FROG algorithm. The precision of this method strongly depends on how well the initial phase term  $\psi_{\text{ini}}(\omega)$  is precompensated. A non-zero  $\psi_{\text{ini}}(\omega)$  might lead to a slight deviation between, e.g., the retrieved and computed pulses as seen in Fig. 2.17(a)–(c).

### Amplitude-and-Phase Approach

With an amplitude-and phase pulse shaper, one can easily solve the time ambiguity by adding a small delayed satellite to the original pulse structure to determine the time

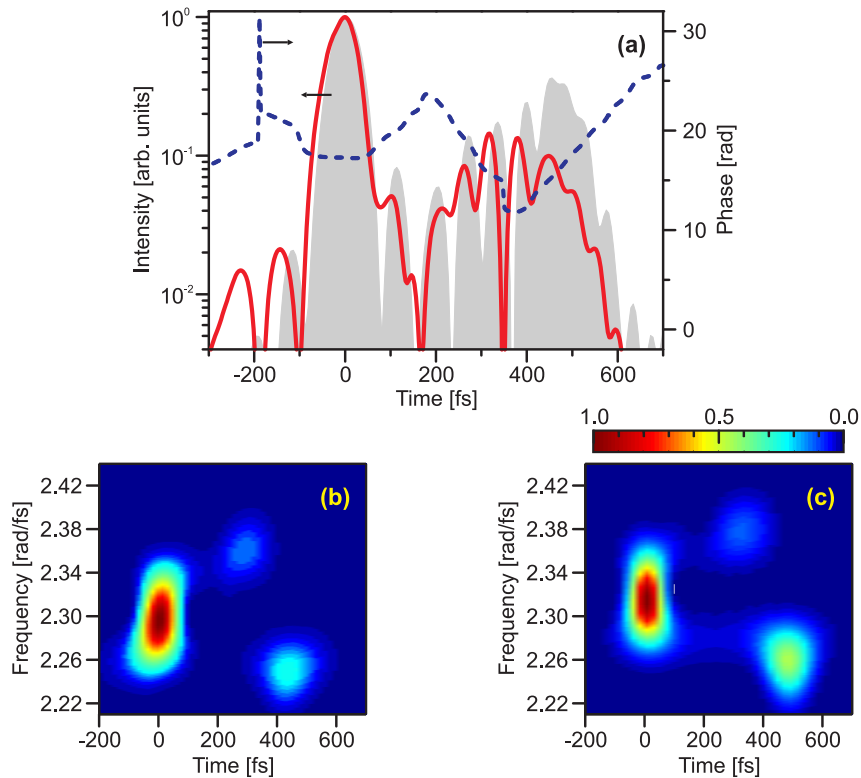


**Figure 2.17:** Comparison between a measured pulse and its computed one based on the programmable spectral phase  $\Phi_{\text{sh}}(\omega)$  and the measured spectrum. Top: Retrieved (solid) and computed (gray-filled) intensities and retrieved phase (dashed) vs. time. Bottom: Husimi distributions of the retrieved pulse (b) and computed pulse (c). See text for further details.

direction. In brief, a second FROG trace of the modified pulse (with the added satellite) is measured and then run on the FROG algorithm. With the predetermined satellite only one solution from the modified FROG trace is possible. By comparing the retrieved pulses of the original with its modified structure, one gets the correct solution.

It is well-known in femtosecond pulse shaping that a pulse shaper which is capable of both phase and amplitude modulation can generate trains of pulse replicas with variable delays and relative pulse intensities [68, 102, 136]. Therefore, with the pulse shaper (Dazzler) already available in the CPA chain, we add a *small satellite* (either a leading or trailing pulse) into the original pulse structure to determine the time direction. Using the home-built PG FROG, we have proven that (i) the added pulse uniquely defines the time direction after the amplification stage, and (ii) even with the presence of the small pulse added the original pulse structure is nearly unchanged through the CPA. The latter is illustrated in Fig. 2.18, in which the original pulse A is shown in comparison to a modified pulse with either prepulse (B) or postpulse (C) added.

We note that there have been a number of pulse shaper-assisted techniques developed for ultrashort pulse characterization [102, 136, 134, 137]. A detailed discussion of the advantages of our method compared to others can be found in Publications A.1.1.

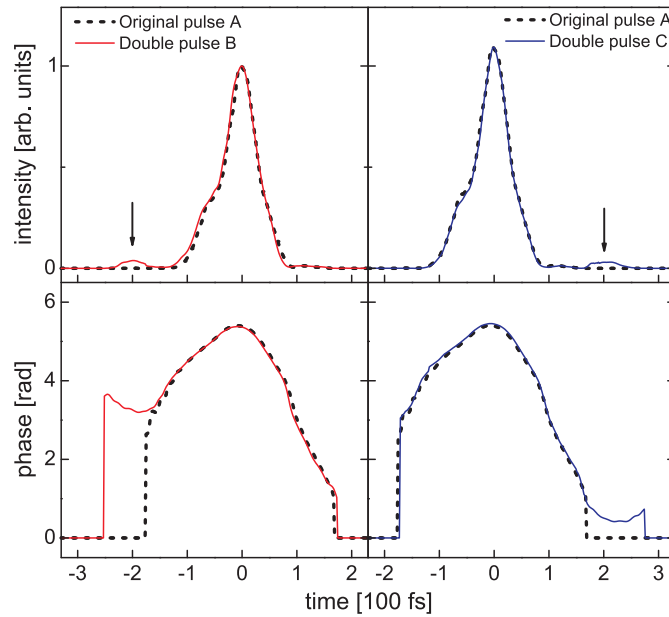


**Figure 2.18:** Original (A) and modified (B or C) pulses in demonstration of the DOTA-method based on an amplitude-and-phase pulse shaper. See text for more description.

## 2.2.4 Colored Double Pulses: Generation, Characterization and Applications

The general challenge encountered free-optimization, or also nonrestricted, experiments and simulations using a closed-loop feedback control scheme [41] is *twofold*. First, there are usually too many parameters encoded in the self-learning algorithm which lead in some cases to an inefficient (slow) or even unsuccessful search, where the acquirement of feedback values is really time-consuming. Second, the obtained optimal solution may contain substructures which contribute to a particular control mechanism to different degrees [138]; or different pulse shapes can also lead to similar fitness values. Consequently, the analysis of the underlying mechanism from the optimal pulse shape is challenging.

In order to get more insights into the system under investigation, it is sometimes useful to restrict the number of possible pulse shapes. Within this context, to investigate the shaped laser-cluster interactions we have applied two approaches: (i) the open-loop control scheme, or also the fitness landscape technique, with use of colored double pulses, and (ii) the closed-loop control scheme limited to colored pulse trains. This section covers the generation and characterization of colored double pulses, and an introduction to the fitness landscape technique. The next section deals with colored pulse trains and their applications.

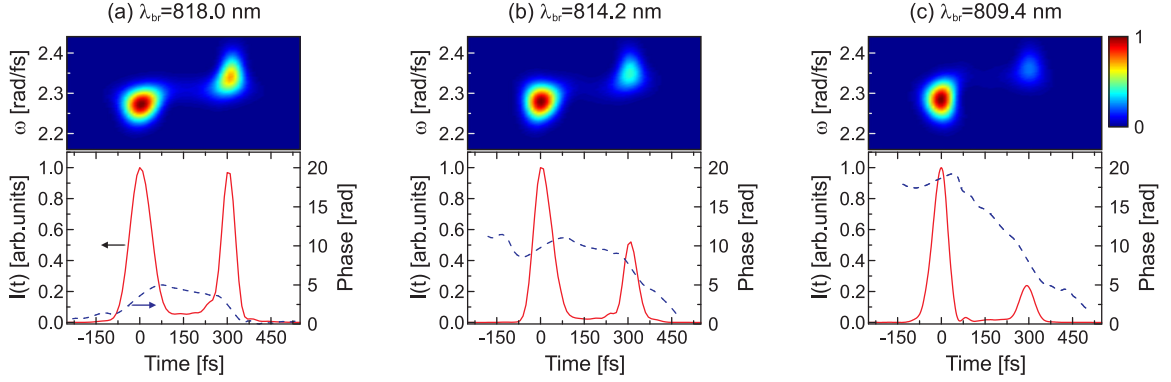


**Figure 2.19:** SHG FROG measurements of colored double-pulses, tailored through a triangular spectral phase function with a constant pulse separation  $\tau = 300$  fs and different selected spectral breakpoint wavelengths: (a)  $\lambda_{\text{br}} = 818.0$  nm, (b)  $\lambda_{\text{br}} = 814.2$  nm, and (c)  $\lambda_{\text{br}} = 809.4$  nm. Top: the Husimi distributions, bottom: the corresponding intensities and phases vs. time.

## Generation and Characterization

Colored double-pulses (CDPs) generated with a phase-only pulse shaper were first experimentally demonstrated by Renard *et al.* [59] and then have widely been applied as the quantum control fitness landscape technique by Gerber’s group [45, 60, 139]. CDPs can be simply created by applying a triangular spectral phase function of the form:

$$\Phi_{\text{CDP}}(\omega) = \frac{\tau}{2} |\omega - \omega_{\text{br}}|, \quad (2.27)$$

where  $\tau$  is the *double pulse separation* (or also double triangular phase slope) and  $\omega_{\text{br}} = (\omega_0 + \delta\omega)$  is the spectral phase breakpoint<sup>21</sup> that is where the laser spectrum is split into a *red* (low-frequency) and a *blue* (high-frequency) part. For a positive  $\tau$ , the ”red” part is shifted forwards by  $\tau/2$  in time whereas the ”blue” part is shifted  $\tau/2$  backwards, resulting in a red-detuned leading pulse and a blue-detuned trailing pulse. This is vice versa for negative  $\tau$ , i.e., a blue-detuned leading pulse followed by a red-detuned one. It is useful to define the relative intensity ratio of colored double pulses as the ratio between leading and trailing pulse intensities,  $I_{\text{CDP}} = I_{\text{pre}}/I_{\text{post}}$ . Because the leading and trailing pulse exchange their order in time with the sign of  $\tau$ , thus  $I_{\text{CDP}}^{(\tau>0)} = 1/I_{\text{CDP}}^{(\tau<0)}$ .

On the one hand, it has been proven that the parameter  $\tau$  allows for changing the optical delay of the colored double-pulse without significant variation of the pulse widths [59, 60]. Pump-probe like experiments can thus be conducted with a single laser beam, as an alternative to the standard methods such as the Mach-Zehnder interferometer. On the other hand, the choice of the spectral phase breakpoint  $\omega_{\text{br}}$  permits to control the relative intensity ratio of colored double-pulses. In practice, the single-beam and adjustable two-color mode have widely been employed in ultraviolet fs pulse shaping [140],

<sup>21</sup>For practical reasons, to indicate the spectral phase breakpoint we often use  $\omega_{\text{br}}$  for mathematical descriptions and  $\lambda_{\text{br}} = 2\pi c/\omega_{\text{br}}$  for presentation of experimental results.

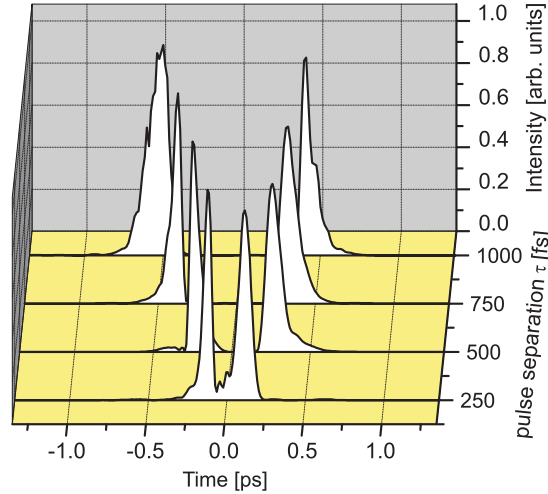
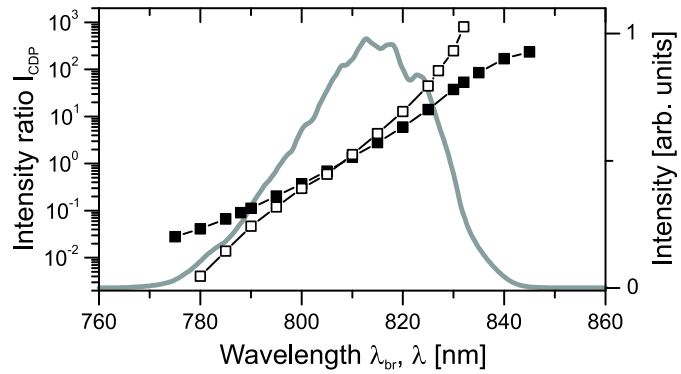


**Figure 2.20:** SHG FROG measurements of colored double pulses, tailored through a triangular spectral phase function with variable pulse separation  $\tau$  and a constant spectral phase breakpoint  $\lambda_{br} = 820$  nm.

**Figure 2.21:** Calculated ( $\blacksquare$ ) and measured ( $\square$ ) relative intensity ratio  $I_{CDP}^{(\tau < 0)}$  vs. the spectral breakpoint wavelength. The laser spectrum (solid line) is depicted for comparison. Note that an over five orders of magnitude dynamic range of  $I_{CDP}$  can be obtained. Due to nonlinear effects in the CPA system a small shift between the experimental and calculated values is observed.



coherent control [45, 141, 142, 143, 144, 145], laser ablation of semiconductors [146] and intense laser-cluster interactions [147, 148, 149].

Examples of colored double-pulses tailored through triangular spectral phase functions with  $\lambda_{br}$  and  $\tau$  are shown in Fig. 2.19 and Fig. 2.20, respectively. In our case, we need to take into account the influence of the CPA installed after the pulse shaper. Nonlinear effects such as gain-narrowing and saturation in CPA lead to the redistribution in the laser spectrum and thus change the relative intensity ratio  $I_{CDP}$  as illustrated in Fig. 2.21.

### Colored Double-Pulse Fitness Landscape Technique

The possibility to programmably alter the temporal delay and relative intensity ratio of colored double pulses makes them a powerful tool to study pump-probe effects. A fitness landscape of a signal of interest can be easily obtained by systematically scanning the parameters  $(\tau, \lambda_{br})$ . This allows for investigating both time- and also energy distribution-resolved effects, suitable for instance to study the energy absorption vs. time in clusters. Such an open-loop scheme is termed as *colored double-pulse fitness landscape technique* (CDPFL), which will be extensively used to study the intense laser-cluster interactions



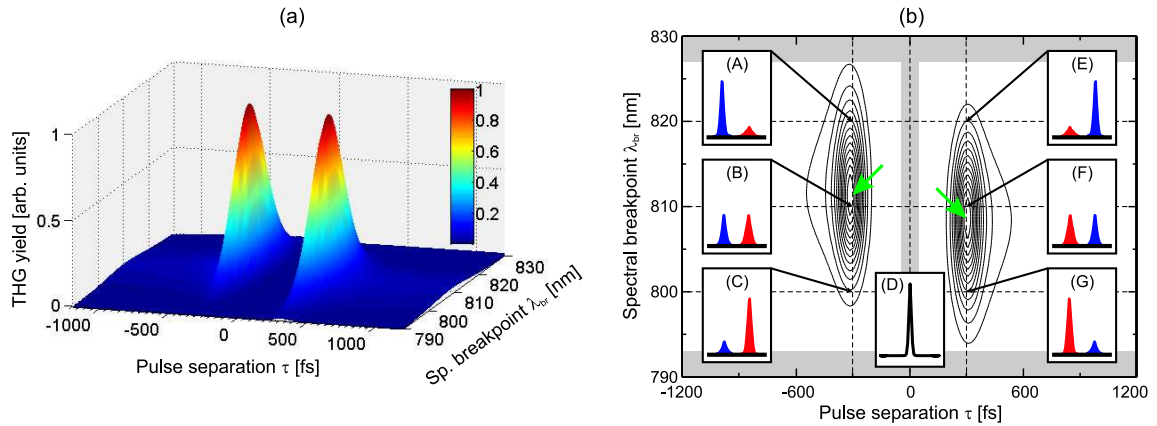


**Figure 2.22:** Left: Calculated colored double-pulse fitness landscape of the THG signal in the setup in Fig. 2.11. Right (insets): CDP temporal profiles for some particular points in the THG-landscape. The color in each pulse denotes the corresponding main spectral components. The THG yield (contour lines) is shown again for comparison. In the landscape, two equal maxima (marked by green arrows) of the THG yield are found displaced from the central wavelength 810 nm. In the roughly-indicated gray region where either  $\tau \sim 0$  fs, or  $\lambda_{br}$  is near 790 nm or 830 nm of the spectrum, the CDPs show up as single pulses (inset (D)). See text for additional details.

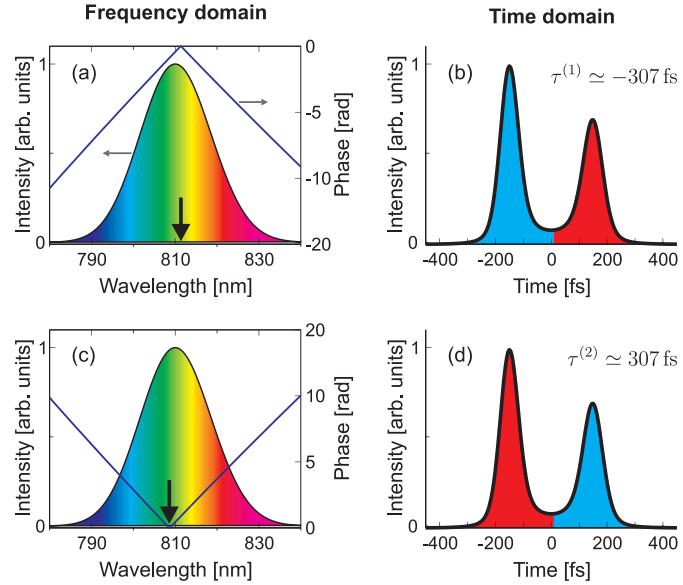
(see Publications A.1.6, A.1.7, and A.1.8).

Due to the nonlinear dependence of the relative intensity ratio in the spectral breakpoint wavelength (see Fig. 2.21), the obtained  $(\tau, \lambda_{br})$ -landscape usually provides an un-intuitive picture and corresponding elaborate analysis have to be performed to extract the information. To first illustrate the impact of the programmable parameters  $(\tau, \lambda_{br})$  on such a landscape, we follow Vogt *et al.* [45] to calculate CDPFL of the third-harmonic generation in the setup shown in Fig. 2.11. For simplicity, we set the optical delay between the fundamental (810 nm) and the second-harmonic pulses  $\Delta t = 300$  fs in the simulation.

Figure 2.22 shows the computed CDPFL of the THG yield (left) and the temporal profiles of CDPs for some specific points in the landscape (right) as analytic tools. Two equal maxima of the THG signal are found in the landscape with corresponding settings of (i)  $(\lambda_{br}^{(1)} \simeq 811.35 \text{ nm}, \tau^{(1)} \simeq -307 \text{ fs})$  and (ii)  $(\lambda_{br}^{(2)} \simeq 808.65 \text{ nm}, \tau^{(2)} \simeq 307 \text{ fs})$ . Their corresponding optimal CPDs are depicted in Fig. 2.23. For the case (i), for instance, the spectral breakpoint  $\lambda_{br}^{(1)}$  is shifted more to the "red" part of the spectrum giving rise to a colored double-pulse with a more intense blue-shifted leading pulse ( $\tau^{(1)} < 0$ , Fig. 2.23, top). And vice versa for the case (ii),  $\lambda_{br}^{(2)}$  is more shifted to the "blue" region and hence the respective double-pulse has also a stronger, but red-shifted leading pulse ( $\tau^{(2)} > 0$ , Fig. 2.23, bottom).

We note that the THG signal in this case (Fig. 2.11) is purely intensity-dependent when the perfect phase-matching conditions are met. Therefore no difference of the maximal THG yield has been observed if either a blue- or red-shifted pulse comes first. In clusters, as we will show later in Publications A.1.7 and section 3.2.2, a significant enhancement for the highest charge state yields, for example, has been obtained for a certain negative  $\tau$ .

**Figure 2.23:** Colored double-pulses leading to maximal THG yield for negative (top) and positive (bottom)  $\tau$ . Both pulses have very similar temporal profiles although their corresponding spectral breakpoints (marked by arrows) are quite different, i.e.,  $\lambda_{\text{br}}^{(1)} = 811.35$  nm and  $\lambda_{\text{br}}^{(2)} = 808.65$  nm. Their pulse separations are  $\sim \pm 307$  fs, close to the originally given value  $\Delta t$ . In the time domain, the color in each pulse here again indicates the corresponding main spectral components.



In addition, as a general feature of open-loop schemes, the CDPFL technique is restricted in parameters and therefore delivers solutions only *close* to the optimal ones. This might serve as an explanation, e.g., for the small deviation between  $\tau^{(1,2)}$  and  $\Delta t$  observed above.

## 2.2.5 Intense Colored Pulse Trains: Generation, Characterization and Applications

In the following, we extend to phase-only tailored colored pulse trains, but still using the basic concept of triangular spectral phase shaping. More details about this issue can be found in Publications [A.1.2](#).

A more complex multipulse structure can be obtained by superimposing a number of triangular spectral phases (multitriangular, MTA) with different values of  $\tau$  and  $\omega_{\text{br}}$ ,

$$\Phi_{\text{MTA}}(\omega) = \sum_{n=1}^N \Phi_{\text{C2P}}^{(n)}(\omega) = \frac{1}{2} \sum_{n=1}^N \tau_n |\omega - (\omega_0 + \delta\omega_n)|. \quad (2.28)$$

For  $N$  spectral phase breakpoints the laser spectrum divides into  $(N + 1)$  regions and a train of colored pulses ( $\text{C}^{N+1}\text{Ps}$ ) can be formed. Similar to the cases of colored double-pulses, pulse separations and relative intensity ratios can be simultaneously addressed by controlling the parameters  $\tau_n$  and  $\delta\omega_n$ , respectively.

Figure [2.24](#) shows an example of colored triple-pulses ( $N = 2$ ) measured with SHG FROG. Here the time separation  $\tau_2$  is varied while the other parameters ( $\tau_1, \delta\omega_1, \delta\omega_2$ ) are fixed. The evolution of the temporal intensity profiles vs.  $\tau_2$  is displayed in Fig. [2.24\(a\)](#). Whereas slight variations in relative intensity ratios are observed, the experimentally determined delays ( $\tau_1^{\text{exp}}, \tau_2^{\text{exp}}$ ) and their corresponding parameters ( $\tau_1, \tau_2$ ) are in good agreement.

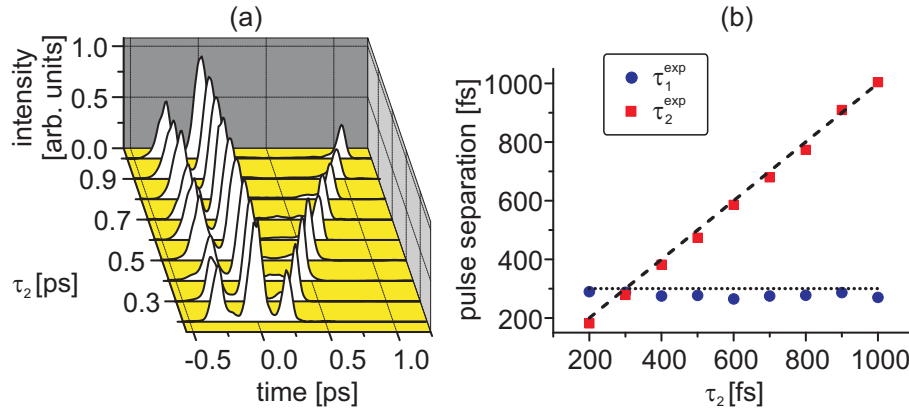


**Figure 2.24:** Measurements of colored triple-pulses tailored through spectral phase function with a variable time separation  $\tau_2$  and constant  $\tau_1 = 300$  fs,  $\delta\omega_1 = -18$  rad/ps, and  $\delta\omega_2 = 31$  rad/ps. (a) The evolution of the temporal intensity of colored triple-pulses tailored with  $\tau_2$ . (b) The experimental pulse separations ( $\tau_1^{\text{exp}}$ ,  $\tau_2^{\text{exp}}$ ) have been determined using a triple ( $\{a_k, b_k, c_k\}$ ) Gaussian fitted-function of the form  $I(t) = \sum_{k=1}^3 a_k \exp(-((t - b_k)^2)/(2c_k^2))$ . The values of  $\tau_1$  (dotted line) and  $\tau_2$  (dashed line) are also depicted for comparison.

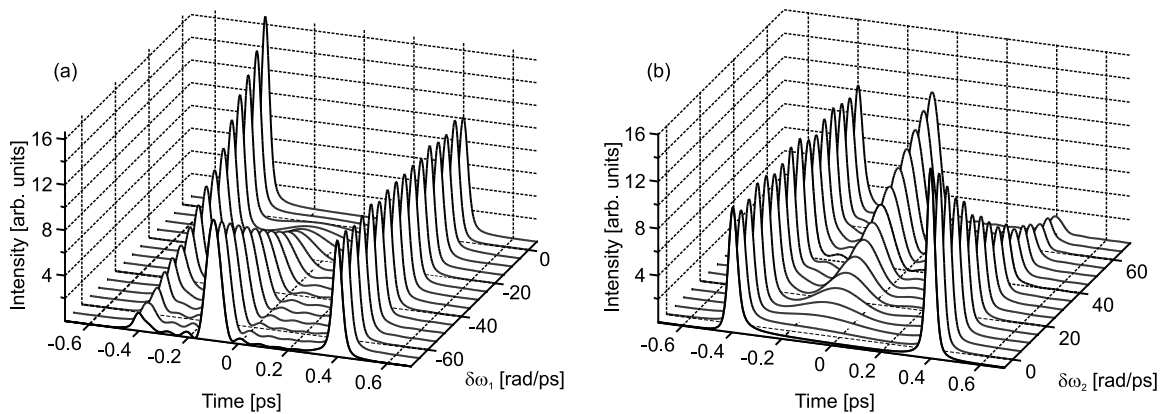


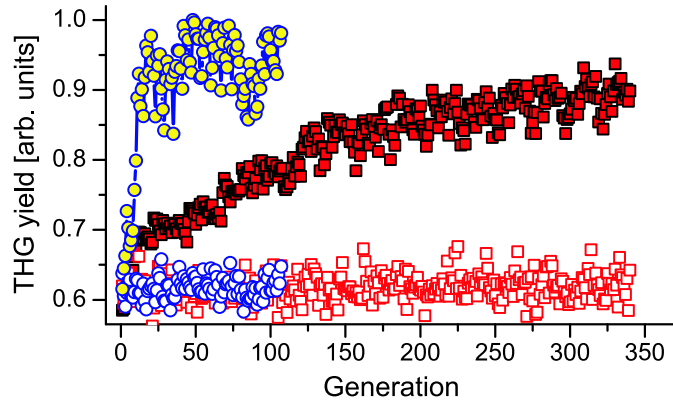
**Figure 2.25:** Simulations of colored triple-pulses tailored through spectral phase functions modifying the relative phase breakpoints ( $\delta\omega_1, \delta\omega_2$ ) only. (a) Modulation of the relative intensity ratio between the first and second pulse by varying the relative phase breakpoint  $\delta\omega_1$  ( $\tau_1 = 300$  fs,  $\tau_2 = 500$  fs,  $\delta\omega_2 = 15$  rad/ps). (b) Similar to (a) but now for the second and third pulse by varying  $\delta\omega_2$  ( $\tau_1 = 300$  fs,  $\tau_2 = 500$  fs, and  $\delta\omega_1 = -15$  rad/ps).

We next tested the capability of the  $C^N$ P-method to independently modulate the relative intensity ratios. The corresponding simulations for  $C^3$ Ps depicted in Fig. 2.25 indicate that the intensity ratios can be controlled via either  $\delta\omega_1$  or  $\delta\omega_2$  without crucially affecting the pulse separations.

The possibility to vary individually delays, and intensity ratios, or, to a certain extent, also chirp of colored pulse trains allows to perform systematical multi-parameter scans of many kinds. For instance, colored triple pulses might be useful for, e.g., pump-dump-probe control of molecular systems [139, 150]. Their applications to clusters within this context are under processing. Further experimental and numerical results for colored quadruple-pulses ( $N = 3$ ) can be found in Publications A.1.2.

In a second example we demonstrate an application of colored pulse trains to closed-

**Figure 2.26:** Evolution of the average of the ten best fitness values after each generation for maximizing the THG yield in the parametric control (yellow-filled circles) and free-optimization (red-filled squares) measurements. Open symbols are their corresponding reference signals of a 400 fs double-pulse measured at the start of each generation.



loop feedback control experiments. For this purpose, the optical setup to generate THG shown in Fig. 2.11 is again employed. The calculated results given in section 2.2.4 serve as the basic references for the following experimental findings. We then phase-only-maximized the third-harmonic yield to find the optimal pulse, using two different approaches: a parametric control experiment (PCE) and a free-optimization experiment (FOE) used as a standard reference. In many respects, these optimization procedures are very similar to the dispersion optimization introduced in section 2.2.2, except for the assignment of fitness values and the encoding methods of the spectral phase functions.

For the PC-experiment, ten different pulse separations and relative phase breakpoints ( $\{\tau_n, \delta\omega_n\}$ ,  $n = [1, 5]$ ) in the range  $[-1 \text{ ps}, 1 \text{ ps}]$  and  $[-150 \text{ rad/ps}, 150 \text{ rad/ps}]$ , respectively, were chosen as the controlled parameters. These encoded the spectral phase function  $\Phi_{\text{MTA}}(\omega)$  according to Eq. (2.28), allowing for the generation and tailoring of clearly structured colored pulse trains ( $\text{C}^6\text{Ps}$ ).

In the free-optimization experiment, the composition of the spectral phase function was based on a set of sixty parameters in total in the range  $[0, 2\pi]$ . These were regularly distributed across the laser spectrum and spline-interpolated at the intermediate frequencies. Upon tailoring, nearly arbitrary spectral phase functions and hence highly complex pulse structures could be generated. To monitor any change in the experimental conditions and to follow the evolution of the optimization search, the best fitness value ( $Y_{\text{PC}}$ ,  $Y_{\text{FO}}$ ) of each generation was compared to a reference value  $Y_{\text{ref}}$  generated by a double-pulse with a pulse separation of 400 fs [101, 102, 136].

The evolution of the averaged fitness values in both strategies is shown in Fig. 2.26. The FOE shows the typical behavior of a many-parameter optimization, i.e., its best fitness value starts to converge after some hundreds of generations. In the present study, the optimization approaches a value of about 0.9 after 350 generations. In contrast, the PCE converges after only a few tens of generations. An optimization factor of  $Y_{\text{PC}}/Y_{\text{ref}} = (1.53 \pm 0.10)$  was achieved for the parametric control experiment, whereas a value of  $Y_{\text{FO}}/Y_{\text{ref}} = (1.45 \pm 0.07)$  obtained for the free-optimization. Probably, the free-optimization experiment will finally give a higher fitness value. However, the devel-

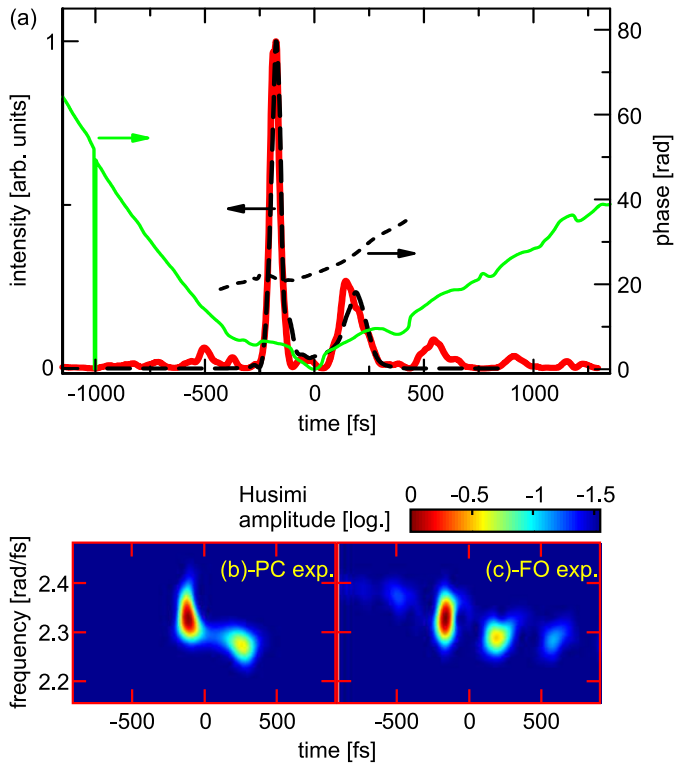


**Figure 2.27:** Top: the temporal phases and intensities of the optimal pulses found in the parametric control (dashed) and free-optimization (solid) experiments. Bottom: the corresponding Husimi representations. Both of the optimized pulses reveal a dominant double-pulse structure with an remarkably stronger leading pulse. The redshift-character of the trailing pulses is also apparent from (b) and (c).

opment of  $Y_{\text{FO}}$  clearly indicates that approaching the optimum will be slow. Obviously, the flexible C<sup>6</sup>P-setup is capable to quickly maximize the signal of this particular task.

To check the extent to which the parametric control pulses can mimic the final result of the free-optimization, both optimal pulses have been characterized in temporal intensity and phase with SHG FROG. This is illustrated in Fig. 2.27 together with the corresponding Husimi distributions. Both pulses show pronounced double-pulse structures with comparable subpulse intensities. However, there are additional weaker subpulses observed in the free-optimization experiment. These subpulses are expected to only give a minor contribution to the third-harmonic generation and might be suppressed at later FO evolutionary steps. The parametric solution instead is already close to the anticipated optimum. We note that our experimental results are in good agreement with the previous CDPFL calculations in section 2.2.4.

The parametric control experiment has a considerable advantage. The method *quickly* uncovers the main pulse characteristics and delivers pulses quite *close* to the optimal solution. This could be taken as a benefit to develop a fast hybrid-coding evolutionary algorithm in which the parametric-optimization solutions serve as seeds for the free-optimization search. In some experiments or simulations, in which the acquirement of fitness values is not directly or time-consuming, the parametric control method as outlined here might be necessary to accelerate the optimization search and therewith allows to successfully perform those studies. First applications to investigation of the strong-field ionization of clusters will be introduced later in section 3.2.2.



# Chapter 3

## Optimal Control of Intense Laser-Cluster Interactions

In this chapter we will briefly describe the experimental and theoretical aspects of clusters in intense laser fields and review the experimental results obtained within the present work. The chapter is organized as follows. We first introduce the helium pick-up cluster apparatus. Then the standard nanoplasma model will be presented, together with some modifications. The influence of the helium matrix on cluster dynamics will be discussed using molecular dynamics approaches. The major experimental results are reviewed in the subsequent sections, concentrating on the optimal strong-field control of the ionization dynamics for He-embedded silver and xenon clusters. Further details can be found in Publications [A.1.3](#) to [A.1.8](#).

### 3.1 Fundamentals of Clusters in Intense Laser Fields

#### 3.1.1 Generation of Cluster Beams

Cluster beams can be prepared by several available techniques described elsewhere [[3](#), [44](#), [151](#), [152](#), [153](#), [154](#)]. In this section we restrict ourselves to describe the generation of clusters in helium nanodroplets using the pick-up technique.

Helium droplet pick-up sources [[47](#), [155](#), [156](#), [157](#)] have proven to be unique at ultralow temperatures. The main body of the He pick-up apparatus used to carry out the experiments was delivered on loan from the Max-Planck-Institut für Strömungsforschung headed by Prof. Toennies and is sketched in Fig. [3.1](#). A detailed description of the machine is given in Refs. [[156](#), [158](#)]. Briefly, helium nanodroplets are produced by supersonic expansion of a precooled helium gas at a stagnation pressure  $P_0$  of 20 bars through a  $5\ \mu\text{m}$ -diameter nozzle. By controlling the temperature  $T_0$  at the orifice (8-16 K), the logarithmic-normal droplet size distributions can be adjusted in between thousands and

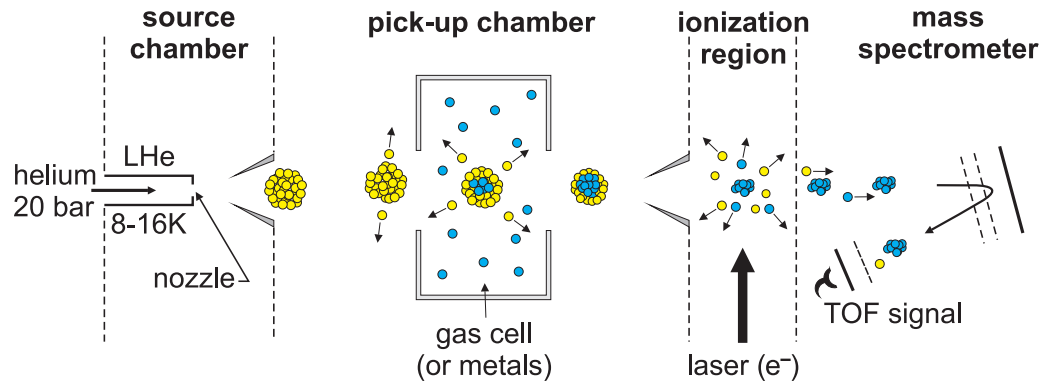


**Figure 3.1:** Experimental setup of a helium droplet pick-up apparatus. See text for more details.

millions atoms (see Fig. 3.2). After passing additional differential pumping stages the droplet beam enters the pick-up chamber containing either a gas cell or a heated oven, where atoms are collected and aggregate to clusters inside the He droplets. With this apparatus it is possible to form clusters with up to  $\sim 150$  silver atoms [159] or 2500 magnesium atoms [160]. Then the beam crosses the interaction zone where the embedded clusters can be ionized with ultrashort laser pulses or high kinetic energy electrons (typically  $\sim 70$  eV). The resulting ionic products are then detected by high resolution reflectron time-of-flight (TOF) mass spectrometry [161, 162].

This type of cluster source shows an outstanding long-term stability, well-suited for performing optimization experiments (see, e.g., our recent paper A.1.5). While in most cases the helium nanomatrix is considered transparent it might become an active part in the interaction process under strong laser fields that substantially changes the cluster dynamics [50, 51, 163]. The discussion about the influence of the surrounding helium medium is given in section 3.1.3.

### 3.1.2 Clusters in Intense Laser Fields

The interactions of clusters with intense laser fields are different from that of atoms or molecules [165]. There are two major reasons: (i) clusters absorb laser energy by a specific mechanism and (ii) depending on the cluster size, the decay of the system will be governed by electron and ion dynamics (collective motions). In other words, many-particle effects including cooperative and collective features characterize the response [166].

For atoms, it is well-known that their response to intense optical laser radiation is determined by multiple ionization processes based on either optical field ionization (OFI) or multi-photon ionization (MPI) (see, e.g., Ref. [44] and Fig. 3.3(a)). For large systems, structural details however become more and more important. For example, ionization barriers can be influenced by the fields from neighboring ions leading to charge-resonance-enhanced ionization (CREI, Fig. 3.3(b)), well-known from strong-field ionization of diatomic molecules [167, 168]. Within this framework, the rate of nonlinear ionization is



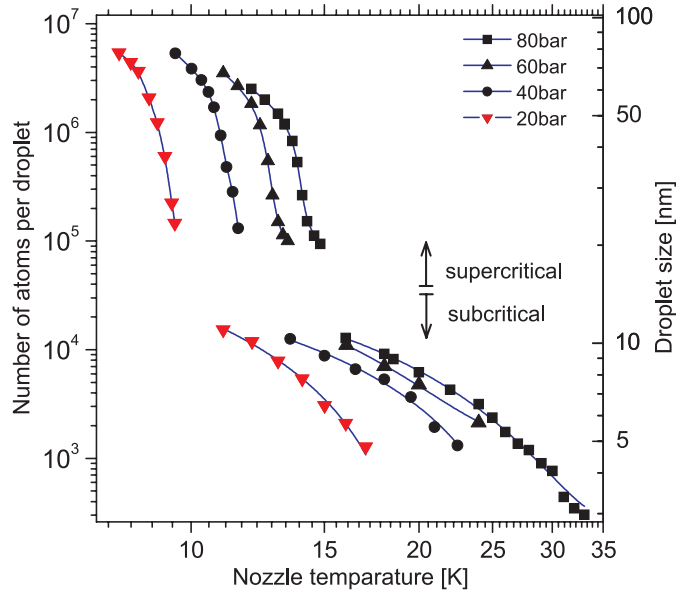


**Figure 3.2:** Mean He droplet size vs. nozzle temperature  $T_0$  for different stagnation pressure  $P_0$ , measured by Toennies and coworkers using beam deflection technique. A  $5\ \mu\text{m}$ -diameter nozzle has been used. The highlighted data points (red) are for the case of interest ( $P_0 = 20\ \text{bar}$ ). Adapted from [164]

strongly enhanced by many orders of magnitude as soon as a molecule is appropriately stretched beyond its equilibrium internuclear separation. CREI has also been applied to small clusters (from a few up to some ten atoms) [169, 170]. We note that due to the presence of many electrons, the total electric field inside the cluster is highly complex, giving rise to an additional stochastic component to charge-enhanced ionization [171].

It is convenient to describe the charging dynamics of clusters by introducing the inner- and outer ionization concept [172] (see Fig. 3.3(c)). Through *inner ionization* tightly bound electrons are removed from their parent ion but still confined within the cluster, giving rise to a number of quasifree electrons. In metallic clusters, electrons are already delocalized. In rare gas clusters, in contrast, electrons have to be first released through the inner ionization. *Outer ionization* then lifts the quasifree electrons into continuum and results in the net charge of the system.

An intuitive picture of rare gas clusters under the influence of strong-field pulses has been proposed by Saalman and coworkers [170, 166], in which the ionization dynamics can be split into three steps as shown in Fig. 3.4: (a) an atomic phase I, (b) a *molecular* or critical expansion phase II, and (c) a relaxation phase III. In phase I, the laser light excites the atoms through OFI or MPI as if they were isolated, the cluster environment is not important here. The quasifree electron production will be initiated during this step (inner ionization). In phase II, the cluster expands due to the Coulomb repulsion resulting in a decreasing ionic density, and hence its plasmon Mie-frequency,  $\omega_{\text{Mie}} \propto \sqrt{\rho_{\text{ion}}(t)}$ , undergoes a redshift. Besides OFI and MPI purely induced by the laser pulse, ionization can be further driven by the *ionization ignition* [173] like, e.g., electron impact ionization (EII)

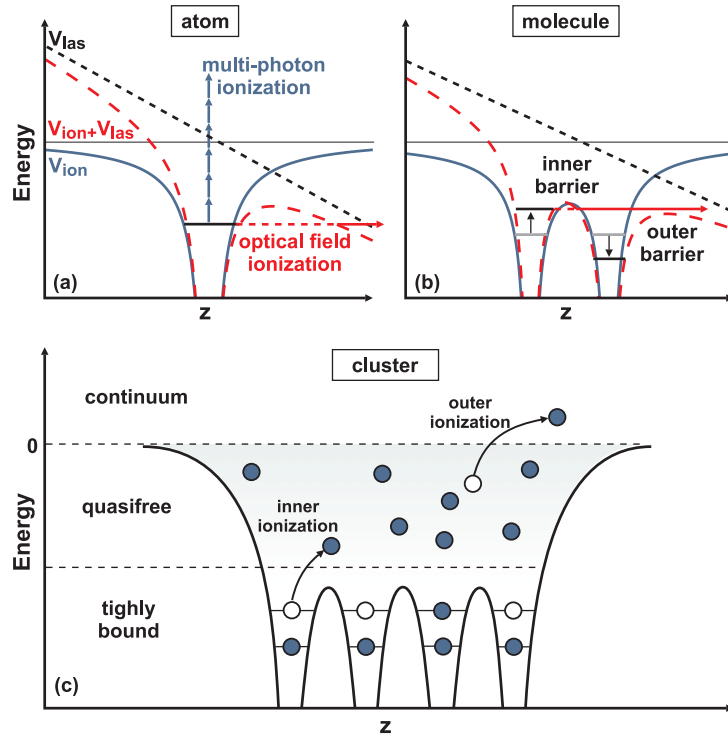


**Figure 3.3:** Schematic view of ionization mechanisms in atoms, molecules, and clusters exposed to intense laser fields. Adapted from [44]

or strong-field amplification. Finally, in phase III the energy transfer to the cluster has come to an end and the redistribution of energy occurs within the cluster through, e.g., recombination resulting in the final charge states.

The quasifree electrons and multi-charged atomic ions in the cluster have been treated as a nanoplasma by Ditmire and coworkers [17], giving a plasma physics based explanation about the efficient energy absorption. Electrons can gain energy from the laser field via inverse bremsstrahlung (IBS), which is replied on the conversion of laser-driven electron motion into thermal energy (laser heating).

### Physics of the Nanoplasma Model

The high density inside clusters (essentially comparable to solids) indicates that collisional ionization can occur, leading to the enhancement of the ionization rate compared to that of low-density atomic gases. The model treats the expanding cluster as a small, spherical plasma, or a *nanoplasma*. In this framework, inverse bremsstrahlung dominates the heating processes in the cluster, giving multi-keV plasma temperatures.

In order for the model to work, a few assumptions are made. First, the clusters have to be large enough (thousands of atoms) so that most of the "ionized" electrons from the host atoms are confined to the cluster during the laser pulse to guarantee quasi-neutrality. Second, the cluster size  $R_c$  must be much larger than the Debye length  $\lambda_D$ , for the plasma picture to be valid. For a solid density of xenon plasma ionized to 5+ with  $T_e \sim 1$  keV, the

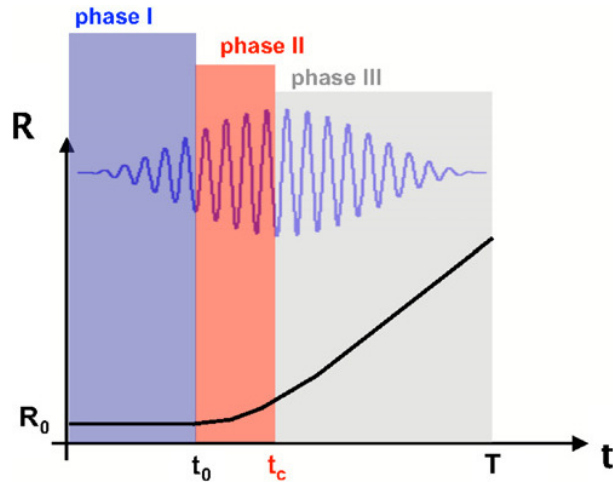


**Figure 3.4:** Simple picture of the three-step ionization dynamics in rare gas clusters subject to an intense laser field in terms of the instantaneous cluster radius  $R(t)$ . Adapted from [166]

Debye length is about 0.8 nm, corresponding to a cluster size of about 40 [165]. Third, the nanoplasma holds together during the laser excitation and hence ultrashort laser pulses are typically required.

**Ionization mechanisms.** There are two major ionization mechanisms which can be important in the interaction of the laser field with atoms of the cluster. The first one is direct optical field ionization of the atoms producing the initial electrons to form the plasma. This ionization rate can be calculated using the ADK formula (Ammosov, Delone and Krainov) [174]. The other mechanism arises from inelastic collisions between electrons and ions, also termed as the *collisional ionization*. Its ionization rate is determined using the collisional ionization rate formula of Lotz [175], taking into account not only the thermal energy of the electrons (thermal collisional ionization) but also their quiver motion in the laser field (laser-driven collisional ionization).

**Heating mechanisms.** Assuming that the laser primarily deposits its energy into the quasifree electrons in the cluster through collisional inverse bremsstrahlung, the heating rate can be found by considering the laser energy deposition rate in a dielectric sphere. The energy deposited per unit volume in the cluster is given by [176]

$$\frac{\partial U}{\partial t} = \frac{1}{4\pi} \mathbf{E} \cdot \frac{\partial \mathbf{D}}{\partial t}. \quad (3.1)$$

The laser field inside the cluster is  $\mathbf{E} = (1/2)\hat{\mathbf{x}}(Ee^{i\omega t} + \text{c.c.})$  and  $\mathbf{D} = \varepsilon\mathbf{E}$ . The heating rate is given by time averaging over a laser cycle,

$$\frac{\partial U}{\partial t} = \frac{\omega}{8\pi} \text{Im}[\varepsilon]|E|^2. \quad (3.2)$$

The total field inside the uniform sphere is [177]

$$E = \frac{3}{|\varepsilon + 2|} E_0, \quad (3.3)$$

where  $E_0$  is the field strength in vacuum. Using the Drude model for the plasma dielectric constant:

$$\varepsilon = 1 - \frac{\omega_p^2}{\omega(\omega + i\nu)}, \quad (3.4)$$

where  $\omega_p = \sqrt{4\pi e^2 n_e / m_e}$  is the plasma frequency and  $\nu$  is the electron-ion collision frequency, the heating rate per unit volume becomes

$$\frac{\partial U}{\partial t} = \frac{9\omega^2 \omega_p^2 \nu}{8\pi} \frac{1}{9\omega^2(\omega^2 + \nu^2) + \omega_p^2(\omega_p^2 - 6\omega^2)} |E_0|^2. \quad (3.5)$$

When the electron density inside the cluster sphere is high compared to the critical electron density, i.e.,  $n_e/n_{\text{crit}} \gg 3$  (with  $n_{\text{crit}} = m_e \omega^2 / 4\pi e^2$ ), then the field inside the cluster, see Eq. (3.3), is smaller than the field surrounding the cluster in vacuum. This shielding results in a decrease of the heating rate because the laser electric field energy density is shielded from the cluster interior. However, when  $n_e/n_{\text{crit}} = 3$ ,  $|\varepsilon + 2|$  goes through a minimum. Consequently,  $E$  and the heating rate are enhanced with respect to the surrounding field. Under these plasmon-enhanced conditions the resonance frequency, also called the Mie- or *surface plasmon frequency*, can be determined as

$$\omega_{\text{Mie}} = \sqrt{\frac{n_e e^2}{3\varepsilon_0 m_e}} = \frac{\omega_p}{\sqrt{3}}. \quad (3.6)$$

The internal field reaches its maximum

$$E_{\text{int}}(\omega = \omega_{\text{Mie}}) = \sqrt{1 + \left(\frac{\omega_{\text{Mie}}}{\nu}\right)^2} E_{\text{ext}}. \quad (3.7)$$

The relative height and width of this resonance are determined by the value of the collision frequency  $\nu$ . In addition, in isolated clusters, there is no heat conduction to an environment, indicating that high plasma temperatures can be expected. For metal clusters, the Mie-frequency is substantially higher (e.g., about 4 eV for small silver clusters  $\text{Ag}_N$  [178]) compared to the laser frequency of about 1.54 eV (800 nm). Therefore, cluster expansion that decreases the Mie-frequency is necessary to achieve a resonant coupling of laser energy.

**Expansion mechanisms.** There are two forces which contribute to the expansion of the cluster during and after the laser pulse: (i) the pressure associated with the hot

electrons which stream outwards and drag the ions with them, and (ii) the Coulomb forces from a charge-buildup on the cluster. By ignoring the pressure of the cold ions, the total pressure  $P$  can be broken down into a hydrodynamic term from the hot electrons and a Coulomb term:  $P = P_e + P_{\text{Coul}}$ . The equation for the time-dependent radius of the cluster becomes

$$\frac{\partial^2 r}{\partial t^2} = 5 \frac{P_e + P_{\text{Coul}}}{n_i m_i} \frac{1}{r}. \quad (3.8)$$

The hydrodynamic pressure is taken as the ideal electron Fermi gas pressure,  $P_e = n_e k T_e \propto 1/r^3$ , and the Coulomb pressure contribution is due to a charge-buildup,  $P_{\text{Coul}} = Q^2 e^2 / 8\pi r^4$ . From the  $(1/r^4)$  scaling, we see that the Coulomb force becomes most dominant for small clusters. Cluster expansion is important since it leads to the rapid decrease in  $n_e$  required for the resonant heating condition (Eq. (3.6)) occurring near the peak of the laser pulse.

**Modifications.** The original nanoplasma model [17] has made significant contributions to predictions and verifications of the experimental results on intense laser-cluster interactions. These include the production of energetic electrons [5] and ions [6], soft X-ray and EUV emission [7], and extreme highly charged ions [6]. It also indicates that the resonant heating accounts for the efficient absorption of laser energy when the electron density drops down to  $3n_{\text{crit}}$ . The existence of an optimum cluster size for a given laser pulse [19] and an optimum pulse duration [23, 24, 25, 26, 27] or dual-pulse delay [30, 31] for a given cluster size also supports the validity of the model.

The model, however, makes use of the collision frequency in the classical theory of Silin [179], which is not applicable at high densities. Therefore, further modifications have been considered in recent work, including (i) the collisions of electrons not only with individual ions but also with the surface of the cluster [180, 181, 182], and (ii) the lowering of the ionization energies due to screening [49, 183].

The modified version gives a more complete description of the collisional processes. In particular, high-order ionization processes involving valence electrons have been introduced to improve the production of high charge states, and the dynamics of inner-shell electrons has been partially included to reproduce the  $K_\alpha$  X-ray emission [181]. The picture looks like follows. The laser field first ionizes cluster atoms mainly through tunnel ionization. Once free, these electrons will further ionize atoms/ions through collisions. Due to the high excitations and densities reached inside the cluster, the collisional process is found to be important and produces much higher charge states than the optical ionization alone. This modified model has been used to explain the experimental findings on silver clusters (see Publications A.1.5).

### 3.1.3 Dynamics of Clusters in Helium Nanodroplets

When embedded into an environment or deposited at surfaces, clusters typically change their optical responses upon external excitations (see, e.g., [184]). A detailed discussion concerning this issue is given recently by Fennel and coworkers [44, 185]. Here we concentrate on the influence of surrounding environments, especially the He nanomatrix, on the embedded clusters in intense laser fields.

In the strong-field regime, composite clusters are proven to be more efficient in energy absorption compared to the corresponding homonuclear clusters. It has been demonstrated that by irradiating heteronuclear clusters  $(\text{D}_2\text{O})_N$  with intense ( $I_L > 10^{16} \text{ W cm}^{-2}$ ) fs laser pulses [186, 187], the resulting high-energy ( $> 3 \text{ keV}$ ) particles can be used to drive nuclear fusion. In other approaches, an increase of the highest charge states [188, 189] and an enhancement of the yield of X-rays [21, 190] have been obtained for rare gas clusters (Kr or Ar) doped with easily ionizable molecules (HI or  $\text{H}_2\text{O}$ ). The basic physics behind is as follows. The ease of ionizing molecules increases the number of quasifree electrons released in the initial stages of the laser pulse [191], resulting in an enhanced contribution to the subsequent electron impact ionization and thereby the yields of ionized products.

Within this context, interest in the impact of the surrounding helium nanomatrices on ionization dynamics in clusters has been triggered by an earlier work in our group [192]. Recent pump-probe molecular dynamics simulations [50, 51] on free and He-embedded xenon clusters ( $\text{Xe}_{100}\text{He}_N$  with  $N$  of up to 5000) have identified the presence of two plasma resonances due to the He shell and the xenon core. In addition, an early and efficient energy absorption was observed for embedded clusters resulting from the He shell, which explodes faster than the xenon core and dominates the absorption properties of the composite cluster.

Employing an MD approach to a similar system ( $\text{Xe}_{309}\text{He}_{10000}$ ) under an intense pump-probe laser scheme, Peltz and Fennel [193] have studied the impact of double plasmon resonances on the charging process. By resolving the energy absorption spatially, they are able to capture both the final Xe charge and electron energy spectra as shown in Fig. 3.5.

Through the presence of the He surrounding, a significant increase in the maximum charge states (through, e.g., shell-induced inner ionization enhancement) was obtained (cf. Fig. 3.5(a) and (d)). The time-dependent dynamics of the Xe ion spectra is quite similar for pure and embedded systems and therefore no double resonance for ions could have been observed (Fig. 3.5(d)). This result might serve as an explanation for the absence of multiple plasmon resonances in the experimental data published so far (see, e.g., Refs [30, 116, 163]). On the contrary, the calculated electron energy spectra as function of delay clearly show a double-peak feature, which is strongly related to the efficient energy absorption in the He shell and the Xe core (Fig. 3.5(e) and (f)). This numerical work suggests that a simultaneous analysis of the ion and electron spectra gives a possible

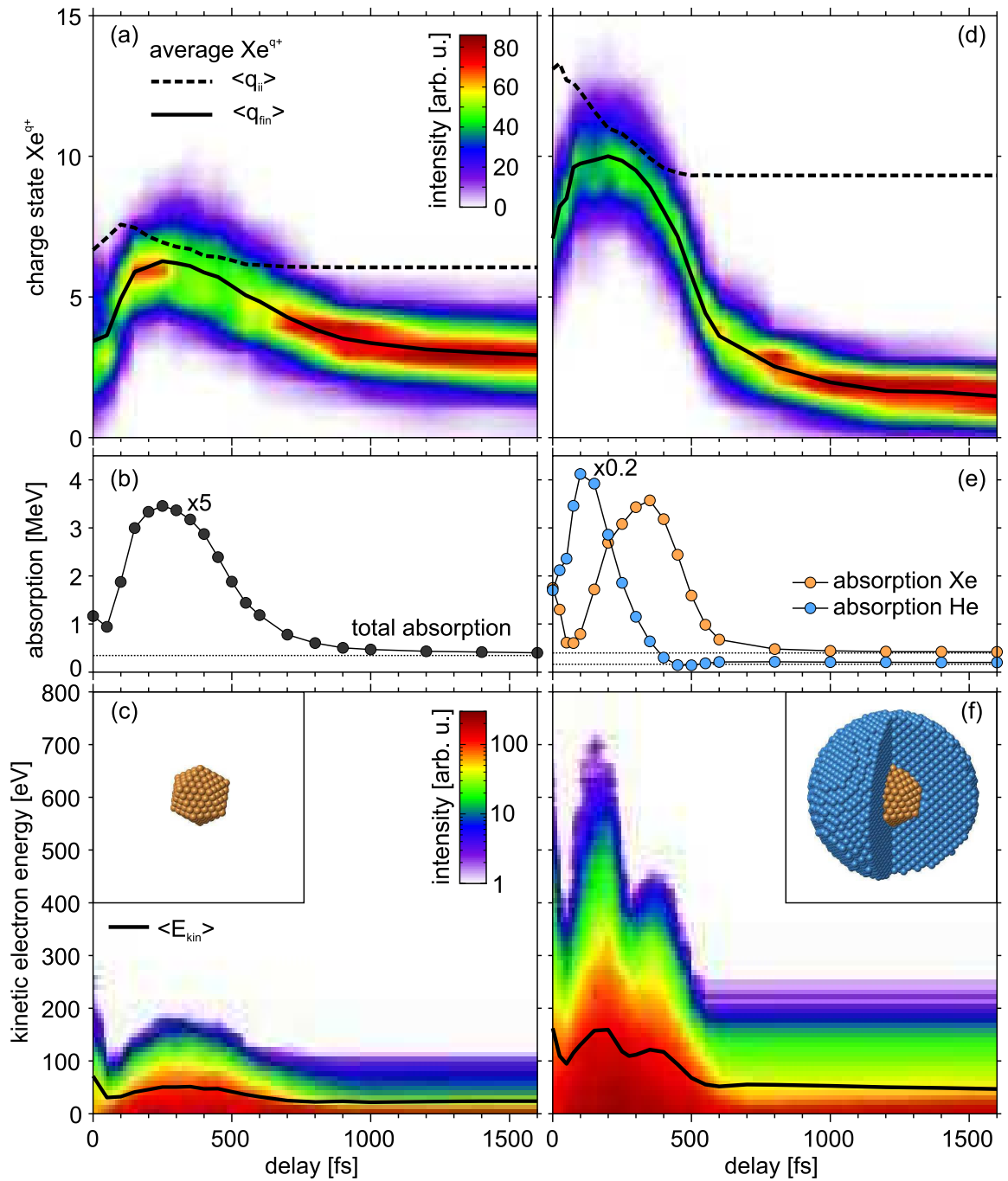


**Figure 3.5:** Delay-dependent final Xe ion spectra (top), energy absorption (middle) and electron energy spectra (bottom) for pure  $Xe_{309}$  (left column) and  $Xe_{309}He_{10000}$  (right column) exposed to double pulses of variable delay (intensity  $I_0 = 2.5 \times 10^{14} \text{ W cm}^{-2}$  and duration  $\tau_p = 25 \text{ fs}$ ).  $\langle q_{ii} \rangle$  and  $\langle q_{fin} \rangle$ : average values of inner ionization and final charge states, respectively.  $\langle E_{kin} \rangle$ : the average kinetic energy of emitted electrons. Insets: corresponding initial geometry of the investigated clusters. See text for further description. From Peltz and Fennel [193]

way to identify the presence and temporal structure of multiple resonances in embedded clusters.

## 3.2 Reviewed Data on the Control of Intense Laser-Cluster Interactions

### 3.2.1 Silver Clusters

**Earlier Open-Loop Measurements.** Similar to rare gas clusters (chapter 1), metal clusters have also shown strong laser energy absorption, which subsequently leads to, e.g., the production of extreme highly charged ions [194] or ionic recoil energies as high as 180 keV [195]. This has been accounted for the plasmon-enhanced resonant ionization mechanism as mentioned earlier. According to the model, the delocalized electrons already present in the ground state of the metal cluster exhibit a collective oscillation mode (plasmon) with the Mie-frequency,  $\omega_{\text{Mie}} \propto \sqrt{\rho_{\text{ion}}}$  (see Eq. (3.6)). Usually the corresponding plasmon energies of metal clusters are substantially higher than the Ti:Sapphire laser photon energy ( $\sim 1.54$  eV). Therefore, to achieve a resonant excitation the cluster density has to be decreased through, e.g., expansions. This indicates the possibility to control the charging of clusters by tailoring the temporal laser pulse shapes.

Extensive effort has been made to achieve a control over the ionized products such as electrons or ions. By changing the pulse width from 140 to 600 fs, Köller *et al.* [24] have observed an increase in the highest observed ionic charge state  $q^*$  from exploding platinum clusters up to  $q^* = 20$ . Note that for platinum atoms under the similar laser conditions, only charge states as high as  $q^* = 4$  have been obtained.

In another study, Döppner *et al.* [30] have investigated the ultrafast dynamics of silver clusters exposed to fs dual-pulses of variable delay. For each charge state, an optimum delay has been found which results in the maximum ion yield, allowing to selectively control the charging process. This also confirms the presence of the collective dipolar electron motion within the cluster: The first laser pulse provides the initial ionization through nonresonant effects such as tunnelling or optical field ionization, which triggers the cluster expansion, leading to a redshift of the transient Mie frequency. If the second pulse arrives after a certain optical delay, the Mie-frequency could match the excited laser frequency resulting in an effective charging of the cluster. The corresponding Vlasov dynamics simulations have indicated that these *initial* and *resonant* ionization steps can be treated separately. While the first pulse intensity determines the optimum time delay, the second defines the magnitude of the final ionization signal.

Further observation of a plasmon-enhanced ionization has been made by Fennel *et al.* [31] using a dual-pulse scheme on medium-sized clusters. By rotating the polarization



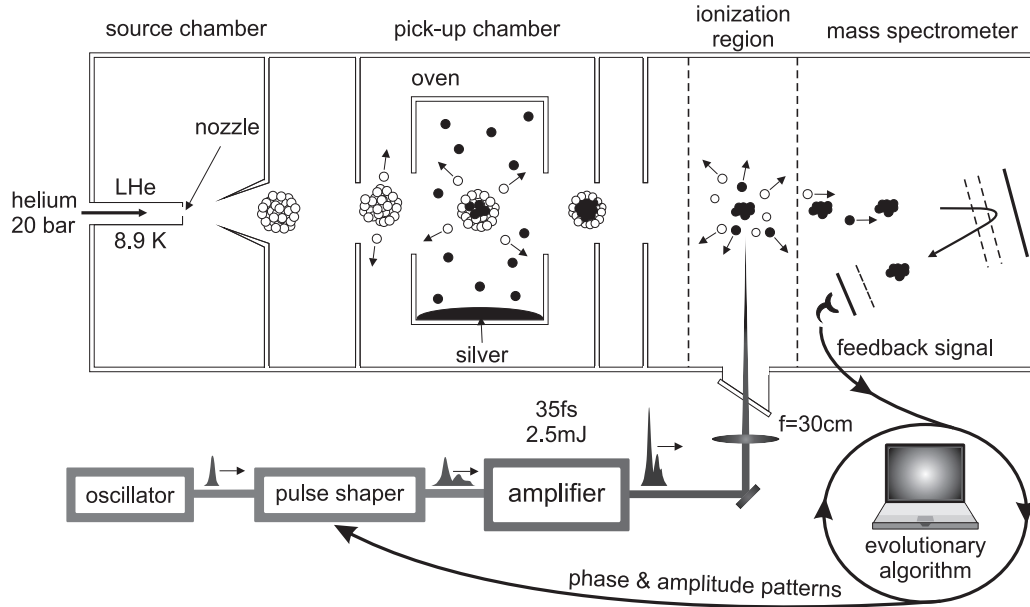


**Figure 3.6:** Schematic view of the experiment for closed-loop optimization of the highly charged atomic Ag ions. *Top:* (i) the generation of the helium nanodroplets, (ii) the formation of the silver clusters inside the droplets by sequential atomic pick-up in the oven, (iii) the laser excitation in the interaction region, and (iv) the time-of-flight analysis in the reflectron time-of-flight mass spectrometer (from left to right). *Bottom:* The stages of pulse delivery from seed pulse generation in the oscillator, to pulse modification in the pulse shaper and final amplification, to pulse focusing into the molecular beam apparatus. In the optimal control experiment, the yield of highly charged ions is maximized by applying an evolutionary algorithm scheme within a feedback loop.

of the second pulse, an enhanced electron emission along the laser polarization axis has been demonstrated.

**Closed-Loop Measurements.** Stretched or dual-pulse techniques mentioned so far allow a simple control over the production of charge-state selected ions or energetic electrons, for instance. This might be interesting for the generation of efficient light sources at desired wavelengths (e.g., EUV). Nowadays, advances in femtosecond pulse shaping (see, e.g., Refs. [40,68] and references therein) make it possible to simultaneously modulate the phase, amplitude, and even polarization state of ultrashort laser pulses. These permit to perform experiments with arbitrarily complex pulse shapes. Moreover, closed-loop optimization experiments can be realized in combination with a computer self-learning algorithm [41].

While widely applied in coherent quantum control (see, e.g., Refs. [69,72,107]) for a long time, the closed-loop feedback control scheme has recently been adapted to study rare gas clusters in a few experiments. The first optimal control experiment on clusters in strong laser fields was conducted by Zamith *et al.* [42], who used a phase-only pulse shaper to maximize the abundance of highly charged Xe ions. The optimized light field contains a two-pulse sequence with comparable intensities and produces ions up to  $\text{Xe}^{23+}$ . In a similar approach, but applying to the topic of X-ray emission rather than the ion yield,

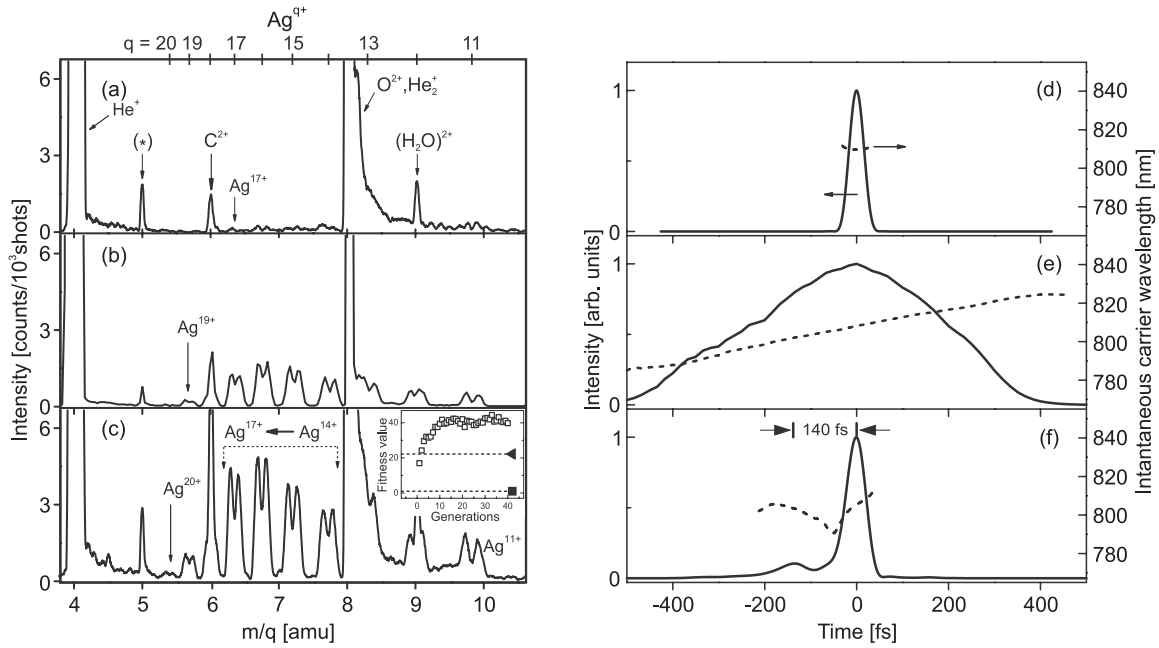


**Figure 3.7:** TOF-mass spectra (left) with highly charged atomic ions obtained when exposing embedded silver clusters to different intense laser pulses (right): (d) a 50 fs pulse ( $I_L = 1 \times 10^{16} \text{ W cm}^{-2}$ ), (e) a 500 fs linearly downchirped pulse, (f) the optimized pulse. Inset: evolution of the averaged best fitness value (open squares) in the optimization experiment, compared to the reference measurements (50 fs, solid square; 500 fs pulses, solid triangle). See text for detail.

Moore *et al.* [20] found that a double-pulse (delay  $\sim 100$  fs) can efficiently heat clusters to maximize the X-ray emission. In both experiments, the spectral phase of the optimized laser fields was however not analyzed in detail.

In our closed-loop adaptive approach (see Publications A.1.5), we maximized the yield of the highly charged ions  $\text{Ag}^{q+}$  (with  $q = 14 - 17$ ) by use of the AOPDF (section 2.2.1) combined with the evolutionary algorithm (section 2.1.2). Both phase and amplitude modulation have been employed. Figure 3.7 shows the TOF-mass spectra (left, (a)–(c)) obtained by exposing the embedded clusters to different pulse shapes (right): (d) a 50 fs pulse, (e) a 500 fs linearly downchirped pulse, and (f) the adaptively obtained optimal pulse, respectively. The main findings are as follows. (i) The adaptively determined pulse has a remarkably simple double-pulse structure, containing a low-intensity prepulse and a stronger main pulse, see Fig. 3.7(f). This again confirms the plasmon-model and emphasizes the separate roles of the pre- and postpulse in ionization processes. While only a small prepulse is sufficient to initiate the cluster expansion, most of the laser energy should concentrate on the postpulse to efficiently produce the highly charged ions. To the best of our knowledge, this unique feature is observed for the first time for metal clusters. It turns out to be opposite to the findings in xenon clusters as shown later. (ii) A negative chirp (redshift) during the main pulse hints at dynamic frequency locking to the transient cluster plasmon (Fig. 3.7(f), dashed line). And (iii) an enhancement of the highest atomic charge states up to  $q = 20$  has been achieved.

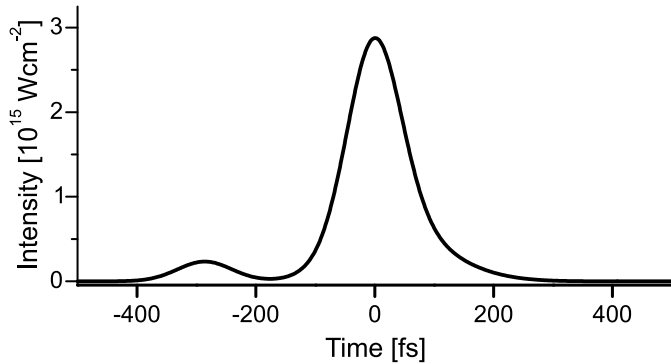


**Figure 3.8:** Calculated temporal intensity evolution of the optimal light field for producing a maximum yield of  $\text{Ag}^{10+}$ . The intensity envelope is in qualitative accordance with the experimental result, (cf. Fig. 3.7(f)). The total pulse fluence corresponds to a 35-fs pulse with a peak intensity  $1 \times 10^{16} \text{ W cm}^{-2}$ .

To assist the experimental study, we<sup>1</sup> have developed a theoretical approach to find the laser pulse shapes that maximize the total yield of a particular highly charged ion in the laser-cluster interaction. For this aim, a genetic algorithm is employed and adapted to the modified nanoplasma approach [49] (see also section 3.1.2), with restriction to the number of possible pulse shapes of the form:

$$I(t) = \sum_{n=0}^4 A_n \exp \left[ -\frac{4 \ln 2 (t - t_n)^2}{\sigma_n^2} \right]. \quad (3.9)$$

Here  $A_n$ ,  $t_n$ , and  $\sigma_n$  are the weights, time offsets, and temporal widths, respectively. While the laser parameters are similar to experiments (central wavelength 810 nm, peak intensity  $1 \times 10^{16} \text{ W cm}^{-2}$ , and duration of 35 fs), the silver clusters are quite large (4500 atoms), compared to experiments ( $\sim 150$  atoms), to ensure the validity of the nanoplasma model.

The calculated optimal pulse shape leading to the maximum yield of  $\text{Ag}^{10+}$  is shown in Fig. 3.8, which delivers the significant features, e.g., the double-pulse structure and the relative intensity ratio, close to the experimental solution. The time delay of the calculated optimal pulse turns out to be longer when compared to the experiment, which might be due to the larger size of the simulated system. Further details can be found in our recent work (Publications A.1.3 and A.1.5).

Similarly, we can also perform the closed-loop optimization with feedback values given as the signals of selected charge-state ions. Figure 3.9 displays the TOF spectra, which originate from laser pulses obtained by maximizing the yield of different highly charged ions  $\text{Ag}^{q+}$ . Interestingly, the ion charge state distributions peak around the selected  $q$  whose yield has been maximized. Consequently, by excitation with shaped pulses, controlled sources of intense energetic particles (ions or electrons) might be constructed.

**Dual-Pulse Approach with Nonlinear Pulse Shaping.** As briefly mentioned in section 2.2.3, amplitude-and-phase shapers can create dual-pulses with variable time

<sup>1</sup>In collaboration within the SFB 652 with P. Hilde, Th. Bornath, M. Schlanges (project A6), and Th. Fennel (project A8).

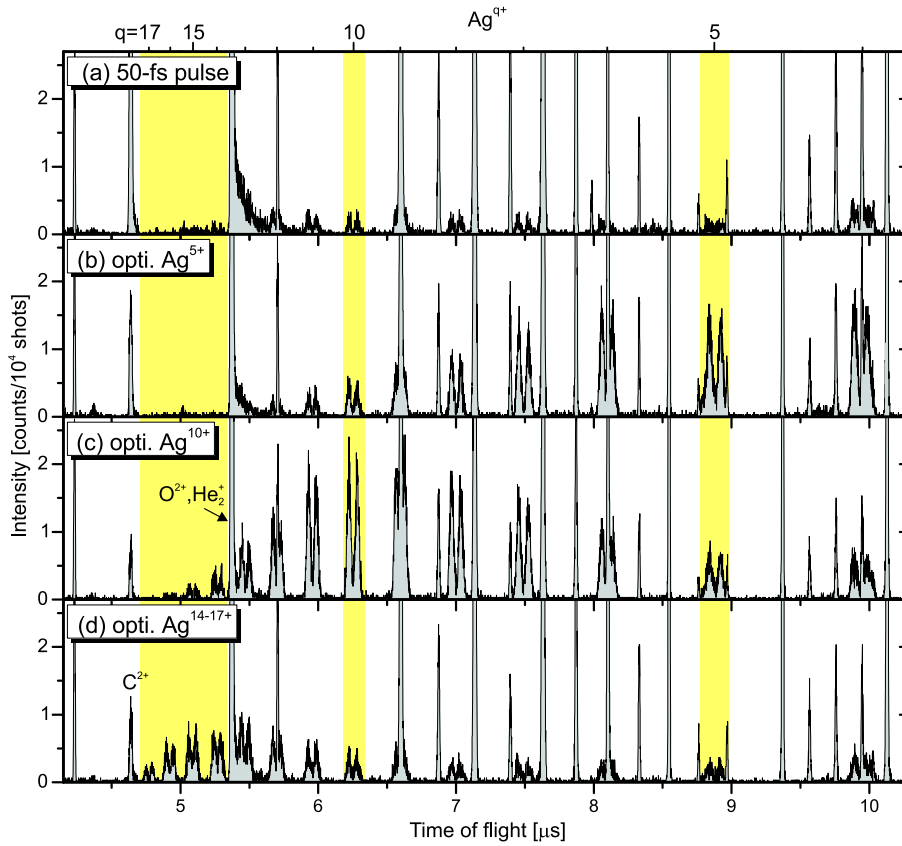


**Figure 3.9:** Ion TOF spectra originating from shaped laser pulses, which give maximal yield of different selected highly charged ions (as indicated). The case (a) is shown for comparison, where single 50 fs pulses were used ( $I_L = 5 \times 10^{15} \text{ W cm}^{-2}$ ).

delay and amplitude. It is therefore possible to perform shaper-assisted dual-pulse experiments on clusters with a single laser beam. If a dual-pulse is generated with a pulse shaper prior to the CPA amplifier, the respective amplified pulse will be a pulse train, consisting of an intense dual-pulse accompanied by several small satellite pulses equally spaced on both sides. This is due to the nonlinear distortions in the CPA, as pointed out in Publications A.1.1 and by others [196, 197, 198]. Under certain circumstances, these satellites, if intense enough, might contribute significantly to the ionization processes, and thus result in an ambiguity in optical delays.

As an illustration, we show in Fig. 3.10 the ionic signals of  $\text{Ag}^{5+}$  and  $\text{Ag}^{19+}$  vs. optical delay  $\Delta t$ , obtained from a shaper-assisted dual-pulse experiment on silver clusters. The initial laser and cluster conditions are similar to the closed-loop optimization experiment above. For simplicity, only  $\Delta t < 0$  needs to be considered. For  $\text{Ag}^{5+}$ , a clear double-peak feature is observed, while for  $\text{Ag}^{19+}$  only a single peak is visible. There is actually no clear explanation for this observation so far. One of the reasons might be due to the complex nonlinear behaviors of the additional satellites in the CPA. In particular, their intensities change with the dual-pulse delay (see Publications A.1.1). Possibly, for certain small optical delays, the satellites are sufficiently intense to take part in the charging process,

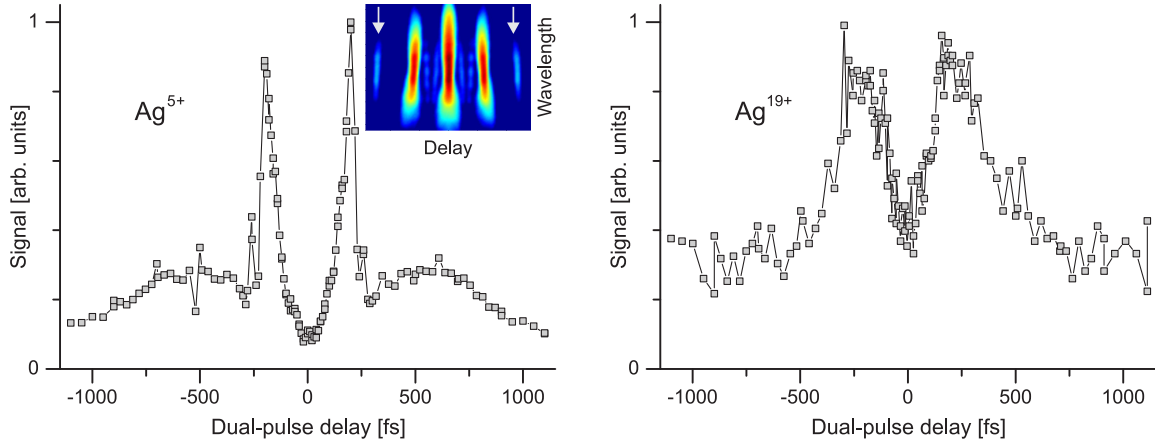


**Figure 3.10:** Amplified dual-pulse yields of  $\text{Ag}^{5+}$  (left) and  $\text{Ag}^{19+}$  (right) as function of optical delay. Inset: Experimental SHG FROG trace of an amplified dual-pulse ( $\Delta t = 600$  fs), showing the unexpected satellites (marked by arrows) formed due to nonlinear distortions in the CPA. See text for further details.

resulting in the (multi)-peak feature in the dual-pulse curves. In addition, the helium environment might also have some impact, which gives rise to the significant yield at the time delay  $\sim \pm 200$  fs (see Fig. 3.10, left). Nevertheless, this nonlinear shaping scheme can be employed to enhance the yield of different selected charge states.

Further study is necessary to get more insights into this issue, for instance using triple-pulses of variable delays constructed with Mach-Zehnder interferometers. Another alternative is to use colored multipulses as introduced to investigate xenon clusters below.

### 3.2.2 Studies of Xenon Clusters exposed to Intense Colored Multipulses

In the following we present the experimental results on the study of embedded xenon clusters using the colored double pulse fitness landscape technique and a restricted closed-loop feedback control scheme. The experimental setups are similar to in Fig. 3.6. In brief, He-embedded xenon clusters  $\text{Xe}_N$  with a mean size  $\bar{N}$  of about 300 atoms are in use. For excitation, tailored laser pulses with different input energies of 0.5 mJ, 1.0 mJ, and 1.9 mJ are focused with a 25 cm lens, giving initial intensities<sup>2</sup> of  $2.8 \times 10^{15} \text{ W cm}^{-2}$ ,  $5.5 \times 10^{15} \text{ W cm}^{-2}$ , and  $1.0 \times 10^{16} \text{ W cm}^{-2}$ , respectively. The absolute intensity values in the interaction chamber are calibrated by studying the generation of  $\text{Xe}^{q+}$  with up to  $q = 6$  in atomic xenon [199].

#### Colored double pulse fitness landscape studies

At laser pulse intensities above  $10^{14} \text{ W cm}^{-2}$ , the embedded clusters completely disintegrate and Xe ions of different charge states are created. A charge state spectrum for

<sup>2</sup>At  $\tau = 0.0$  fs (single pulse conditions,  $\tau_p \simeq 50$  fs)

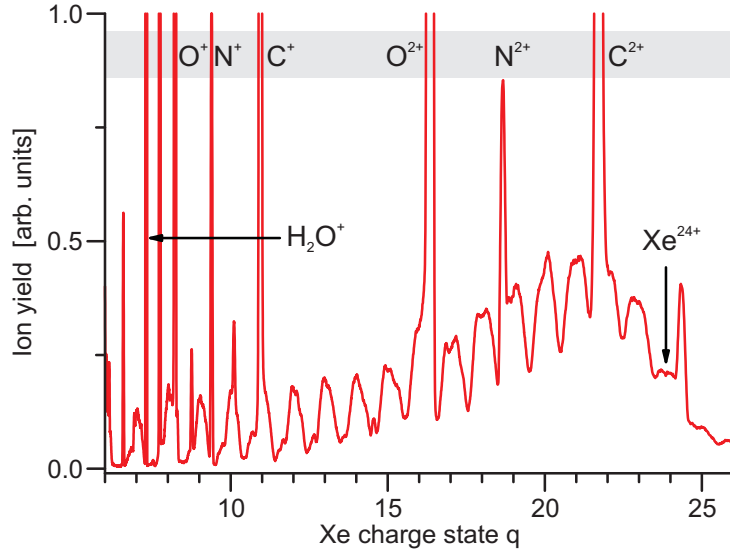


**Figure 3.11:** Typical charge state spectrum obtained from xenon clusters  $\text{Xe}_N$  ( $\bar{N} = 200$ ) in helium droplets exposed to stretched 500 fs laser pulses at  $2 \times 10^{15} \text{ W cm}^{-2}$ . High charge states up to  $q = 24$  are observed. In addition to  $\text{Xe}^{q+}$ , signals from residual gas molecules (e.g.,  $\text{O}^{2+}$ ,  $\text{C}^{2+}$ ,  $\text{H}_2\text{O}^+$ ) are also recorded.

500 fs-FWHM chirped pulse excitation is depicted in Fig. 3.11, showing intensity up to  $q = 24$ . Notably, the yield  $Y(\text{Xe}^{q+})$  is enhanced for  $q > 15$ . We note however that, similar to the case of  $\text{Ag}_N$ , different ionic distributions can be formed by tuning the pulse width or the dual-pulse delay (as shown later). In a CDPFL measurement, such spectra are recorded as a function of spectral phase breakpoint  $\lambda_{\text{br}}$  and double pulse separation  $\tau$  taking the yields of  $\text{Xe}^{q+}$  as fitness values.

**Pump-Probe Characteristics.** For each spectral phase breakpoint  $\lambda_{\text{br}}$ , pump-probe ( $\mathcal{PP}$ ) like measurement can be obtained by recording TOF spectra as a function of the pulse separation  $\tau$ . As an illustration, Fig. 3.12 displays the  $\mathcal{PP}$  characteristics of  $\text{Xe}^{17+}$  for specific spectral phase breakpoints (relative intensity ratios) with an input energy  $E_L = 0.5 \text{ mJ}$ . At  $\lambda_{\text{br}} = 827 \text{ nm}$  ( $I_{\text{CDP}}^{(\tau < 0)} \simeq 286.0$ , Fig. 3.12(a)), one of the subpulses has an intensity well below  $10^{13} \text{ W cm}^{-2}$ , which obviously is not sufficient to induce the effective generation of  $q = 17$ . Therefore, the  $\mathcal{PP}$ -signal of  $\text{Xe}^{17+}$  shows no evidence of a time delay-dependent dynamics. This confirms the previous findings that single-pulse excitation is quite inefficient for clusters [30, 111]. At a higher ratio  $I_{\text{CDP}}^{(\tau < 0)} \simeq 20.6$  (Fig. 3.12(b)), evidence of resonant charging shows up only at a certain *negative* value  $\tau_{\text{max}}^\lambda < 0.0 \text{ fs}$ . This first indicates that two separate pulses are required to efficiently generate  $\text{Xe}^{17+}$ . Second, as described earlier, this  $(\lambda_{\text{br}}, \tau)$ -setting corresponds to colored double pulses with a strong blue-detuned leading pulse and a weaker red-detuned trailing pulse for  $\tau < 0$ , and vice versa for  $\tau > 0$ . It shows that a stronger leading pulse is more favorable for an effective charging, rather than a weak one as for silver clusters shown in section 3.2.1. Higher leading pulse intensity is necessary for a resonant charging to occur, as seen in Fig. 3.12(c)

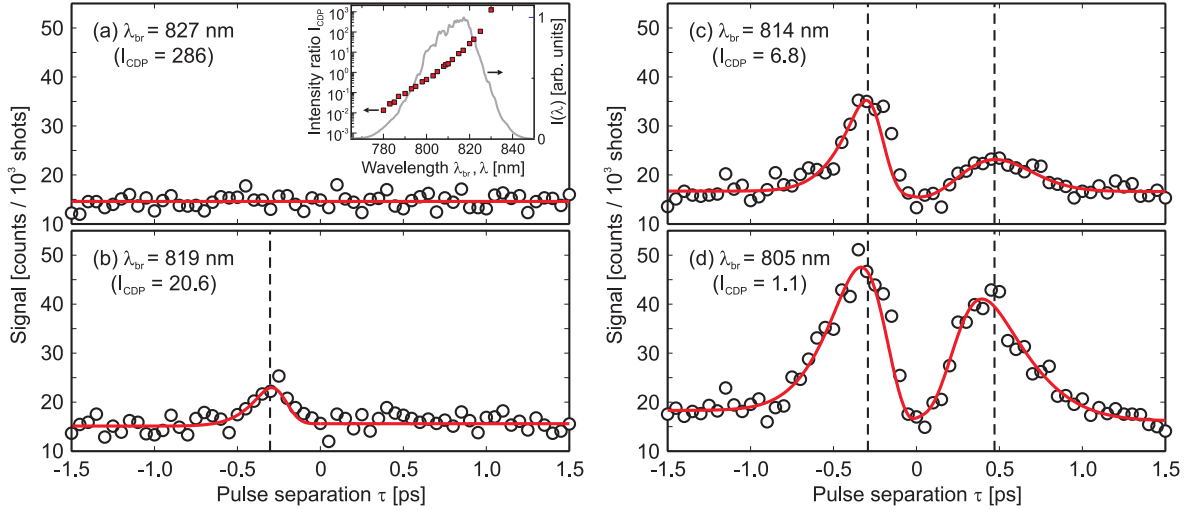


**Figure 3.12:** Colored double pulse yields of  $\text{Xe}^{17+}$  (circles) as function of pulse separation  $\tau$  at selected phase breakpoints  $\lambda_{\text{br}}$ , showing the onset of multiple ionization of embedded Xe clusters. The corresponding pulse intensity ratios  $I_{\text{CDP}}$  (for  $\tau < 0$ ) are also indicated. Combined exponential functions are applied separately to negative and positive  $\tau$  to fit the experimental data (lines). The maximum values will serve as inputs to deduce the charge state-selective appearance intensity thresholds shown in Fig. 3.19. The vertical dashed lines mark the peak positions in (b) to show the slight shifts of  $\tau_{\text{max}}^{\lambda}$  with intensity of the corresponding leading pulses. Inset: Relative intensity ratio  $I_{\text{CDP}}^{(\tau < 0)}$  vs. spectral breakpoint wavelength (squares) and the laser spectrum (gray line) for comparison. In this example, an input energy  $E_L = 0.5$  mJ was in use, giving an initial intensity of  $2.8 \times 10^{15}$   $\text{Wcm}^{-2}$ .

for  $\tau > 0$ . Finally, for  $I_{\text{CDP}}$  near unity (Fig. 3.12(d)), a clear double peak structure can be obtained with an enhancement of  $\sim 20\%$  for  $\tau < 0$ . This particular feature will be discussed in detail below, with respect to the global chirp of colored double pulses. Additionally, a small shift of the optimum time delay  $\tau_{\text{max}}^{\lambda}$  towards smaller values with an increasing intensity of the leading pulse is observed, in good agreement with previous findings for silver clusters using the  $\mathcal{PP}$ -approach [30]. We also note here that by analyzing the yield of the ions at optimum delays, the charge state-selective threshold intensity can be deduced (see below).

**Overview of the CDP landscapes.** A full fitness landscape can be obtained by scanning both the  $(\lambda_{\text{br}}, \tau)$  parameters with certain resolutions and is shown in Fig. 3.13(a) for  $\text{Xe}^{17+}$  as an example. The double peak features in the previous  $\mathcal{PP}$  spectra in Fig. 3.12 now show up as a double-hill in the landscape. The lower figures are the corresponding  $(I_{\text{CDP}}, \tau)$ -landscapes extracted from the upper one for negative (Fig. 3.13(b)) and positive (Fig. 3.13(c)) values of  $\tau$ . Generally, both the hills have a quite similar shape in terms of the relative intensity ratio  $I_{\text{CDP}}$ , reflecting the response the clusters to intensities of the subpulses. The roughly sketched dashed lines are to guide the eyes, showing the shift of  $\tau_{\text{max}}^{\lambda}$  towards smaller values with increasing intensity of the leading pulses. We note however two major differences of the  $(I_{\text{CDP}}, \tau)$ -landscapes. First, for a given  $I_{\text{CDP}}$ , the respective  $|\tau_{\text{max}}^{\lambda}|$  value is smaller for negative rather than positive  $\tau$ . This implies that a *blue-*

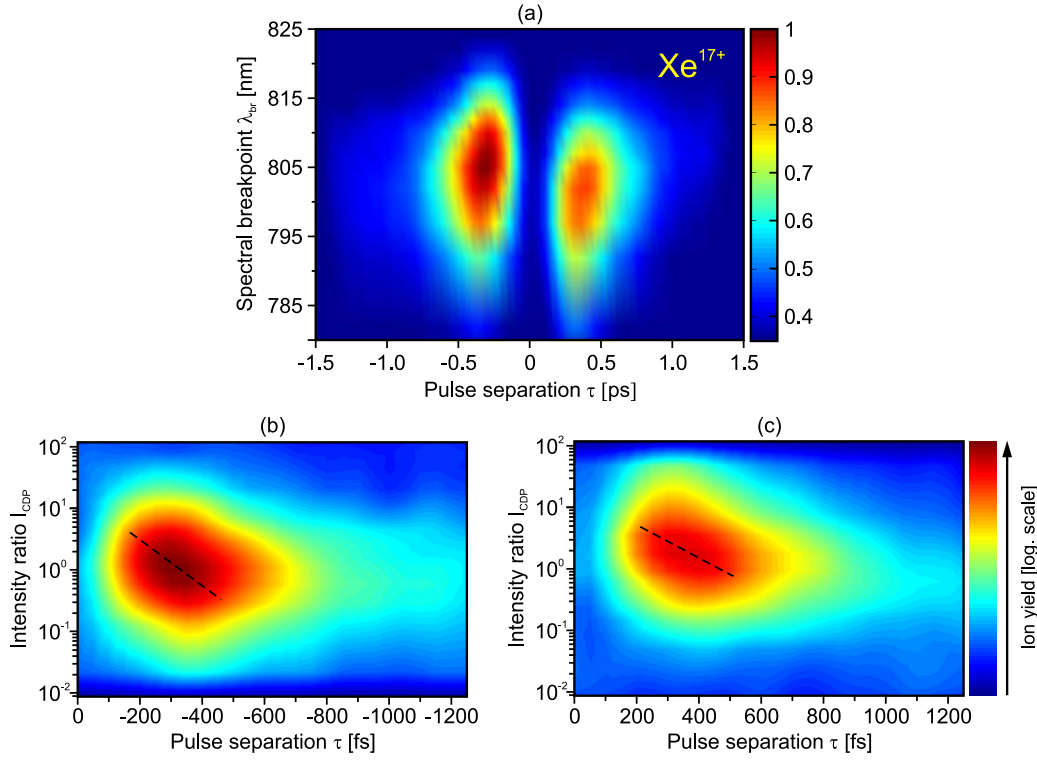


**Figure 3.13:** Top: Colored double pulse fitness landscape for  $\text{Xe}^{17+}$ , obtained by exposing embedded xenon clusters with laser pulses of a 0.5 mJ energy. Bottom: corresponding  $(\tau, I_{\text{CDP}})$ -landscapes extracted for  $\tau < 0$  (b) and  $\tau > 0$  (c) based on the experimental values of  $I_{\text{CDP}}$  in Fig. 3.12(a), inset. The roughly sketched dashed lines are to guide the eyes, indicating the shift of the optimum delay  $|\tau_{\text{max}}^\lambda|$  (for each spectral breakpoint) towards smaller values when the leading pulses get stronger.

detuned leading pulse results in an increased charge-buildup and hence a larger expansion rate of the cluster, when compared to a *red*-detuned leading pulse of the same intensity. Second, for highest- $q$  (with  $q > 15$ ) the maximal yield in both landscapes is always found for negative  $\tau$ , i.e.,  $\tau_{\text{opt}}^{q+} < 0$ . This indicates that a negative global chirp is more favorable for an extreme charging of clusters. Detailed discussion about this property is given in Publications A.1.7.

To demonstrate the difference of the strong-field response between atoms and clusters, Fig. 3.14 visualizes the full fitness landscapes for the low ionization stages, i.e.,  $\text{Xe}^{3+}$ – $\text{Xe}^{5+}$  at an input energy of 0.5 mJ. With increasing charge state the signal modifies from a double T-girder shape to a clear double-hill structure. This change reflects the onset of a cluster mediated response. Most of the lower charge state signal up to  $q = 3$  is generated by barrier-suppression ionization (BSI) of Xe atoms leaking into the interaction region from the pick-up cell, see Fig. 3.14(a). Since the BSI rate of atoms is strongly dependent on laser intensity [199], the yield therefore peaks in the region where only single pulses are practically present (gray area in Fig. 2.22). The landscape of  $\text{Xe}^{4+}$  (Fig. 3.14(b)) is the first one which shows a change in the response function. Two new strong features appear separated from the zero  $\tau_{\text{CDP}}$  setting. For  $\text{Xe}^{5+}$  (Fig. 3.14(c)) and higher charge states,



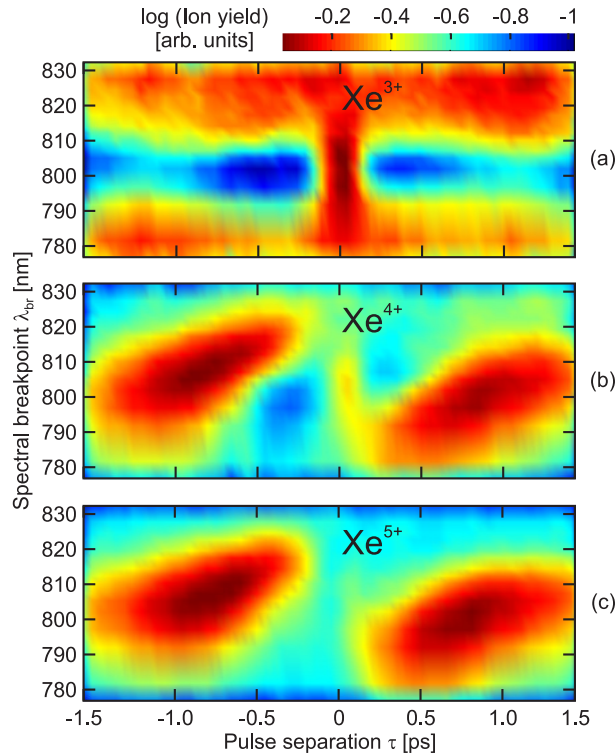


**Figure 3.14:** Colored double pulse fitness landscapes for  $\text{Xe}^{q+}$  ions ( $q = 3 - 5$ ) recorded in the Coulomb explosion of embedded xenon clusters. Due to the presence of Xe gas leaking from the pick-up gas cell into the interaction region, the lower  $q$ -states show additional features of atomic BSI ((a) and (b)).

the double-hill feature dominates, whereas the atomic contribution has disappeared.

We sum up here the key achievements from the CDPFL, which will be listed and briefly discussed below. (i) As function of charge state, the maxima show a systematic shift towards smaller pulse separation. (ii) The optimal  $I_{\text{CDP}}$  modifies as a function of pulse energy. (iii) The local maxima are not equal in height and the global maxima for highly charged ions are always found in the left, corresponding to colored double pulses with negative global chirp. (iv) The plasmon-induced charge state bleaching of clusters can be observed. (v) The charge state-selective intensity threshold values for the leading pulses can be determined, showing a steplike behavior in good agreement with previous observation.

**Analyzing the maximum positions.** Studying the optimal settings  $(\lambda_{\text{opt}}^{q+}, \tau_{\text{opt}}^{q+})$  leading to the maximum yield in the charge state-selective landscape will give clues about the extreme charging conditions. The optical delay position of the maximum ion yield as function of  $q$ ,  $|\tau_{\text{opt}}^{q+}|$ , reduces from about 900 fs for  $\text{Xe}^{5+}$  to 175 fs for  $\text{Xe}^{23+}$  (Fig. 3.15, top). In between 0.5 and 1.9 mJ, one observes no clear dependence of  $\tau_{\text{opt}}^{q+}$  (with  $q > 15$ ) on the chosen laser input energy. Most notably, the value of  $\tau_{\text{opt}}^{23+}$  obtained at the optimal intensity ratio marks the condition for the most effective energy deposition resulting in the highest ionization states (see Fig. 3.15, bottom). This might link to the avalanche-like

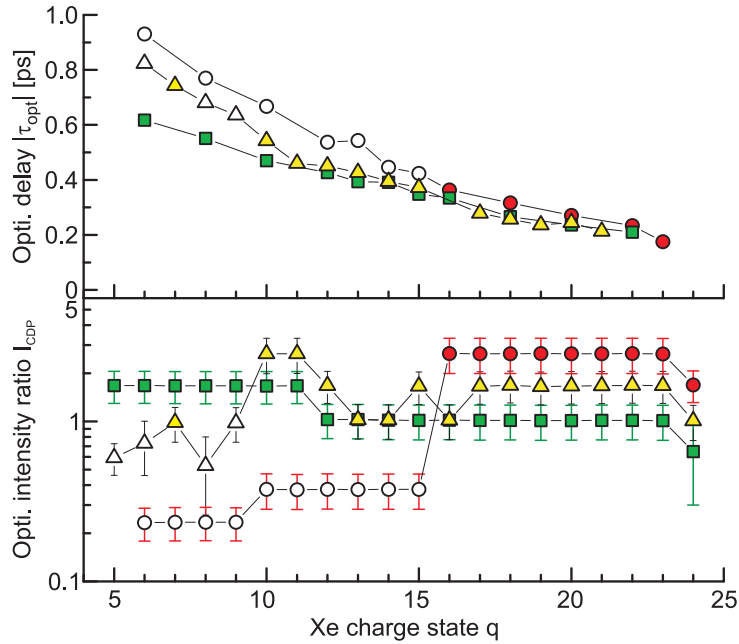


**Figure 3.15:** Charge state-selective optimal delay  $\tau_{\text{opt}}^{q+}$  (top) and optimal intensity ratio  $I_{\text{CDP}}$  (bottom) values extracted from the fitness landscapes. The symbols correspond to the laser energy chosen (circles: 0.5 mJ; triangles: 1.0 mJ; squares: 1.9 mJ), with filled and open symbols for negative and positive  $\tau_{\text{opt}}^{q+}$ , respectively.

ionization reported recently by Döppner *et al.* [163]. We will be back to this point later in the discussion about the charge state-selective threshold intensity.

The occurrence of an optimal delay can again be understood on the basis of the plasmon enhanced multi-ionization mechanism [24]. At the arrival of the leading pulse, the weakest bound electrons are removed leading to the formation of the nanoplasma [17]. It is well accepted that most energy can be captured by clusters through the Mie plasmon, which is the electron dipole resonance of a small metallic particle [18]. Initially, the Mie resonance  $\omega_{\text{Mie}}$  is well beyond the driving laser frequency  $\omega_0$ . Through cluster expansion, the ion background density reduces and subsequently drives the system into proper resonance conditions, i.e.,  $\omega_{\text{Mie}} \sim \omega_0$ . This process introduces a time lag of some hundred femtoseconds, depending on the chosen laser parameters and the size of the particles. We however note that this two-step ionization mechanism merely provides a simple picture to understand the results delivered by the CDPFL measurements. In fact, there might be several more sophisticated mechanisms, which can only be resolved with the use of more complex pulse structures rather than double-pulses, as shown later in the closed-loop optimization experiments.

**Pulse structure at optimal conditions.** Based on the experimental laser spectrum (Fig. 3.12(a), inset) and the  $(\tau_{\text{CDP}}, \lambda_{\text{CDP}})$  positions giving the global maximum of the highest- $q$  ( $q > 20$ ) ions for different applied pulse energies, the corresponding colored double pulses have been calculated as depicted in Fig. 3.16. Two features are considered

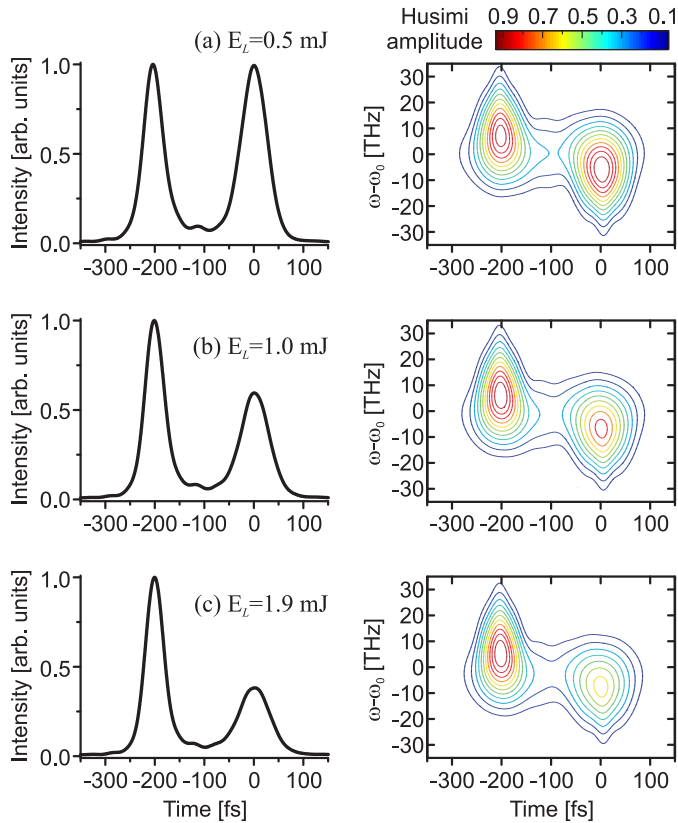


**Figure 3.16:** Optimal colored double pulses leading to the most effective generation of high charge states for different pulse energies (as indicated). Left column: calculated temporal intensities based on the measured laser spectrum (Fig. 3.12(a), inset). Right column: corresponding Husimi distributions. Notably, although the prepulse intensity (top to bottom) is remarkably stronger the optimal delays are comparable. Additionally, the postpulses are clearly redshifted (right column).

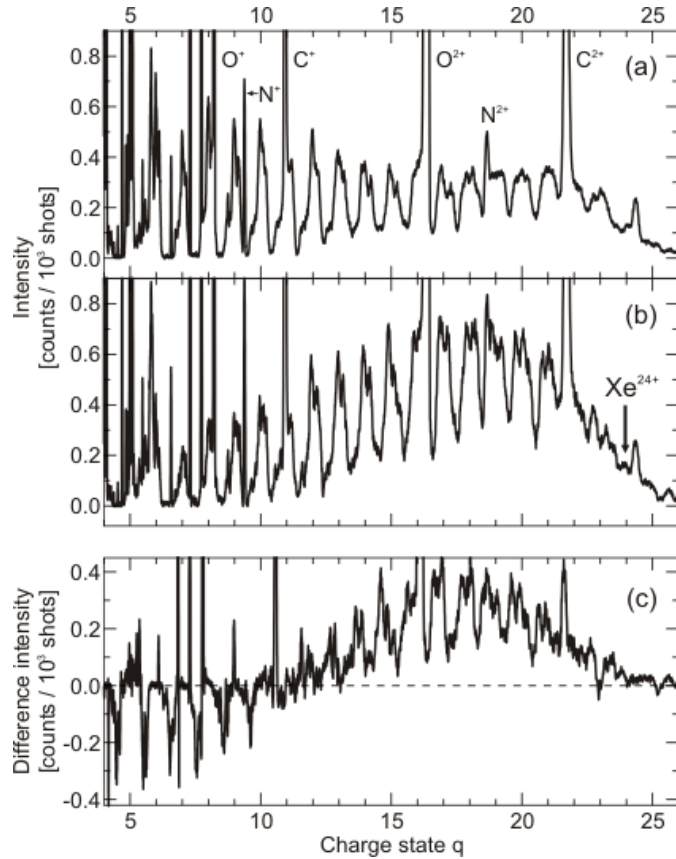
here with respect to the pulse intensity and to the global chirp. First, a stronger leading pulse tends to be best suited for the production of the highly charged ions, in contrast to the findings in silver clusters shown previously. Probably, for an efficient generation of highly charged ions, a certain number of quasifree electrons has to be released with the intense leading pulse through inner ionization to induce an extreme charging later when the trailing pulse arrives at resonance. In addition, while the leading pulses are significantly stronger (see Fig. 3.16(a)–(c)), the respective optimal delays are comparable ( $\sim 200$  fs). This might hint at a characteristic expansion rate of the system under the specific experimental conditions, e.g., cluster composition and the laser wavelength.

Second, the Husimi distributions show that irrespective of the applied energies, all optimal CDPs have a blue-detuned leading pulse and a red-detuned trailing pulse. Naively, such CDPs correspond to negatively stretched pulses [45, 60], and therefore best suited to adapt to the red-shifted Mie-frequency of the expanding cluster. Further details about this issue are given in Publications A.1.7.

**Plasmon-Induced Charge State Bleaching.** It has been observed earlier that the *shape* of the charge state distributions changes under slight modifications of the laser parameters [42, 189], i.e., maintaining laser energy and subpulse duration. CDPFL is capable of revealing this feature in a single scan.

Exemplarily,  $\text{Xe}^{6+}$  and  $\text{Xe}^{23+}$  are chosen as representatives for different ion charge

**Figure 3.17:** Charge state spectra obtained by exposing embedded xenon clusters to intense colored double pulses leading to the maximum yields of  $\text{Xe}^{6+}$  (top,  $\tau_{\text{CDP}} \simeq 850$  fs,  $\lambda_{\text{CDP}} \simeq 812$  nm) and  $\text{Xe}^{23+}$  (middle,  $\tau_{\text{CDP}} \simeq -200$  fs,  $\lambda_{\text{CDP}} \simeq 810$  nm). For comparison, the difference spectrum is also displayed (bottom). Clearly, the different colored double pulse composition results in a significant modification of the charge state distribution favoring high- $q$  ion production for the latter setting. The pulse energy is 1.9 mJ in this measurement, giving an initial intensity of  $1.0 \times 10^{16}$  W cm $^{-2}$ .



state regimes. In Fig. 3.17, we compare the ion spectra obtained under two different CDP conditions: (i) ( $\tau_{\text{CDP}} \simeq 850$  fs,  $\lambda_{\text{br}} \simeq 812$  nm) maximizing the yield of  $q = 6$ , and (ii) ( $\tau_{\text{CDP}} \simeq -200$  fs,  $\lambda_{\text{CDP}} \simeq 810$  nm) giving the maximum yield of  $\text{Xe}^{23+}$ . Parameter settings for effective generation of low- $q$  and effective high- $q$  ions are clearly separated. Figure 3.18 shows the full landscapes for different input energies. At a pulse energy of, e.g., 1.9 mJ, a clear *minimum* for  $\text{Xe}^{6+}$  appears around laser parameters of ( $\tau_{\text{CDP}} \simeq -200$  fs,  $\lambda_{\text{CDP}} \simeq 810$  nm). Indeed, the signals of the highest charge states exactly cover this region. The evolution how the features transform can be clearly traced when examining the  $q$ -dependent landscapes. Apparently, the effect is evident for a wide range of laser energy settings, see Fig. 3.18(a)–(c). One should emphasize that this particular characteristic only uncovers clearly in the fitness landscape measurements where both intensity ratios and optical delays are systematically probed. For xenon which however may act as a prototype for the rare gas systems, this permits for a general statement. The signals of the lower- $q$  are strongly suppressed whenever the pulse parameters allow for an *effective* charging into extreme ionization states. For a complete discussion, see Publications A.1.8.

**Appearance Intensity Threshold.** Recent work on xenon clusters [163] exposed to intense laser pulses has shown that the threshold intensity for the appearance of given charge state changes with the duration of applied laser pulses. The CDPFL technique allows to tune both intensity ratio and delay of colored double pulses. Therefore, the

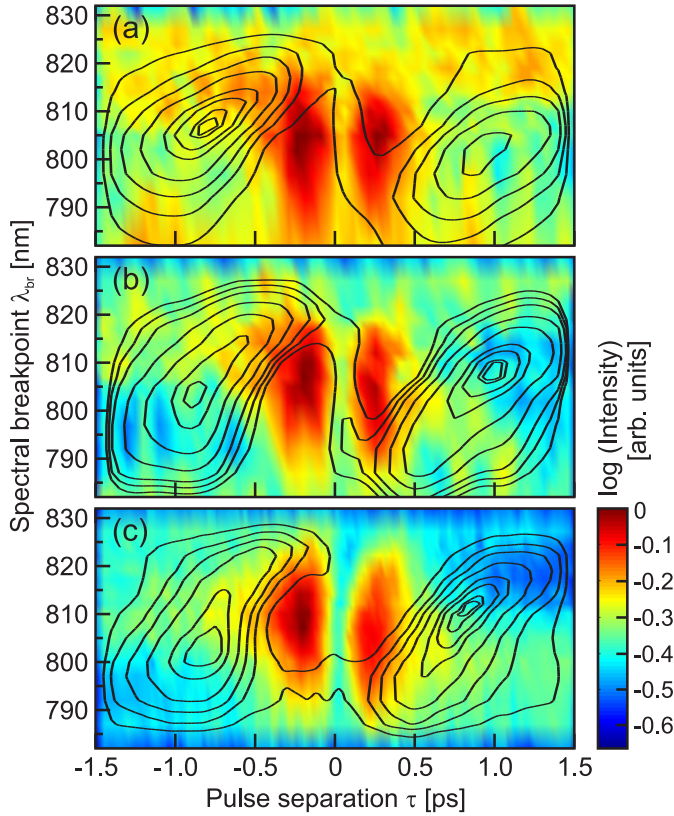


**Figure 3.18:** Comparison of fitness landscapes for selected low (contour lines) and highly (surfaces) charged Xe ions for different laser pulse energy settings (a) 0.5mJ ( $\text{Xe}^{4+}$  and  $\text{Xe}^{23+}$ ), (b) 1.0mJ ( $\text{Xe}^{5+}$  and  $\text{Xe}^{23+}$ ), and (c) 1.9mJ ( $\text{Xe}^{6+}$  and  $\text{Xe}^{23+}$ ). The data show evidence for charge state bleaching.

threshold intensity of the leading pulse for a particular charge state can be studied at the optimal delay, which is expected to give the lowest-appeared value.

As shown earlier in Fig. 3.12, no delay-dependent ion yield can be observed when the one of the subpulses is weak enough. This pulse condition creates an onset signal as seen in Fig. 3.12(a). Providing the leading pulse is sufficiently strong, a significant enhancement of the yield can be obtained at the optimal delay. By studying the maximum yield as function of the intensity ratio, the lowest-appeared intensity threshold can be obtained. Although the estimation of the intensity of the colored subpulses is inexact<sup>3</sup> (with an uncertainty factor of about two), the pronounced yield at the resonance is expected to suppress this limitation.

Figure 3.19 depicts the evolution of the maximum ion yields with the intensity ratio for  $\text{Xe}^{17+}$ , termed as the efficiency spectrum. To attain critical prepulse intensities, the data for each  $q$  have been linearly interpolated in the vicinity of the signal onsets (within the gray area). Figure 3.20(a) shows the appearance intensity thresholds  $I_{\text{app}}$  extracted with this method. The calculations [163] in Fig. 3.20(b) and (c) are also plotted for comparison. Interestingly, a quite low intensity value of below  $4 \times 10^{13} \text{ W cm}^{-2}$  is found for highly charged  $\text{Xe}^{q+}$  up to  $q = 17$ . For the higher charge states, only a slight increase in the appearance intensity thresholds can be identified, finally giving  $8.5 \times 10^{13} \text{ W cm}^{-2}$  for the highest charge state of  $\text{Xe}^{24+}$ . This steplike behavior of the charge state-selective

<sup>3</sup>Due to the slight variation of subpulse durations with  $\tau$  and  $\lambda_{\text{br}}$ .

**Figure 3.19:** Efficiency spectra showing the optimal yields vs. the relative intensity ratio  $I_{\text{CDP}}$  for the left- ( $\tau < 0$ , circles) and right-hand ( $\tau > 0$ , squares) maxima in the CDP fitness landscape of  $\text{Xe}^{17+}$ . The method to extract the values from the fitness landscapes is described in the text. The error represents the deviation between the fitted and the experimental maxima. Thin lines are used to guide the eyes. By interpolation of the data near the onset (gray area) the appearance intensity thresholds are deduced. For  $\text{Xe}^{17+}$ , a prepulse threshold value of  $\sim 4 \times 10^{13} \text{ W cm}^{-2}$  has been determined with this method.

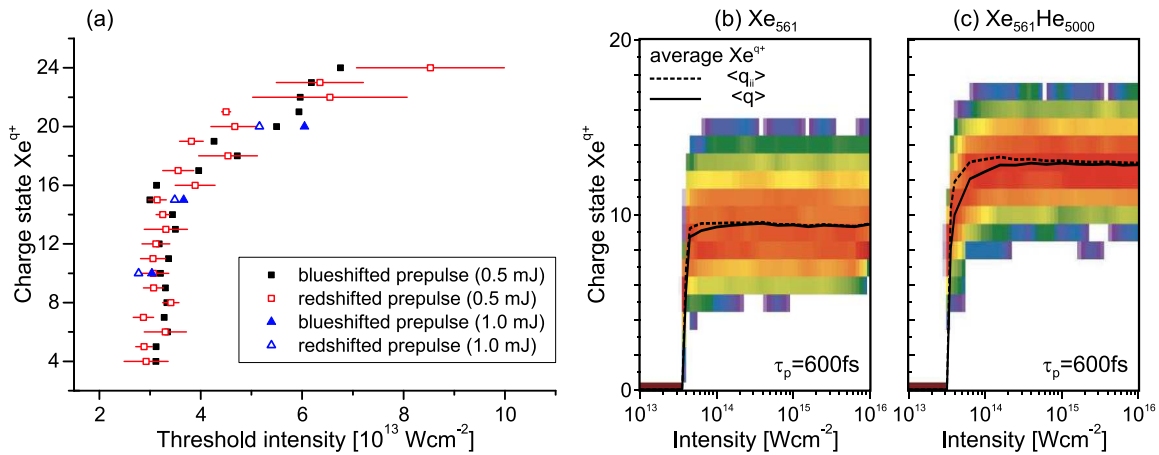
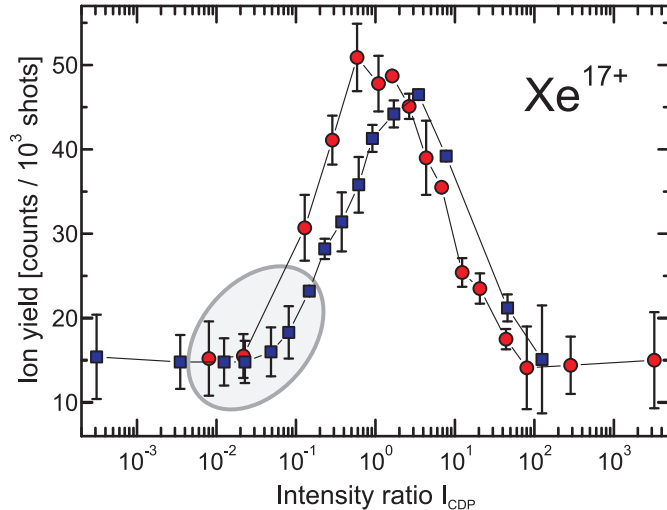


**Figure 3.20:** (a): Charge state-dependent appearance intensity thresholds  $I_{\text{app}}^{\text{pre}}$  extracted from the CDPFL for  $\text{Xe}^{q+}$  with an input energy of  $E_L = 0.5 \text{ mJ}$ . To prove that the values of are independent of the chosen  $E_L$ , some reference data (for  $q=5, 15$ , and  $20$ ) for  $1 \text{ mJ}$  excitations are included. (b) and (c): Calculated  $\text{Xe}^{q+}$  spectra vs. laser peak intensity from pure  $\text{Xe}_{561}$  and  $\text{Xe}_{561}\text{He}_{5000}$ , respectively, exposed to  $600 \text{ fs}$  pulses (adapted from [163]). Note that the experiment and theory are in good agreement.

intensity thresholds has also been observed in a stretched pulse approach using the focus-scan method [163]. We note that the threshold intensity value of  $\text{Xe}^{24+}$  found in this work is more than three orders of magnitude lower when compared to the strong field BSI threshold of the xenon atom [200], giving evidence for a pronounced contribution of many body correlation effects in clusters (see, e.g., Ref. [52]).

### Intense colored pulse train approach

In this section we applied the closed-loop optimization technique, but restricted to a certain number of possible pulse shapes, i.e., colored pulse trains introduced in section 2.2.5. Similar to the optimal control experiments on  $\text{Ag}^{q+}$ , the yields of selected  $\text{Xe}^{q+}$  are maximized to find the corresponding optimal pulses shapes. Experiments were performed on about 140-atom Xe clusters irradiated with  $\sim 40$ -fs pulses at an initial intensity of

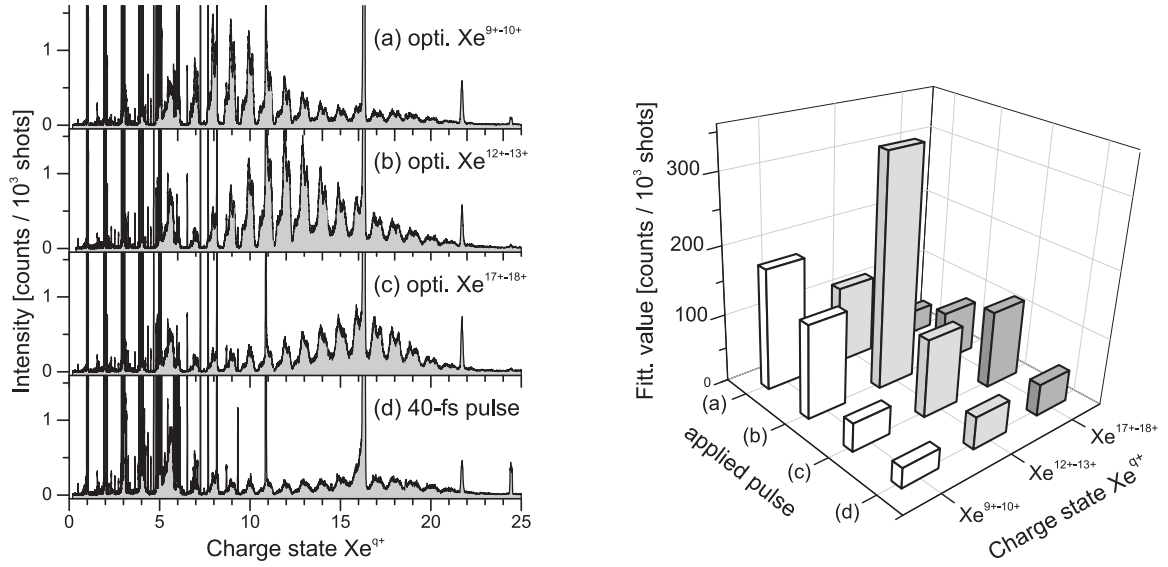


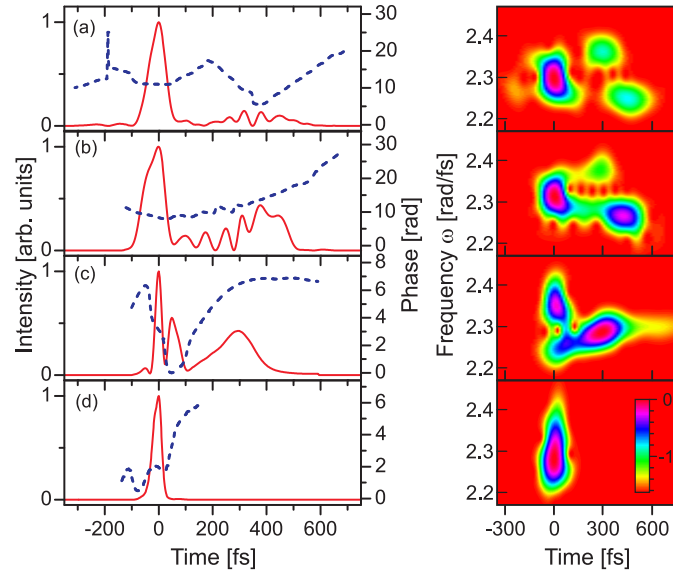
**Figure 3.21:** Left: Selective charge-state optimal spectra of  $\text{Xe}^{q+}$  obtained by applying the restricted closed-loop control with feedback value assigned as the total yields of different highly charged ions  $\text{Xe}^{q+}$ : (a)  $q=9-10$ , (b)  $q=12-13$ , and (c)  $q=17-18$ . 40-fs pulse excitation (d) is shown for comparison. See Fig. 3.21 for the corresponding laser pulses. Right: Comparison of respective fitness values for the cases (a)–(d).

$8 \times 10^{15} \text{ Wcm}^{-2}$ . The tailored pulses were characterized with SHG FROG, using the phase-only approach to remove the time ambiguity (see section 2.2.3).

Figures 3.21(a)–(c) show the charge state spectra, obtained by exposing the clusters to different pulse shapes (see Fig. 3.22) that maximize the yields of selected highly charged ions. Excitation with 40 fs bandwidth-limited pulses is also visualized for comparison (Fig. 3.21(d)), illustrating an inefficient charging. On the contrary, shaping the pulses leads to maximum yields of the selected ions. The optimizations show that the simple view of a two-step ionization is not longer sustainable. Instead, e.g., a sequence of three pulses leads to effective generation of high- $q$  values. By tuning the optical delays, relative intensity ratios, and to certain extent, the spectral components within the pulses, the ionic distribution can be controlled. This might be appealing for applications which require an efficient  $q$ -selective particle or X-ray source at a high repetition rate. For instance, the charged ion  $\text{Xe}^{10+}$  is directly related to the production of 13.5-nm X-ray [201], interesting for the extreme ultraviolet lithography.

After the theoretical work of Martchenko *et al.* [43], a three-pulse sequence optimizes the ionization of free xenon clusters: the first subpulse triggers the cluster expansion, while the second pulse optimizes the enhanced ionization [170] and the third drives the plasmon-induced ionization at resonance [24, 30]. In our experiments, the maximum yield in the CDP fitness landscapes of the selected highly charged ions has been used as reference for the corresponding multipulse optimization search. Usually, 10-20% enhancements have been obtained for the closed-loop feedback measurements, which confirm the need of a

**Figure 3.22:** Laser pulses corresponding to the fragment spectra depicted in Fig. 3.21: Optimized pulses giving the maximum yield of  $\text{Xe}^{q+}$  with (a)  $q=9-10$ , (b)  $q=12-13$ , and (c)  $q=17-18$ , and (d) a 40-fs pulse as a reference. Left: Intensities (solid) and phases (dashed) vs. time. Right: Corresponding Husimi distributions. Notably, a three pulse sequence leads to the effective generation of the highest- $q$  values (c).



third pulse and might indicate the contribution of other currently unresolved processes, e.g., the helium resonance.

For the first time, to our knowledge, intense triple-pulses have been experimentally observed to effectively ionize clusters. This is due to a number of major developments. First, full characterization of the optimized pulses and the use of the joint time-frequency Husimi representation help to clearly identify the pulse structures, when compared to the time or frequency-domain only (cf. Fig. 3.22, left and right column). Second, the applications of simple pulse trains might assist the evolutionary algorithm to easily find the well-separated pulse structures.

We note however that the restricted optimization using colored pulse trains provides only optimized pulse shapes "close" to the optimal solutions. On the one hand, it allows for understanding the experimental results within a simple picture such as the plasmon-enhanced ionization model. In addition, it also permits for simulations to mimic the experiments in an accessible manner. On the other hand, further insights into the system require the use of more complex pulse shapes. Within our program, further developments are in progress: (i) systematic scans with other parameters, e.g., colored triple pulses through tuning optical delays or relative intensities; (ii) generation of more complex pulse structures, such as *chirped* pulse trains, for optimization; (iii) hybrid-encoding evolutionary algorithms, in which the solutions found by the simple optimization above will be used as seeds for the subsequent free-optimization; (iv) optimization on computers using similar encoding methods assists to analyze the experimental results.



# Chapter 4

## Conclusions and Outlook

This work investigates the strong-field laser-induced ionization dynamics in embedded clusters applying the femtosecond pulse shaping techniques. The major achievements are as follows:

- With respect to the characterization of ultrashort laser pulses, we have developed a pulse shaper-assisted technique to remove the time-ambiguity present in SHG FROG.<sup>1</sup> This allows to measure both the amplitude and phase of tailored laser pulses with a high sensitivity and accuracy.
- For a pulse shaper placed prior to a CPA system, shaper-generated pulse replicas are distorted by propagating through the amplifier and might lead to ambiguities in analyzing the experimental results. We have extended a technique to form clean *intense* pulse trains using phase-only shaping. These well-defined pulse structures can be used to perform multi-parameter scans or even closed-loop feedback control experiments. An optical approach has proven that these pulse trains, though simple, are able to reveal several crucial characteristics of the system, which are also interesting for study of the strong-field ionization of clusters.
- Closed-loop optimization experiments on silver clusters in intense laser pulses have shown the following. (i) A double-pulse with a small leading pulse effectively ionizes the clusters, resulting in the maximum yield of the highly charged ions, as well as an enhancement of the highest charge states. (ii) A negative chirp during the main pulse hints at a dynamic frequency locking to the cluster plasmon. (iii) By tuning the temporal structure of ultrashort laser pulses, the yield for selected charge states can be maximized, giving rise to promising applications of high-efficient particle or X-ray sources. Similar results have been obtained for embedded xenon clusters.

---

<sup>1</sup>Second-Harmonic Generation Frequency-Resolved Optical Gating

- CDPFL<sup>2</sup> studies on xenon clusters have provided further insights into the cluster dynamics. A number of new effects are observed, i.e.,: (i) optimal double-pulse shapes with stronger leading pulses are more suited for an extreme charging in the clusters at high pulse energies; (ii) An enhancement of the yield of highly charged ions has been obtained for negative pulse separations, which correspond to the double pulses with a blue-detuned leading pulse and a red-detuned trailing pulse; (iii) The experimental conditions for *plasmon-induced charge state bleaching* have been determined in clusters.
- Three-pulse sequences are found to maximize the yield of selected highly charged ions, when exposing xenon clusters to intense laser pulses. The results might be related to earlier reported simulations. However, further work is necessary to identify the role of each pulse in the ionization processes.

In the following, we outline suggestions for future experimental work, mainly emphasizing on the applications of intense colored pulse trains.

First, CDPFL technique has proven to be a powerful tool to study cluster nonlinear dynamics. By changing the source conditions, e.g., the mean-size of helium droplets or embedded clusters, the impact of the helium surrounding and different ionization processes such as enhanced ionization or resonant charging might be classified. Within this context, multi-parameter scans or even closed-loop feedback control scheme employed colored pulse trains will be helpful to analyze and identify the contribution in the ionization dynamics.

Second, in terms of the laser intensity, with the new upgraded CPA system (7-10 mJ, 50 fs, 1 kHz), intensities up to  $10^{17}$  W cm<sup>-2</sup> can be achieved, allowing to perform optimal control experiments in an extended intensity regime. With this respect, the phase-only nature of colored pulse trains makes it possible to realize such kind of experiments.

Third, in terms of the laser wavelength, well-separated colored pulse trains can be used to easily generate trains of higher-order harmonics such as the second- or third-harmonic generation in a single laser beam.<sup>3</sup> Therefore, similar strong-field experiments on clusters at other laser wavelengths ( $\sim 405$  or  $270$  nm) can be performed in the future.

Finally, a hybrid-encoding evolutionary algorithm can be developed, in which the solutions found by a restricted closed-loop optimization will serve as seeds for the final free-optimization step. This will accelerate the search and assist the algorithm to find the optimal solution.

---

<sup>2</sup>Colored Double Pulse Fitness Landscape

<sup>3</sup>See, e.g., Fig. 2.11.

# Bibliography

- [1] M. Protopapas, C. Keitel, and P. Knight, “Atomic physics with super-high intensity lasers,” *Rep. Prog. Phys.* **60**, 389–486 (1997).
- [2] V. Krainov and M. Smirnov, “Cluster beams in the super-intense femtosecond laser pulse,” *Phys. Rep.-Rev. Sec. Phys. Lett.* **370**, 237–331 (2002).
- [3] H. Haberland, “Experimental methods,” in “Clusters of Atoms and Molecules I,” vol. 52 of *Springer Series in Chemical Physics*, H. Haberland, ed. (Springer-Verlag, Berlin, 1995).
- [4] T. Ditmire, R. A. Smith, J. W. G. Tisch, and M. H. R. Hutchinson, “High Intensity Laser Absorption by Gases of Atomic Clusters,” *Phys. Rev. Lett.* **78**, 3121–3124 (1997).
- [5] Y. L. Shao, T. Ditmire, J. W. G. Tisch, E. Springate, J. P. Marangos, and M. H. R. Hutchinson, “Multi-keV electron generation in the interaction of intense laser pulses with xe clusters,” *Phys. Rev. Lett.* **77**, 3343–3346 (1996).
- [6] T. Ditmire, J. Tisch, E. Springate, M. Mason, N. Hay, R. Smith, I. Marangos, and M. Hutchinson, “High energy ions produced in explosions of superheated atomic clusters,” *Nature* **386**, 54–56 (1997).
- [7] A. McPherson, B. Thompson, A. Borisov, K. Boyer, and C. Rhodes, “Multiphoton-induced X-ray emission at 4-5 keV from Xe atoms with multiple core vacancies,” *Nature* **370**, 631–634 (1994).
- [8] T. Ditmire, J. Zweiback, V. Yanovsky, T. Cowan, G. Hays, and K. Wharton, “Nuclear fusion from explosions of femtosecond laser-heated deuterium clusters,” *Nature* **398**, 489–492 (1999).
- [9] J. Zweiback, R. A. Smith, T. E. Cowan, G. Hays, K. B. Wharton, V. P. Yanovsky, and T. Ditmire, “Nuclear fusion driven by coulomb explosions of large deuterium clusters,” *Phys. Rev. Lett.* **84**, 2634–2637 (2000).
- [10] K. W. Madison, P. K. Patel, M. Allen, D. Price, R. Fitzpatrick, and T. Ditmire, “Role of laser-pulse duration in the neutron yield of deuterium cluster targets,” *Phys. Rev. A* **70**, 053201 (2004).
- [11] L. M. Chen, F. Liu, W. M. Wang, M. Kando, J. Y. Mao, L. Zhang, J. L. Ma, Y. T. Li, S. V. Bulanov, T. Tajima, Y. Kato, Z. M. Sheng, Z. Y. Wei, and J. Zhang, “Intense High-Contrast Femtosecond K-Shell X-Ray Source from Laser-Driven Ar Clusters,” *Phys. Rev. Lett.* **104**, 215004 (2010).

- [12] D. Attwood, *Soft X-Rays and Extreme Ultraviolet Radiation: Principles and Applications* (Cambridge University Press, New York, 2007).
- [13] T. Ditmire, R. Smith, and M. Hutchinson, “Plasma waveguide formation in predisassociated clustering gases,” *Opt. Lett.* **23**, 322–324 (1998).
- [14] V. Kumarappan, K. Kim, and H. Milchberg, “Guiding of intense laser pulses in plasma waveguides produced from efficient, femtosecond end-pumped heating of clustered gases,” *Phys. Rev. Lett.* **94**, 205004 (2005).
- [15] E. Esarey, C. B. Schroeder, and W. P. Leemans, “Physics of laser-driven plasma-based electron accelerators,” *Rev. Mod. Phys.* **81**, 1229–1285 (2009).
- [16] P. Zeitoun, G. Faivre, S. Sebban, T. Mocek, A. Hallou, M. Fajardo, D. Aubert, P. Balcou, F. Burgy, D. Douillet, S. Kazamias, G. de Lacheze-Murel, T. Lefrou, S. le Pape, P. Mercere, H. Merdji, A. Morlens, J. Rousseau, and C. Valentin, “A high-intensity highly coherent soft X-ray femtosecond laser seeded by a high harmonic beam,” *Nature* **431**, 426–429 (2004).
- [17] T. Ditmire, T. Donnelly, A. Rubenchik, R. Falcone, and M. Perry, “Interaction of intense laser pulses with atomic clusters,” *Phys. Rev. A* **53**, 3379–3402 (1996).
- [18] G. Mie, “Beiträge zur Optik trüber Medien, speziell kolloidaler Metallösungen,” *Ann. Phys.* **25**, 377–445 (1908).
- [19] E. Springate, N. Hay, J. Tisch, M. Mason, T. Ditmire, M. Hutchinson, and J. Marangos, “Explosion of atomic clusters irradiated by high-intensity laser pulses: Scaling of ion energies with cluster and laser parameters,” *Phys. Rev. A* **61**, 063201 (2000).
- [20] A. Moore, K. Mendham, D. Symes, J. Robinson, E. Springate, M. Mason, R. Smith, J. Tisch, and J. Marangos, “Control parameters for ion heating and X-ray emission from laser induced cluster explosion,” *Appl. Phys. B-Lasers Opt.* **80**, 101–107 (2005).
- [21] J. Jha, D. Mathur, and M. Krishnamurthy, “Enhancement of x-ray yields from heteronuclear cluster plasmas irradiated by intense laser light,” *J. Phys. B* **38**, L291–L299 (2005).
- [22] J. Jha, D. Mathur, and M. Krishnamurthy, “Engineering clusters for table-top acceleration of ions,” *Appl. Phys. Lett.* **88**, 041107 (2006).
- [23] J. Zweiback, T. Ditmire, and M. D. Perry, “Femtosecond time-resolved studies of the dynamics of noble-gas cluster explosions,” *Phys. Rev. A* **59**, R3166–9 (1999).
- [24] L. Köller, M. Schumacher, J. Köhn, S. Teuber, J. Tiggesbäumker, and K.-H. Meiwes-Broer, “Plasmon-Enhanced Multi-Ionization of Small Metal Clusters in Strong Femtosecond Laser Fields,” *Phys. Rev. Lett.* **82**, 3783–3786 (1999).
- [25] E. Parra, I. Alexeev, J. Fan, K. Kim, S. McNaught, and H. Milchberg, “X-ray and extreme ultraviolet emission induced by variable pulse-width irradiation of Ar and Kr clusters and droplets,” *Phys. Rev. E* **62**, R5931–R5934 (2000).

- [26] J. Zweiback, T. Ditmire, and M. Perry, “Resonance in scattering and absorption from large noble gas clusters,” *Opt. Exp.* **6**, 236–242 (2000).
- [27] M. Schnürer, S. Ter-Avetisyan, H. Stiel, U. Vogt, W. Radloff, M. Kalashnikov, W. Sandner, and P. Nickles, “Influence of laser pulse width on absolute EUV-yield from Xe-clusters,” *Eur. Phys. J. D* **14**, 331–335 (2001).
- [28] Y. Fukuda, K. Yamakawa, Y. Akahane, M. Aoyama, N. Inoue, H. Ueda, and Y. Kishimoto, “Optimized energetic particle emissions from Xe clusters in intense laser fields,” *Phys. Rev. A* **67**, 061201 (2003).
- [29] K. Mendham, J. Tisch, M. Mason, N. Hay, and J. Marangos, “Control of laser heating in clusters through variation in temporal pulse shape,” *Opt. Express* **11**, 1357–1364 (2003).
- [30] T. Döppner, T. Fennel, T. Diederich, J. Tiggesbäumker, and K.-H. Meiwes-Broer, “Controlling the Coulomb Explosion of Silver Clusters by Femtosecond Dual-Pulse Laser Excitation,” *Phys. Rev. Lett.* **94**, 013401 (2005).
- [31] T. Fennel, T. Döppner, J. Passig, C. Schaal, J. Tiggesbäumker, and K.-H. Meiwes-Broer, “Plasmon-Enhanced Electron Acceleration in Intense Laser Metal-Cluster Interactions,” *Phys. Rev. Lett.* **98**, 143401 (2007).
- [32] P. Golovinski, “Laser wavelength dependence for strong-field-induced excitation in clusters,” *Laser Phys.* **9**, 1048–1052 (1999).
- [33] G. Petrov and J. Davis, “Impact of the laser wavelength on the dynamics of Xe cluster plasma produced by an intense ultrashort laser pulse,” *Phys. Plasmas* **13**, 033106 (2006).
- [34] M. Kundu and D. Bauer, “Optimizing the ionization and energy absorption of laser-irradiated clusters,” *Phys. Plasmas* **15**, 033303 (2008).
- [35] T. Ditmire, E. Springate, J. Tisch, Y. Shao, M. Mason, N. Hay, J. Marangos, and M. Hutchinson, “Explosion of atomic clusters heated by high-intensity femtosecond laser pulses,” *Phys. Rev. A* **57**, 369 (1998).
- [36] V. Kumarappan, M. Krishnamurthy, and D. Mathur, “Asymmetric High-Energy Ion Emission from Argon Clusters in Intense Laser Fields,” *Phys. Rev. Lett.* **87**, 085005 (2001).
- [37] V. Kumarappan, M. Krishnamurthy, D. Mathur, and L. Tribedi, “Effect of laser polarization on X-ray emission from  $\text{Ar}_n$  ( $n = 200\text{--}10^4$ ) clusters in intense laser fields,” *Phys. Rev. A* **63**, 023203 (2001).
- [38] E. Lamour, C. Prigent, J. Rozet, and D. Vernhet, “Physical parameter dependence of the X-ray generation in intense laser-cluster interaction,” *Nucl. Instr. Meth. B* **235**, 408–413 (2005).
- [39] U. Keller, “Recent developments in compact ultrafast lasers,” *Nature* **424**, 831–838 (2003).

- [40] A. Monmayrant, S. Weber, and B. Chatel, “A newcomer’s guide to ultrashort pulse shaping and characterization,” *J. Phys. B-At. Mol. Opt. Phys.* **43**, 103001 (2010).
- [41] R. Judson and H. Rabitz, “Teaching lasers to control molecules,” *Phys. Rev. Lett.* **68**, 1500–1503 (1992).
- [42] S. Zamith, T. Martchenko, Y. Ni, S. Aseyev, H. Muller, and M. Vrakking, “Control of the production of highly charged ions in femtosecond-laser cluster fragmentation,” *Phys. Rev. A* **70**, 011201 (2004).
- [43] T. Martchenko, C. Siedschlag, S. Zamith, H. Muller, and M. Vrakking, “Optimal control of femtosecond laser-cluster interactions,” *Phys. Rev. A* **72**, 053202 (2005).
- [44] T. Fennel, K.-H. Meiwes-Broer, J. Tiggesbäumker, P.-G. Reinhard, P. M. Dinh, and E. Surau, “Laser-driven nonlinear cluster dynamics,” *Rev. Mod. Phys.* **82**, 1793–1842 (2010).
- [45] G. Vogt, P. Nuernberger, R. Selle, F. Dimler, T. Brixner, and G. Gerber, “Analysis of femtosecond quantum control mechanisms with colored double pulses,” *Phys. Rev. A* **74**, 033413 (2006).
- [46] S. Göde, Ph.D. thesis, Universität Rostock, in preparation.
- [47] J. Tiggesbäumker and F. Stienkemeier, “Formation and properties of metal clusters isolated in helium droplets,” *Phys. Chem. Chem. Phys.* **9**, 4748–4770 (2007).
- [48] R. Trebino, *Frequency-Resolved Optical Gating: The Measurement of Ultrashort Laser Pulses* (Kluwer Academic, London, 2000).
- [49] P. Hilse, M. Moll, M. Schlanges, and T. Bornath, “Laser-cluster-interaction in a nanoplasma-model with inclusion of lowered ionization energies,” *Laser Phys.* **19**, 428–436 (2009).
- [50] A. Mikaberidze, U. Saalman, and J. M. Rost, “Energy absorption of xenon clusters in helium nanodroplets under strong laser pulses,” *Phys. Rev. A* **77**, 041201 (2008).
- [51] A. Mikaberidze, U. Saalman, and J. M. Rost, “Laser-Driven Nanoplasmas in Doped Helium Droplets: Local Ignition and Anisotropic Growth,” *Phys. Rev. Lett* **102**, 128102 (2009).
- [52] T. Fennel, L. Ramunno, and T. Brabec, “Highly charged ions from laser-cluster interactions: Local-field-enhanced impact ionization and frustrated electron-ion recombination,” *Phys. Rev. Lett.* **99**, 233401 (2007).
- [53] J.-C. Diels and W. Rudolph, *Ultrashort Laser Pulse Phenomena* (Academic Press, London, 2006).
- [54] T. Brabec and F. Krausz, “Nonlinear Optical Pulse Propagation in the Single-Cycle Regime,” *Phys. Rev. Lett.* **78**, 3282–3285 (1997).
- [55] R. N. Bracewell, *The Fourier transform and its applications* (McGraw-Hill, New York, 2000).

- [56] R. Trebino, K. W. DeLong, D. N. Fittinghoff, J. N. Sweetser, M. A. Krumbügel, B. A. Richman, and D. J. Kane, “Measuring ultrashort laser pulses in the time-frequency domain using frequency-resolved optical gating,” *Rev. Sci. Instrum.* **68**, 3277–3295 (1997).
- [57] C. Iaconis and I. Walmsley, “Spectral phase interferometry for direct electric-field reconstruction of ultrashort optical pulses,” *Opt. Lett.* **23**, 792–794 (1998).
- [58] F. Krausz and M. Ivanov, “Attosecond physics,” *Rev. Mod. Phys.* **81**, 163–234 (2009).
- [59] M. Renard, R. Chaux, B. Lavorel, and O. Faucher, “Pulse trains produced by phase-modulation of ultrashort optical pulses: tailoring and characterization,” *Opt. Express* **12**, 473–482 (2004).
- [60] P. Nürnberger, “Differences and analogies between linearly chirped and colored double pulses in the femtosecond regime,” *Opt. Commun.* **282**, 227–235 (2009).
- [61] G. P. Agrawal, *Nonlinear fiber optics* (Academic Press, New York, 2001).
- [62] J. Paye, “The chronocyclic representation of ultrashort light pulses,” *IEEE J. Quantum Electron.* **28**, 2262–2273 (1992).
- [63] L. Cohen, *Time Frequency Analysis : Theory and Applications (Prentice-Hall Signal Processing)* (Prentice Hall PTR, New Jersey, 1994).
- [64] S. Fechner, F. Dimler, T. Brixner, G. Gerber, and D. J. Tannor, “The von Neumann picture: a new representation for ultrashort laser pulses,” *Opt. Express* **15**, 15387–15401 (2007).
- [65] E. Wigner, “On the quantum correction for thermodynamic equilibrium,” *Phys. Rev.* **40**, 0749–0759 (1932).
- [66] K. Husimi, “Some formal properties of the density matrix,” *Prog. Phys. Math. Soc. Japan* **22**, 264–314 (1940).
- [67] W. P. Schleich, *Quantum Optics in Phase Space* (Wiley-VCH, Berlin, 2001).
- [68] A. M. Weiner, “Femtosecond pulse shaping using spatial light modulators,” *Rev. Sci. Instr.* **71**, 1929–1960 (2000).
- [69] D. Tannor, *Introduction to Quantum Mechanics: A Time-Dependent Perspective* (University Science Books, Herndon, 2006).
- [70] A. C. Florean, D. Cardoza, J. L. White, J. K. Lanyi, R. J. Sension, and P. H. Bucksbaum, “Control of retinal isomerization in bacteriorhodopsin in the high-intensity regime,” *Proc. Natl. Acad. Sci. U. S. A.* **106**, 10896–10900 (2009).
- [71] J. Savolainen, R. Fanciulli, N. Dijkhuizen, A. L. Moore, J. Hauer, T. Buckup, M. Motzkus, and J. L. Herek, “Controlling the efficiency of an artificial light-harvesting complex,” *Proc. Natl. Acad. Sci. U. S. A.* **105**, 7641–7646 (2008).

- [72] T. Brixner, N. Damrauer, P. Niklaus, and G. Gerber, “Photoselective adaptive femtosecond quantum control in the liquid phase,” *Nature* **414**, 57–60 (2001).
- [73] R. Levis, G. Menkir, and H. Rabitz, “Selective bond dissociation and rearrangement with optimally tailored, strong-field laser pulses,” *Science* **292**, 709–713 (2001).
- [74] C. Winterfeldt, C. Spielmann, and G. Gerber, “Colloquium: Optimal control of high-harmonic generation,” *Rev. Mod. Phys.* **80**, 117–140 (2008).
- [75] J. Dela Cruz, I. Pastirk, M. Comstock, V. Lozovoy, and M. Dantus, “Use of coherent control methods through scattering biological tissue to achieve functional imaging,” *Proc. Natl. Acad. Sci. U. S. A.* **101**, 16996–17001 (2004).
- [76] A. Assion, T. Baumert, M. Bergt, T. Brixner, B. Kiefer, V. Seyfried, M. Strehle, and G. Gerber, “Control of chemical reactions by feedback-optimized phase-shaped femtosecond laser pulses,” *Science* **282**, 919–922 (1998).
- [77] P. Nuernberger, G. Vogt, T. Brixner, and G. Gerber, “Femtosecond quantum control of molecular dynamics in the condensed phase,” *Phys. Chem. Chem. Phys.* **9**, 2470–2497 (2007).
- [78] F. Träger, ed., *Springer Handbook of Lasers and Optics* (Springer Science + Business Media, Inc., New York, 2007).
- [79] A. Monmayrant, B. Chatel, and B. Girard, “Quantum state measurement using coherent transients,” *Phys. Rev. Lett.* **96**, 103002 (2006).
- [80] J. Degert, W. Wohlleben, B. Chatel, M. Motzkus, and B. Girard, “Realization of a time-domain fresnel lens with coherent control,” *Phys. Rev. Lett.* **89**, 203003 (2002).
- [81] N. Dudovich, B. Dayan, S. M. Gallagher Faeder, and Y. Silberberg, “Transform-limited pulses are not optimal for resonant multiphoton transitions,” *Phys. Rev. Lett.* **86**, 47–50 (2001).
- [82] N. Dudovich, D. Oron, and Y. Silberberg, “Coherent transient enhancement of optically induced resonant transitions,” *Phys. Rev. Lett.* **88**, 123004 (2002).
- [83] Z. Amitay, A. Gandman, L. Chuntunov, and L. Rybak, “Multichannel selective femtosecond coherent control based on symmetry properties,” *Phys. Rev. Lett.* **100**, 193002 (2008).
- [84] A. Pe’er, B. Dayan, A. A. Friesem, and Y. Silberberg, “Temporal shaping of entangled photons,” *Phys. Rev. Lett.* **94**, 073601 (2005).
- [85] A. Yariv and P. Yeh, *Optical waves in crystals* (Wiley, New York, 1984).
- [86] D. Goswami, “Optical pulse shaping approaches to coherent control,” *Phys. Rep.* **374**, 385–481 (2003).
- [87] A. M. Weiner, J. P. Heritage, and E. M. Kirschner, “High-resolution femtosecond pulse shaping,” *J. Opt. Soc. Am. B* **5**, 1563–1572 (1988).



- [88] T. Brixner and G. Gerber, “Femtosecond polarization pulse shaping,” *Opt. Lett.* **26**, 557–559 (2001).
- [89] P. Tournois, “Acousto-optic programmable dispersive filter for adaptative compensation of group delay time dispersion in laser systems,” *Opt. Comm.* **140**, 245–249 (1997).
- [90] F. Verluise, V. Laude, Z. Cheng, C. Spielmann, and P. Tournois, “Amplitude and phase control of ultrashort pulses by use of an acousto-optic programmable dispersive filter: pulse compression and shaping,” *Opt. Lett.* **25**, 575–577 (2000).
- [91] D. Kaplan and P. Tournois, “Theory and performance of the acousto optic programmable dispersive filter used for femtosecond laser pulse shaping,” *J. Phys. IV France* **12**, 69–75 (2002).
- [92] S. Coudreau, D. Kaplan, and P. Tournois, “Ultraviolet acousto-optic programmable dispersive filter laser pulse shaping in kdp,” *Opt. Lett.* **31**, 1899–1901 (2006).
- [93] P. Tournois, “Design of acousto-optic programmable filters in mercury halides for mid-infrared laser pulse shaping,” *Opt. Commun.* **281**, 4054–4056 (2008).
- [94] H. S. Peng, X. J. Huang, Q. H. Zhu, X. D. Wang, K. N. Zhou, X. F. Wei, X. M. Zeng, L. Q. Liu, X. Wang, Y. Guo, D. H. Lin, B. Xu, L. B. Xu, X. L. Chu, and X. M. Zhang, “Silex-i: 300-tw ti:sapphire laser,” *Laser Physics* **16**, 244–247 (2006).
- [95] X. Liang, Y. Leng, C. Wang, C. Li, L. Lin, B. Zhao, Y. Jiang, X. Lu, M. Hu, C. Zhang, H. Lu, D. Yin, Y. Jiang, X. Lu, H. Wei, J. Zhu, R. Li, and Z. Xu, “Parasitic lasing suppression in high gain femtosecond petawatt Ti: sapphire amplifier,” *Opt. Express* **15**, 15335–15341 (2007).
- [96] L. Chuang, L. Xiao-Ming, W. Cheng, L. Yu-Xin, L. Xiao-Yan, L. Ru-Xin, and X. Zhi-Zhan, “Generation of 17-TW 23-fs pulses with a two-stage Ti : Sapphire amplifier at repetition rate 10 Hz,” *Chin. Phys. Lett.* **24**, 1276–1278 (2007).
- [97] F. Legare, M. Najji, P. Lassonde, D. Comtois, V. Crozatier, T. Oksenhendler, H. Anis, and J.-C. Kieffer, “Pulse compression and shaping of broadband optical parametric amplifier laser source,” *Opt. Lett.* **33**, 2824–2826 (2008).
- [98] N. X. Truong, J. Tiggesbäumker, and K. H. Meiwes-Broer, “Intense colored pulse trains: generation, characterization, and applications,” *J. Opt.* **12**, 115201 (2010).
- [99] D. H. Reitze, S. Kazamias, F. Weihe, G. Mullot, D. Douillet, F. Aug, O. Albert, V. Ramanathan, J. P. Chambaret, D. Hulin, and P. Balcou, “Enhancement of high-order harmonic generation at tuned wavelengths through adaptive control,” *Opt. Lett.* **29**, 86–88 (2004).
- [100] N. X. Truong, P. Hilse, S. Göde, A. Przystawik, T. Döppner, T. Fennel, T. Bornath, J. Tiggesbäumker, M. Schlages, G. Gerber, and K. H. Meiwes-Broer, “Optimal control of the strong-field ionization of silver clusters in helium droplets,” *Phys. Rev. A* **81**, 013201 (2010).

- [101] N. X. Truong, J. Tiggesbäumker, and T. Döppner, “Shaper-assisted removal of the direction-of-time ambiguity in second-harmonic generation frequency-resolved optical gating,” *Meas. Sci. Technol.* **21**, 085303 (2010).
- [102] A. Monmayrant, M. Joffre, T. Oksenhendler, R. Herzog, D. Kaplan, and P. Tournois, “Time-domain interferometry for direct electric-field reconstruction by use of an acousto-optic programmable filter and a two-photon detector,” *Opt. Lett.* **28**, 278–280 (2003).
- [103] L. Canova, X. Chen, A. Trisorio, A. Jullien, A. Assion, G. Tempea, N. Forget, T. Oksenhendler, and R. Lopez-Martens, “Carrier-envelope phase stabilization and control using a transmission grating compressor and an AOPDF,” *Opt. Lett.* **34**, 1333–1335 (2009).
- [104] T. Bäck, *Evolutionary algorithms in theory and practice: evolution strategies, evolutionary programming, genetic algorithms* (Oxford University Press, Oxford, 1996).
- [105] A. K. Hartmann and R. Heiko, *Optimization Algorithms in Physics* (Wiley, Berlin, 2002).
- [106] S. A. Rice and M. Zhao, *Optical Control of Molecular Dynamics* (Wiley, New York, 2000).
- [107] M. Shapiro and P. Brumer, *Principles of the Quantum Control of Molecular Processes* (Wiley, New York, 2003).
- [108] D. E. Goldberg, *Genetic algorithms in search, optimization, and machine learning* (Addison-Wesley Professional, New York, 1989).
- [109] J. H. Holland, *Adaptation in Natural and Artificial Systems: An Introductory Analysis with Applications to Biology, Control, and Artificial Intelligence* (MIT Press, Cambridge, 1992).
- [110] H. P. Schwefel, *Evolution and optimum seeking* (Wiley, New York, 1995).
- [111] N. X. Truong, P. Hilse, S. Göde, A. Przystawik, T. Döppner, T. Fennel, T. Bornath, J. Tiggesbäumker, M. Schlanges, G. Gerber, and K. H. Meiwes-Broer, “Optimal control of the strong-field ionization of silver clusters in helium droplets,” *Phys. Rev. A* **81**, 013201 (2010).
- [112] J. Tiggesbäumker, T. Fennel, N. X. Truong, and K.-H. Meiwes-Broer, “Resolving the ion and electron dynamics in finite systems exposed to intense optical laser fields,” in “Metal-to-Nonmetal Transitions,” vol. 132 of *Springer Series in Materials Science*, R. Redmer, F. Hensel, and B. Holst, eds. (Springer, Berlin, 2010), pp. 85–113.
- [113] H. Pohlheim, *Evolutionäre Algorithmen: Verfahren, Operatoren und Hinweise für die Praxis* (Springer, Berlin, 2000).
- [114] J. Zhou, J. Peatross, M. Murnane, and H. Kapteyn, “Enhanced high-harmonic generation using 25 fs laser pulses,” *Phys. Rev. Lett.* **76**, 752–755 (1996).

- [115] C. J. Bardeen, Q. Wang, and C. V. Shank, “Selective excitation of vibrational wave packet motion using chirped pulses,” *Phys. Rev. Lett.* **75**, 3410–3413 (1995).
- [116] T. Döppner, T. Diederich, A. Przystawik, N. X. Truong, T. Fennel, J. Tiggesbäumker, and K.-H. Meiwes-Broer, “Charging of metal clusters in helium droplets exposed to intense femtosecond laser pulses,” *Phys. Chem. Chem. Phys.* **9**, 4639–4652 (2007).
- [117] B. Seifert and H. Stolz, “A method for unique phase retrieval of ultrafast optical fields,” *Meas. Sci. Technol.* **20**, 015303 (2009).
- [118] M. E. Anderson, A. Monmayrant, S. P. Gorza, P. Wasylczyk, and I. A. Walmsley, “Spider: A decade of measuring ultrashort pulses,” *Laser Phys. Lett.* **5**, 259–266 (2008).
- [119] T. Feurer and R. Sauerbrey, *Characterization of Short Laser Pulses*, vol. 29C of *Experimental Methods in the Physical Sciences* (Academic Press, San Diego, 1996).
- [120] T. H. Maiman, “Stimulated Optical Radiation in Ruby,” *Nature* **187**, 493 (1960).
- [121] R. W. Boyd, *Nonlinear Optics* (Academic Press, San Diego, 2003).
- [122] S. J. Wawilow and W. L. Lewschin, “Die beziehungen zwischen fluoreszenz und phosphoreszenz in festen und flüssigen medien,” *Z. Phys.* **35**, 920–936 (1926).
- [123] P. A. Franken, A. E. Hill, C. W. Peters, and G. Weinreich, “Generation of optical harmonics,” *Phys. Rev. Lett.* **7**, 118–119 (1961).
- [124] N. X. Truong, “Setup and characterization of a high-dynamic range, third-order correlator for 1 kHz laser system,” Master’s thesis, Friedrich-Schiller-Universität Jena (2004).
- [125] S. Quian and D. Chen, *Joint time-frequency analysis; Methods and Applications* (Prentice Hall, New Jersey, 1996).
- [126] R. A. Altes, “Detection, estimation, and classification with spectrograms,” *J. Acoust. Soc. Am.* **67**, 1232–1246 (1980).
- [127] K. W. DeLong and R. Trebino, “Improved ultrashort pulse-retrieval algorithm for frequency-resolved optical gating,” *J. Opt. Soc. Am. B* **11**, 2429 (1994).
- [128] K. W. DeLong, R. Trebino, and W. E. White, “Simultaneous recovery of two ultrashort laser pulses from a single spectrogram,” *J. Opt. Soc. Am. B* **12**, 2463 (1995).
- [129] T. Brabec, *Strong field laser physics*, Springer Series in Optical Sciences (Springer, Berlin, 2008).
- [130] A. M. Weiner, *Ultrafast Optics*, Wiley Series in Pure and Applied Optics (Wiley, New Jersey, 2009).
- [131] A. E. Siegman, *Lasers* (University Science Books, California, 1986).

- [132] D. Kane, A. Taylor, R. Trebino, and K. DeLong, “Single-shot measurement of the intensity and phase of a femtosecond UV laser pulse with frequency-resolved optical gating,” *Opt. Lett.* **19**, 1061–1063 (1994).
- [133] E. Zeek, A. P. Shreenath, P. O’Shea, M. Kimmel, and R. Trebino, “Simultaneous automatic calibration and direction-of-time removal in frequency-resolved optical gating,” *Appl. Phys. B* **74**, S265–S271 (2002).
- [134] V. Lozovoy, I. Pastirk, and M. Dantus, “Multiphoton intrapulse interference. iv. ultrashort laser pulse spectral phase characterization and compensation,” *Opt. Lett.* **29**, 775–777 (2004).
- [135] V. V. Lozovoy, B. Xu, Y. Coello, and M. Dantus, “Direct measurement of spectral phase for ultrashort laser pulses,” *Opt. Express* **16**, 592–597 (2008).
- [136] A. Galler and T. Feurer, “Pulse shaper assisted short laser pulse characterization,” *Appl. Phys. B* **90**, 427–430 (2008).
- [137] B. von Vacano, T. Buckup, and M. Motzkus, “In situ broadband pulse compression for multiphoton microscopy using a shaper-assisted collinear spider,” *Opt. Lett.* **31**, 1154–1156 (2006).
- [138] H. Rabitz, M. Hsieh, and C. Rosenthal, “Quantum optimally controlled transition landscapes,” *Science* **303**, 1998–2001 (2004).
- [139] G. Vogt, P. Nuernberger, T. Brixner, and G. Gerber, “Femtosecond pump-shaped-dump quantum control of retinal isomerization in bacteriorhodopsin,” *Chem. Phys. Lett.* **433**, 211–215 (2006).
- [140] P. Nuernberger, G. Vogt, R. Selle, S. Fechner, T. Brixner, and G. Gerber, “Generation of shaped ultraviolet pulses at the third harmonic of titanium-sapphire femtosecond laser radiation,” *Appl. Phys. B* **88**, 519–526 (2007).
- [141] B. von Vacano and M. Motzkus, “Time-resolved two color single-beam CARS employing supercontinuum and femtosecond pulse shaping,” *Opt. Commun.* **264**, 488–493 (2006).
- [142] P. Marquetand, P. Nuernberger, G. Vogt, T. Brixner, and V. Engel, “Properties of wave packets deduced from quantum control fitness landscapes,” *EPL* **80**, 53001 (2007).
- [143] P. Marquetand, P. Nuernberger, T. Brixner, and V. Engel, “Molecular dump processes induced by chirped laser pulses,” *J. Chem. Phys.* **129**, 074303 (2008).
- [144] D. Wolpert, M. Schade, F. Langhojer, G. Gerber, and T. Brixner, “Quantum control of the photoinduced Wolff rearrangement of diazonaphthoquinone in the condensed phase,” *J. Phys. B* **41**, 074025 (2008).
- [145] M. Wollenhaupt, M. Krug, J. Koehler, T. Bayer, C. Sarpe-Tudoran, and T. Baumert, “Photoelectron angular distributions from strong-field coherent electronic excitation,” *Appl. Phys. B* **95**, 245–259 (2009).

- [146] V. Hommes, M. Miclea, and R. Hergenroeder, "Silicon surface morphology study after exposure to tailored femtosecond pulses," *Appl. Surf. Sci.* **252**, 7449–7460 (2006).
- [147] N. X. Truong, S. Göde, J. Tiggesbäumker, and K. H. Meiwes-Broer, "A study of the global chirp dependence on the interaction of intense colored double pulses with clusters," *Eur. Phys. J. D.* (2011, in press).
- [148] N. X. Truong, S. Göde, J. Tiggesbäumker, and K. H. Meiwes-Broer, "Systematically shaped laser pulses for intense laser-cluster studies," to be submitted.
- [149] N. X. Truong, S. Göde, J. Tiggesbäumker, and K. H. Meiwes-Broer, "Charge state bleaching in intense laser-cluster interactions," to be submitted.
- [150] P. Nuernberger, G. Vogt, T. Brixner, and G. Gerber, "Femtosecond pump - shaped dump - probe control of retinal in bacteriorhodopsin," in "Ultrafast Phenomena XV," vol. 88 of *Springer Series in Chemical Physics*, P. Corkum, D. M. Jonas, R. J. D. Miller, and A. M. Weiner, eds. (Springer, Berlin, 2007), pp. 459–461.
- [151] W. de Heer, "The physics of simple metal clusters: Experimental aspects and simple models," *Rev. Mod. Phys.* **65**, 611–676 (1993).
- [152] P. Milani and S. Iannotta, *Cluster Beam Synthesis of Nanostructured Materials* (Springer, Berlin, 1999).
- [153] H. Pauly, *Atom, Molecule and Cluster Beams 2* (Springer, Berlin, 2000).
- [154] B. Whaley and R. Miller, "Special topic: Helium nanodroplets: A novel medium for chemistry and physics," *J. Chem. Phys.* **115**, 10064 (2001).
- [155] S. Goyal, D. Schutt, and G. Scoles, "Vibrational spectroscopy of sulfur hexafluoride attached to helium clusters," *Phys. Rev. Lett.* **69**, 933–936 (1992).
- [156] A. Bartelt, J. Close, F. Federmann, N. Quaas, and J.-P. Toennies, "Cold metal clusters: Helium droplets as a nanoscale cryostat," *Phys. Rev. Lett.* **77**, 3525–3528 (1996).
- [157] J. Toennies and A. Vilesov, "Superfluid helium droplets: A uniquely cold nanomatrix for molecules and molecular complexes," *Angew. Chem., Int. Ed.* **43**, 2622–2648 (2004).
- [158] T. Diederich, "Spektroskopie an silber- und magnesiumclustern in heliumtropfen," Ph.D. thesis, Universität Rostock (2003).
- [159] P. Radcliffe, A. Przystawik, T. Diederich, T. Döppner, J. Tiggesbäumker, and K.-H. Meiwes-Broer, "Excited-state relaxation of Ag<sub>8</sub> clusters embedded in helium droplets," *Phys. Rev. Lett.* **92**, 173403 (2004).
- [160] T. Diederich, T. Döppner, T. Fennel, J. Tiggesbäumker, and K.-H. Meiwes-Broer, "Shell structure of magnesium and other divalent metal clusters," *Phys. Rev. A* **72**, 023203 (2005).

- [161] B. A. Mamyrin, D. V. S. V. I. Karataev, and V. A. Zagulin, “The mass-reflection, a new nonmagnetic time-of-flight mass spectrometer with high resolution,” *Rev. Sci. Instr.* **37**, 45 (1973).
- [162] P. Radcliffe, “The Ionization Dynamics of Silver Clusters after Exposure to Strong Laser Pulses,” Ph.D. thesis, Universität Rostock (2004).
- [163] T. Döppner, J. P. Müller, A. Przystawik, S. Göde, J. Tiggesbäumler, K. H. Meiwes-Broer, C. Varin, L. Ramunno, T. Brabec, and T. Fennel, “Step-like Intensity Threshold Behavior of Extreme Ionization in Laser-Driven Xenon Clusters,” *Phys. Rev. Lett.* **105**, 053401 (2010).
- [164] F. Stienkemeier and K. K. Lehmann, “Spectroscopy and dynamics in helium nanodroplets,” *J. Phys. B-At. Mol. Opt. Phys.* **39**, R127–R166 (2006).
- [165] J. H. Posthumus, ed., *Molecules and Clusters in Intense Laser Fields* (University Press, Cambridge, 2001).
- [166] U. Saalman, C. Siedschlag, and J. M. Rost, “Mechanisms of cluster ionization in strong laser pulses,” *J. Phys. B* **39**, R39 (2006).
- [167] T. Seidemann, M. Y. Ivanov, and P. B. Corkum, “Role of electron localization in intense-field molecular ionization,” *Phys. Rev. Lett.* **75**, 2819–22 (1995).
- [168] T. Zuo and A. Bandrauk, “Charge-resonance-enhanced ionization of diatomic molecular ions by intense lasers,” *Phys. Rev. A* **52**, R2511 (1995).
- [169] V. Vénier, R. Taïeb, and A. Maquet, “Atomic clusters submitted to an intense short laser pulse: A density-functional approach,” *Phys. Rev. A* **65**, 013202 (2001).
- [170] C. Siedschlag and J. Rost, “Electron Release of Rare-Gas Atomic Clusters under an Intense Laser Pulse,” *Phys. Rev. Lett.* **89**, 173401 (2002).
- [171] C. Jungreuthmayer, M. Geissler, J. Zanghellini, and T. Brabec, “Microscopic Analysis of Large-Cluster Explosion in Intense Laser Fields,” *Phys. Rev. Lett.* **92**, 133401 (2004).
- [172] I. Last and J. Jortner, “Quasiresonance ionization of large multicharged clusters in a strong laser field,” *Phys. Rev. A* **60**, 2215–2221 (1999).
- [173] C. Rose-Petruck, K. Schäfer, K. Wilson, and C. Barty, “Ultrafast electron dynamics and inner-shell ionization in laser driven clusters,” *Phys. Rev. A* **55**, 1182–1190 (1997).
- [174] M. Ammosov, N. Delone, and V. Krainov, “Tunnel ionization of complex atoms and atomic ions in electromagnetic fields,” *Sov. Phys. JETP* **64**, 1191 (1986).
- [175] W. Lotz, “Electron-Impact Ionization Cross-Sections and Ionization Rate Coefficients for Atoms and Ions from Hydrogen to Calcium,” *Z. Phys.* **216**, 241–7 (1968).
- [176] L. Landau and E. Lifshitz, *Electrodynamics of Continuous Media* (Pergamon, Oxford, 1984).

- [177] J. Jackson, *Klassische Elektrodynamik* (de Gruyter, Berlin, 1983).
- [178] J. Tiggesbäumker, L. Köller, H. Lutz, and K.-H. Meiwes-Broer, “Giant resonances in silver-cluster photofragmentation,” *Chem. Phys. Lett.* **190**, 42–47 (1992).
- [179] V. P. Silin, “Nonlinear high-frequency plasma conductivity,” *Sov. Phys. JETP* **20**, 1510–6 (1965).
- [180] F. Megi, M. Belkacem, M. Bouchene, E. Suraud, and G. Zwicknagel, “On the importance of damping phenomena in clusters irradiated by intense laser fields,” *J. Phys. B-At. Mol. Opt. Phys.* **36**, 273–282 (2003).
- [181] S. Micheau, H. Jouin, and B. Pons, “Modified nanoplasma model for laser-cluster interaction,” *Phys. Rev. A* **77**, 053201 (2008).
- [182] T. Bornath, P. Hilse, and M. Schlanges, “Interaction of Dense Nanoplasmas with Intense Laser Fields: Ionization Dynamics in Large Silver Clusters,” *Contrib. Plasma Phys.* **47**, 402 (2007).
- [183] J. Stewart and K. Pyatt, “Lowering of Ionization Potentials in Plasmas,” *Astrophys. J.* **144**, 1203 (1966).
- [184] U. Kreibig and M. Vollmer, *Optical properties of metal clusters*, no. 25 in Springer Series in Materials Science (Springer, Berlin, 1995).
- [185] P. M. Dinh, P. G. Reinhard, and E. Suraud, “Dynamics of clusters and molecules in contact with an environment,” *Phys. Rep.-Rev. Sec. Phys. Lett.* **485**, 43–107 (2010).
- [186] I. Last and J. Jortner, “Nuclear Fusion induced by Coulomb Explosion of Heteronuclear Clusters,” *Phys. Rev. Lett.* **87**, 33401 (2001).
- [187] M. Hohenberger, D. R. Symes, K. W. Madison, A. Sumeruk, G. Dyer, A. Edens, W. Grigsby, G. Hays, M. Teichmann, and T. Ditmire, “Dynamic acceleration effects in explosions of laser-irradiated heteronuclear clusters,” *Phys. Rev. Lett.* **95**, 195003 (2005).
- [188] J. Purnell, E. M. Snyder, S. Wei, and A. W. C. Jr., “Ultrafast laser-induced Coulomb explosion of clusters with high charge states,” *Chem. Phys. Lett.* **229**, 333–9 (1994).
- [189] E. M. Snyder, S. A. Buzza, and A. W. Castleman Jr., “Intense Field-Matter Interactions: Multiple Ionization of Clusters,” *Phys. Rev Lett.* **77**, 3347–50 (1996).
- [190] J. Jha, P. Sharma, V. Nataraju, R. Vatsa, D. Mathur, and M. Krishnamurthy, “Characterization of doping levels in heteronuclear, gas-phase, van der Waals clusters and their energy absorption from an intense optical field,” *Chem. Phys. Lett.* **430**, 26–31 (2006).
- [191] J. Jha and M. Krishnamurthy, “Hotter electron generation in doped clusters,” *J. Phys. B* **41** (2008).

- [192] T. Döppner and S. Teuber and Th. Diederich and Th. Fennel and P. Radcliffe and J. Tiggesbäumker and K.H. Meiwes-Broer, “Dynamics of Free and Embedded Lead Clusters in Intense Laser Fields,” *Eur. Phys. J. D.* **24**, 157–160 (2003).
- [193] C. Peltz and T. Fennel, “Resonant charging of Xe clusters in Helium nanodroplets under intense laser fields,” *Eur. Phys. J. D.* (2011, in press).
- [194] T. Döppner, S. Teuber, M. Schumacher, J. Tiggesbäumker, and K.-H. Meiwes-Broer, “Charging dynamics of metal clusters in intense laser fields,” *Appl. Phys. B* **71**, 357–360 (2000).
- [195] S. Teuber, T. Döppner, T. Fennel, J. Tiggesbäumker, and K. Meiwes-Broer, “Ionic recoil energies in the Coulomb explosion of metal clusters,” *Eur. Phys. J. D.* **16**, 59–64 (2001).
- [196] M. K. Jackson, G. R. Boyer, J. Paye, M. A. Franco, and A. Mysyrowicz, “Temporal diffraction by nonlinear interaction in optical fibers,” *Opt. Lett.* **17**, 1770–1772 (1992).
- [197] V. L. da Silva, Y. Silberberg, and J. P. Heritage, “Nonlinear pulse shaping and causality,” *Opt. Lett.* **18**, 580–582 (1993).
- [198] X. Liu, R. Wagner, A. Maksimchuk, E. Goodman, J. Workman, D. Umstadter, and A. Migus, “Nonlinear temporal diffraction and frequency shifts resulting from pulse shaping in chirped-pulse amplification systems,” *Opt. Lett.* **20**, 1163–1165 (1995).
- [199] S. Augst, D. Strickland, D. D. Meyerhofer, S. L. Chin, and J. H. Eberly, “Tunneling Ionization of Noble Gases in a High-Intensity Laser Field,” *Phys. Rev. Lett.* **63**, 2212–5 (1989).
- [200] M. Dammasch, M. Dorr, U. Eichmann, E. Lenz, and W. Sandner, “Relativistic laser-field-drift suppression of nonsequential multiple ionization,” *Phys. Rev. A* **64**, 061402 (2001).
- [201] E. R. Kieft, J. J. A. M. van der Mullen, G. M. W. Kroesen, and V. Banine, “Time-resolved pinhole camera imaging and extreme ultraviolet spectrometry on a hollow cathode discharge in xenon,” *Phys. Rev. E* **68**, 056403 (2003).
- [202] R. Menzel, *Photonics: Linear and Nonlinear Interactions of Laser Light and Matter* (Springer-Verlag, Berlin, 2007).
- [203] C. Rullière, ed., *Femtosecond Laser Pulses: Principles and Experiments*, Advanced Texts in Physics (Springer, New York, 2005).
- [204] P. F. Moulton, “Spectroscopic and laser characteristics of Ti:Al<sub>2</sub>O<sub>3</sub>,” *J. Opt. Soc. Am. B-Opt. Phys.* **3**, 125–133 (1986).
- [205] H. Kogelnik, C. Shank, A. Dienes, and E. Ippen, “Astigmatically compensated cavities for CW dye lasers,” *IEEE J. Quant. Electron.* **QE8**, 373 (1972).
- [206] F. X. Kärtner, U. Morgner, R. Ell, T. Schibli, J. G. Fujimoto, E. P. Ippen, V. Scheuer, G. Angelow, and T. Tschudi, “Ultrabroadband double-chirped mirror pairs for generation of octave spectra,” *J. Opt. Soc. Am. B* **18**, 882–885 (2001).



- [207] S. Rausch, T. Binhammer, A. Harth, J. Kim, R. Ell, F. X. Kärtner, and U. Morgner, “Controlled waveforms on the single-cycle scale from a femtosecond oscillator,” *Opt. Express* **16**, 9739–9745 (2008).
- [208] K. Yamane, Z. Zhang, K. Oka, R. Morita, M. Yamashita, and A. Suguro, “Optical pulse compression to 3.4 fs in the monocycle region by feedback phase compensation,” *Opt. Lett.* **28**, 2258–2260 (2003).
- [209] S. Rausch, T. Binhammer, A. Harth, F. X. Kaertner, and U. Morgner, “Few-cycle femtosecond field synthesizer,” *Opt. Express* **16**, 17410–17419 (2008).
- [210] J. Ye and S. T. Cundiff, eds., *Femtosecond optical frequency comb: principle, operation, and applications* (Springer Science + Business Media, Inc., New York, 2005).
- [211] T. Brabec and F. Krausz, “Intense few-cycle laser fields: Frontiers of nonlinear optics,” *Rev. Mod. Phys.* **72**, 545–592 (2000).
- [212] E. Hecht, *Optik* (Oldenbourg Verlag, München, 2002).
- [213] U. Morgner, “Ultrafast optics: Single-cycle pulse generation,” *Nat. Photonics* **4**, 14–15 (2010).
- [214] F. Schwabl, *Quantenmechanik* (Springer, Berlin, 1993).
- [215] R. L. Sutherland, *Handbook of Nonlinear Optics* (Marcel Dekker Inc., New York, 2003).
- [216] J. A. Armstrong, N. Bloembergen, J. Ducuing, and P. S. Pershan, “Interactions between light waves in a nonlinear dielectric,” *Phys. Rev.* **127**, 1918–1939 (1962).
- [217] Y. R. Shen, *The Principles of Nonlinear Optics* (John Wiley, New York, 1986).
- [218] S. A. Akhmanov, V. A. Vysloukh, and A. S. Chirkin, *Optics of Femtosecond Laser Pulses* (American Institute of Physics, New York, 1992).
- [219] J. E. Midwinter and J. Warner, “The effects of phase matching method and of uniaxial crystal symmetry on the polar distribution of second-order non-linear optical polarization,” *Brit. J. Appl. Phys.* **16**, 1135 (1965).
- [220] W. Knoechner, *Solid-State Laser Engineering* (Springer, Berlin, 1999).
- [221] F. X. Kärtner, ed., *Few-Cycle Laser Pulse Generation and Its Applications*, vol. 95 of *Topics in Applied Physics* (Springer-Verlag, Berlin, 2004).
- [222] F. Verluise, V. Laude, J. Huignard, P. Tournois, and A. Migus, “Arbitrary dispersion control of ultrashort optical pulses with acoustic waves,” *J. Opt. Soc. Am. B* **17**, 138–145 (2000).
- [223] T. Blickle, “Theory of Evolutionary Algorithms and Application to System Synthesis,” Ph.D. thesis, ETH Zürich (1997).
- [224] J. E. Baker, “Adaptive selection methods for genetic algorithms,” in “Proc. 1st Int. Conf. on Genetic Algorithms,” (L. Erlbaum Associates Inc., Hillsdale, 1985), pp. 101–111.

- 
- [225] X. Yu and M. Gen, *Introduction to Evolutionary Algorithms* (Springer, New York, 2010).
- [226] K. A. D. Jong, “An analysis of the behavior of a class of genetic adaptive systems,” Ph.D. thesis, University of Michigan (1975).
- [227] H. Mühlenbein and D. Schlierkamp-Voosen, “Predictive models for the breeder genetic algorithm i. continuous parameter optimization,” *Evol. Comput.* **1**, 25–49 (1993).
- [228] H.-P. Schwefel, *Numerical Optimization of Computer Models* (John Wiley & Sons, Inc., New York, 1981).
- [229] H.-P. Schwefel, *Numerische Optimierung von Computer-Modellen mittels der Evolutionsstrategie*, vol. 26 of *Interdisciplinary Systems Research* (Birkhäuser, Basel, 1977).

# Appendix A

## Publications

### A.1 Publications within the Thesis

#### A.1.1 Shaper-assisted removal of the direction-of-time ambiguity in second-harmonic generation frequency-resolved optical gating

Truong *et al.*, Meas. Sci. Technol. **21**:085303, 2010

#### A.1.2 Intense colored pulse trains: generation, characterization, and applications

Truong *et al.*, J. Opt. **12**:115201, 2010

#### A.1.3 Charging of metal clusters in helium droplets exposed to intense femtosecond laser pulses

Döppner *et al.*, Phys. Chem. Chem. Phys. **9**:4639, 2007

#### A.1.4 Resolving the Ion and Electron Dynamics in Finite Systems Exposed to Intense Optical Laser Fields

Tiggesbäumker *et al.*, Chapter in *Metal-to-Nonmetal Transitions*, Editor R. Redmer *et al.*, Springer Series in Materials Science **132**:85, 2010

#### A.1.5 Optimal control of the strong-field ionization of silver clusters in helium droplets

Truong *et al.*, Phys. Rev. A **81**:013201, 2010

#### A.1.6 Systematically Shaped Laser Pulses for Intense Laser-Cluster Studies

Truong *et al.*, to be submitted to J. Phys. B: At. Mol. Opt. Phys.

#### A.1.7 A Study of the Global Chirp Dependence on the Interaction of Intense Colored Double Pulses with Clusters

Truong *et al.*, Eur. Phys. J. D (in press), 2011

### A.1.8 Charge State Bleaching in Intense Laser–Cluster Interactions

Truong *et al.*, to be submitted to *New. J. Phys.*

## A.2 Surrounding Publications

### A.2.1 Thomson scattering from near-solid density plasmas using soft X-ray free electron lasers

Höll *et al.*, *High Energy Density Phys.* **3**:120, 2007

### A.2.2 Bremsstrahlung and line spectroscopy of warm dense aluminum plasma heated by xuv free-electron-laser radiation

Zastrau *et al.*, *Phys. Rev. E* **78**:066406, 2008

### A.2.3 Soft X-Ray Thomson Scattering in Warm Dense Matter at FLASH

Fäustlin *et al.*, Chapter in *Ultrafast Phenomena XVI*, Editor P. Corkum *et al.*, Springer Series in Chemical Physics **92**:241, 2009

### A.2.4 Soft X-ray scattering using FEL radiation for probing near-solid density plasmas at few electron volt temperatures

Toleikis *et al.*, *High Energy Density Phys.* **6**:15, 2010

## A.1 Publications within the Thesis

### A.1.1 Shaper-assisted removal of the direction-of-time ambiguity in second-harmonic generation frequency-resolved optical gating

N. X. Truong, J. Tiggesbäumker, T. Döppner

In *Meas. Sci. Technol.* **21**:085303, 2010

The author's contribution in this work is to perform the experiments, analyze the data, and co-write the manuscript.



### **A.1.2 Intense colored pulse trains: generation, characterization, and applications**

N. X. Truong, J. Tiggesbäumker, K. H. Meiwes-Broer

In *J. Opt.* **12**:115201, 2010

The author's contribution in this work is to perform the experiments, analyze the data, and co-write the manuscript.





### **A.1.3 Charging of metal clusters in helium droplets exposed to intense femtosecond laser pulses**

T. Döppner, Th. Diederich, A. Przystawik, N. X. Truong, Th. Fennel, J. Tiggesbäumker, K.-H. Meiwes-Broer

In *Phys. Chem. Chem. Phys.* **9**:4639, 2007

The author's contribution in this work is to perform the experiments on silver clusters, and co-write the manuscript.



#### A.1.4 Resolving the Ion and Electron Dynamics in Finite Systems Exposed to Intense Optical Laser Fields

J. Tiggesbäumker, T. Fennel, N. X. Truong, K.-H. Meiwes-Broer

In *Metal-to-Nonmetal Transitions*, Editor R. Redmer *et al.*, Springer Series in Materials Science **132**:85, 2010

The author's contribution in this work is to perform the optimal control experiments on silver clusters, and correct the manuscript.



### **A.1.5 Optimal control of the strong-field ionization of silver clusters in helium droplets**

N. X. Truong, P. Hilse, S. Göde, A. Przystawik, T. Döppner, Th. Fennel, Th. Bornath, J. Tiggesbäumker, M. Schlanges, G. Gerber, K. H. Meiwes-Broer

In *Phys. Rev. A* **81**:013201, 2010

The author's contribution in this work is to perform the optimal control experiments on silver clusters, analyze the data, and co-write the manuscript.



### **A.1.6 Systematically Shaped Laser Pulses for Intense Laser-Cluster Studies**

N. X. Truong, S. Göde, J. Tiggesbäumker, K. H. Meiwes-Broer

To be submitted to *J. Phys. B: At. Mol. Opt. Phys.*, 2011

The author's contribution in this work is to perform the optimal control experiments on xenon clusters, analyze the data, and co-write the manuscript.





### **A.1.7 A Study of the Global Chirp Dependence on the Interaction of Intense Colored Double Pulses with Clusters**

N. X. Truong, S. Göde, J. Tiggesbäumker, K. H. Meiwes-Broer

*Eur. Phys. J. D* (in press), 2011

The author's contribution in this work is to perform the optimal control experiments on xenon clusters, analyze the data, and co-write the manuscript.



### **A.1.8 Charge State Bleaching in Intense Laser-Cluster Interactions**

N. X. Truong, S. Göde, J. Tiggesbäumker, K. H. Meiwes-Broer

To be submitted to *New. J. Phys.*, 2011

The author's contribution in this work is to perform the optimal control experiments on xenon clusters, analyze the data, and co-write the manuscript.



## A.2 Surrounding Publications

The author's contribution in these papers is to perform the experiments with the infrared laser on helium and hydrogen droplet beams in Rostock, perform experiments with FLASH in Hamburg, and correct the manuscripts.

### A.2.1 Thomson scattering from near-solid density plasmas using soft X-ray free electron lasers

A. Höll, Th. Bornath, L. Cao, T. Döppner, S. Düsterer, E. Förster, C. Fortmann, S. H. Glenzer, G. Gregori, T. Laarmann, K.-H. Meiwes-Broer, A. Przystawik, P. Radcliffe, R. Redmer, H. Reinholz, G. Röpke, R. Thiele, J. Tiggesbäumker, S. Toleikis, N. X. Truong, T. Tschentscher, I. Uschmann, U. Zastra

In *High Energy Density Phys.* **3**:120, 2007



### **A.2.2 Bremsstrahlung and line spectroscopy of warm dense aluminum plasma heated by xuv free-electron-laser radiation**

U. Zastra, C. Fortmann, R. R. Fäustlin, L. F. Cao, T. Döppner, S. Düsterer, S. H. Glenzer, G. Gregori, T. Laarmann, H. J. Lee, A. Przystawik, P. Radcliffe, H. Reinholz, G. Röpke, R. Thiele, J. Tiggesbäumker, N. X. Truong, S. Toleikis, I. Uschmann, A. Wierling, T. Tschentscher, E. Förster, R. Redmer

In *Phys. Rev. E* **78**:066406, 2008





### **A.2.3 Soft X-Ray Thomson Scattering in Warm Dense Matter at FLASH**

R. R. Fäustlin, S. Toleikis, Th. Bornath, L. Cao, T. Döppner, S. Düsterer, E. Förster, C. Fortmann, S. H. Glenzer, S. Göde, G. Gregori, A. Höll, R. Irsig, T. Laarmann, H. J. Lee, K. H. Meiwes-Broer, A. Przystawik, P. Radcliffe, R. Redmer, H. Reinholz, G. Röpke, R. Thiele, J. Tiggesbäumker, N. X. Truong, I. Uschmann, U. Zastra, Th. Tschentscher

In *Ultrafast Phenomena XVI*, Editor P. Corkum *et al.*, Springer Series in Chemical Physics **92**:241, 2009



#### **A.2.4 Soft X-ray scattering using FEL radiation for probing near-solid density plasmas at few electron volt temperatures**

S. Toleikis, R. R. Fäustlin, L. Cao, T. Döppner, S. Düsterer, E. Förster, C. Fortmann, S. H. Glenzer, S. Göde, G. Gregori, R. Irsig, T. Laarmann, H. J. Lee, B. Li, J. Mithen, K. -H. Meiwes-Broer, A. Przystawik, P. Radcliffe, R. Redmer, F. Tavella, R. Thiele, J. Tiggesbäumker, N. X. Truong, I. Uschmann, U. Zastra, Th. Tschentscher

In *High Energy Density Phys.* **6**:15, 2010



# Appendix B

## Supporting Materials

### B.1 Generation of Ultrashort Laser Pulses

To generate optical pulses in the femtosecond regime, one needs (i) a bandwidth of more than 1 THz, (ii) a suitable active medium which is able to amplify this bandwidth, and (iii) a mechanism to couple all of the modes, termed as the mode-locking technique [202, 203]. To date, several different laser mode-locking techniques have been developed, but all have to provide two basic functions: forcing all the modes to be equally spaced and to have the same phase at one instant of time. Typically, these requirements can be achieved with help of either an external modulator (active mode-locking) or a saturable absorbing medium (passive mode-locking). However, in some kinds of laser materials, the modes may be able to lock themselves, partially or totally, in the active medium. One of the most common techniques for generating ultrashort laser pulses is the passive mode-locking of Ti:sapphire ( $\text{Ti:Al}_2\text{O}_3$ ) lasers based on the nonlinear Kerr effect (see Appendix B.3). In such a laser material, the optical waves with stronger peak intensities experience less losses, and thus will be selectively modified with respect to peak intensity.

Considered as the laser material with optimal properties, Ti:sapphire crystals produce gain stretching from 650 nm to over 1100 nm [204], what is equivalent to a bandwidth of about 200 THz and a shortest-possible pulse duration of  $\sim 4$  fs.<sup>1</sup> It also has a very high thermal conductivity, a relatively large emission cross section ( $\sim 3 \cdot 10^{-19}$  cm<sup>2</sup> at 800 nm), as well as a saturation flux density approaching 1 Jcm<sup>-2</sup>. Since the Kerr effect is instantaneous and independent on the stored energy density of the laser medium, it enables a totally new class of laser systems with ultrashort duration (sub-10 fs) and extremely high powers. While the mode-locking process can be described relatively easily in the frequency-domain [203], a truly successful, comprehensive, and quantitative theory for ultrashort lasers is still missing. Therefore, the generation of ultrashort laser pulses of Ti:sapphire will only qualitatively be discussed.

A typical cavity design of a Ti:sapphire fs oscillator using Kerr-lens mode-locking is shown in Fig. B.1 [203]. The laser crystal is located in the common focus of the two mirrors  $M_1$  and  $M_2$  in an Z-configuration to compensate for astigmatism [205]. The energy source is a continuous-wave (cw) laser, typically an argon-ion laser or a diode-pumped frequency-doubled Nd:YVO<sub>4</sub> laser. The dichroic mirror  $M_1$  is highly transparent at the wavelength of the pump laser ( $\sim 530$  nm) and highly reflects at about 800 nm, which is the central emission wavelength of Ti:sapphire-based lasers.

---

<sup>1</sup>For an assumed Gaussian envelope.

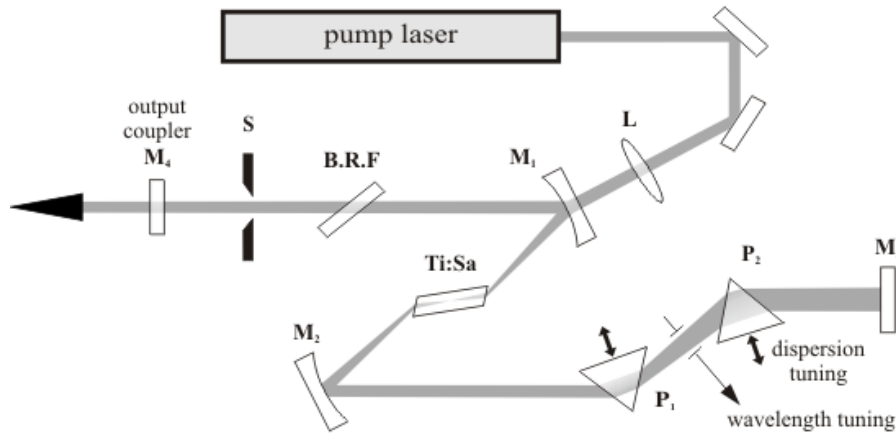


**Figure B.1:** Typical design of a Kerr-lens mode-locked Ti:sapphire femtosecond oscillator. Adapted from [203]

When passing through the crystal, optical waves with a Gaussian beam profile, for instance, feel an inhomogeneous refractive index due to the optical Kerr effect. The crystal behaves like a converging lens and focuses the laser beam. Therefore, the oscillator must be so designed that the losses are larger without the appearance of the Kerr-lens. This explains for the presence of the adjustable slit S (hard aperture) in the setup in Fig. B.1. Another approach is to adjust the cavity in such a way that the Kerr-lens effect in the crystal leads to a better overlap with the pump beams, thus an enhanced gain for high peak power pulses (soft aperture). The central wavelength of the laser system can be changed by turning the birefringent filter (B.R.F).

Because the Ti:sapphire crystal shows positive dispersion in the near infrared region, simple chirp compensation in the resonator is required, e.g., using a prism pair as shown in Fig. B.1. Specially designed dielectric mirrors, called chirp-compensating mirrors, have also been used for the compensation of linear and nonlinear dispersion. By such mirrors, the different wavelengths are effectively reflected at different depths and thus experience different optical delays in the sub- $\mu\text{m}$  range [206]. In addition, the refractive index of the active medium varies as a function of time, and thus causes the self-phase modulation (Appendix B.3). This effect broadens the laser spectrum and thereby introduces further possibility to shorten the pulse duration.

By using the compensation techniques discussed above, compact construction of fs laser oscillators with a pulse duration approaching the single-cycle limit ( $< 4$  fs) has been demonstrated [207, 208, 209]. In the frequency domain, such an ultrashort pulse provides an ultrabroadband mode-comb, which is useful for ultraprecise frequency metrology [210]. In the time domain, well-defined oscillations of the electric field within such pulses allow for the study of the dynamics in atoms, molecules and bulk in sub-femtosecond scales [211, 58].

## B.2 Ultrashort Laser Pulse Parameters

### Power, Energy and Intensity

We consider an ultrashort laser pulse  $E(t)$  propagating as a beam in a dispersionless material of refractive index  $n$ . The instantaneous pulse power or the flow of energy per

unit of time (in [W]) can be obtained from the Poynting theorem of electrodynamics [212]

$$\mathcal{P}(t) = \varepsilon_0 cn \int_A dS \frac{1}{T} \int_{t-T/2}^{t+T/2} E^2(t') dt', \quad (\text{B.1})$$

where  $\int_A dS$  is the integration over the beam cross section  $A$ .

To measure this quantity one needs a detector with the temporal response comparable to the speed of the variation of the field envelope to be measured. So far there is no such fast device available which can resolve the femtosecond laser pulses directly. From the experimental viewpoint the optical period  $T$  has to be replaced by the actual response time of the detector. *Pulse energy*  $\mathcal{W}$  (in [J]) is the integration of the power over time:

$$\mathcal{W} = \int_{-\infty}^{\infty} \mathcal{P}(t') dt'. \quad (\text{B.2})$$

Pulse power per unit area is the *temporal intensity*  $I(t)$  (in [ $\text{W cm}^{-2}$ ])

$$\begin{aligned} I(t) &= \varepsilon_0 cn \frac{1}{T} \int_{t-T/2}^{t+T/2} E^2(t') dt' \\ &= \frac{1}{2} \varepsilon_0 cn \mathcal{E}^2(t) = \frac{1}{2} \varepsilon_0 cn |\tilde{\mathcal{E}}(t)|^2, \end{aligned} \quad (\text{B.3})$$

and the energy density per unit area (in [ $\text{J cm}^{-2}$ ]):

$$W = \int_{-\infty}^{\infty} I(t') dt'. \quad (\text{B.4})$$

The *spectral intensity* of an ultrashort pulse is typically obtained by measuring the intensity of the laser field with a spectrometer and given as

$$S_\omega(\omega) = |\eta(\omega) \tilde{E}(\omega)|^2, \quad (\text{B.5})$$

where  $\eta$  is a scaling factor which accounts for losses, geometrical influences, and the finite resolution of the spectrometer. For an ideal spectrometer,  $|\eta|^2 = \varepsilon_0 cn / \pi$ , and the complete expression for the spectral intensity reads

$$\begin{aligned} S_\omega(\omega) &= \frac{\varepsilon_0 cn}{\pi} |\tilde{E}(\omega)|^2 \\ &= \frac{\varepsilon_0 cn}{4\pi} |\tilde{\mathcal{E}}(\omega - \omega_0)|^2, \end{aligned} \quad (\text{B.6})$$

where  $\tilde{\mathcal{E}}(\omega)$  is the spectral envelope function and defined as the complex Fourier transform of the complex field envelope  $\tilde{\mathcal{E}}(t)$ :

$$\tilde{\mathcal{E}}(\omega) = \int_{-\infty}^{\infty} \tilde{\mathcal{E}}(t) e^{-i\omega t} dt = 2 \int_{-\infty}^{\infty} \tilde{E}(t) e^{-i(\omega + \omega_0)t} dt. \quad (\text{B.7})$$

The spectrum vs. wavelength can be obtained by writing the spectral energy of the

corresponding pulse in both frequency and wavelength domains:

$$\int_{-\infty}^{\infty} S_{\lambda}(\lambda) d\lambda = \int_{-\infty}^{\infty} S_{\omega}(\omega) d\omega. \quad (\text{B.8})$$

By noting that  $\omega = 2\pi c/\lambda$  and thus  $d\omega = -(2\pi c/\lambda^2) d\lambda$ , we have:

$$S_{\lambda} = S_{\omega}(2\pi c/\lambda) \frac{2\pi c}{\lambda^2}. \quad (\text{B.9})$$

## Pulse Duration and Spectral Width

It is difficult to assert the detailed characteristics of a light pulse when its duration becomes shorter and shorter. Part of the problem is how to define the *pulse duration* and the *spectral width* so that they can deliver possibly exact information of the considered pulse. Especially, in the femtosecond regime, the shortest-generated laser pulses contain only a few (or even single) optical cycles [207, 213]. The standard statistical definitions are usually used in theoretic calculations and given as:

$$\tau_p^2 = \frac{\int_{-\infty}^{\infty} (t - t_p)^2 |\tilde{\mathcal{E}}(t)|^2 dt}{\int_{-\infty}^{\infty} |\tilde{\mathcal{E}}(t)|^2 dt} \quad (\text{B.10})$$

$$\Delta\omega_p^2 = \frac{\int_{-\infty}^{\infty} (\omega - \omega_0)^2 |\tilde{E}(\omega)|^2 d\omega}{\int_{-\infty}^{\infty} |\tilde{E}(\omega)|^2 d\omega}, \quad (\text{B.11})$$

where  $t_p$  is the intensity-weighted average time (defined similarly to the carrier frequency  $\omega_0$  in Eq. (2.5)). They can be used to ascertain whether the temporal (spectral) intensity is concentrated around the average time (frequency).

With help of the Schwarz's inequality [214], it can be shown that these quantities are related through the following universal inequality:

$$\Delta\omega_p^{(s)} \tau_p^{(s)} \geq \frac{1}{2}. \quad (\text{B.12})$$

The equality in Eq. (B.12) can only be reached with Gaussian temporal and spectral envelopes and the pulse is then said to be *Fourier-transform-limited* or unchirped. In this case, the instantaneous frequency  $\omega(t)$  (see, Eq. (2.7)) is independent of time.

However, in practice half-maximum quantities are easier to measure directly. One therefore defines the pulse duration  $\tau_p$  as the FWHM<sup>2</sup> of the intensity profile  $|\tilde{\mathcal{E}}(t)|^2$ , and the spectral width  $\Delta\omega_p$  as the FWHM of the spectral intensity  $|\tilde{\mathcal{E}}(\omega)|^2$ . The Fourier inequality is then usually given by:

$$\Delta\omega_p \tau_p = 2\pi \Delta\nu_p \tau_p \geq 2\pi c_B, \quad (\text{B.13})$$

where  $c_B$  is a numerical constant, depending on the assumed shape of the pulse. Table B.1 shows examples of some commonly cited pulse shapes. The equality holds for bandwidth-limited pulses which have no frequency modulation in the phase term  $\varphi(t)$  (see Eq. (2.7)).

---

<sup>2</sup>FWHM: Full Width at Half Maximum.



Shape	Intensity profile $I(t)$	$\tau_p$ FWHM	Spectral profile $S(\omega)$	$\Delta\omega_p$ FWHM	$c_B$	$\langle\tau_p\rangle\langle\Delta\omega_p\rangle$ MSQ
Gauss	$e^{-2(t/\tau_G)^2}$	$1.177\tau_G$	$e^{-(\frac{\omega\tau_G}{2})^2}$	$2.355/\tau_G$	0.441	0.5
Sech	$\text{sech}^2(t/\tau_S)$	$1.763\tau_S$	$\text{sech}^2\frac{\pi\omega\tau_S}{2}$	$1.122/\tau_S$	0.315	5.25
Lorentz	$[1 + (t/\tau_L)^2]^{-2}$	$1.287\tau_L$	$e^{-2 \omega \tau_L}$	$0.693/\tau_L$	0.142	0.7
Asym. sech	$[e^{t/\tau_a} + e^{-3t/\tau_a}]^{-2}$	$1.043\tau_a$	$\text{sech}\frac{\pi\omega\tau_a}{2}$	$1.677/\tau_a$	0.278	
Square	1 for $ t/\tau_r  \leq 1$ , 0 elsewhere	$\tau_r$	$\text{sinc}^2(\omega\tau_r)$	$2.78/\tau_r$	0.443	3.27

**Table B.1:** Essential characteristics of various standard pulse shapes.  $\langle\tau_p\rangle$  and  $\langle\Delta\omega_p\rangle$  are respectively the pulse duration and spectral width based on mean square deviations (MSQ). Adapted from [53]

### Example of a Gaussian Pulse

To illustrate how the key parameters can be derived from a given laser pulse shape, we consider a Gaussian pulse with a quadratic temporal phase

$$\tilde{\mathcal{E}}(t) = \mathcal{E}_0 e^{-(1+i\alpha)t^2/\tau_G^2}, \quad (\text{B.14})$$

with a duration (FWHM)

$$\tau_p = \sqrt{2 \ln 2} \tau_G. \quad (\text{B.15})$$

Calculated from (B.3), the temporal intensity has also Gaussian shape with a FWHM-width  $\tau_p/\sqrt{2}$ :

$$I(t) = \frac{1}{2} \varepsilon c n \mathcal{E}_0^2 e^{-2t^2/\tau_G^2}. \quad (\text{B.16})$$

The temporal phase is simply given as:

$$\varphi(t) = \alpha t^2/\tau_G^2, \quad (\text{B.17})$$

and thus the instantaneous frequency is

$$\omega(t) = \omega_0 - d\varphi(t)/dt = \omega_0 - 2\alpha t/\tau_G^2. \quad (\text{B.18})$$

As one can see from Eq. (B.18), the pulse is down-chirped for a positive chirp value of  $\alpha$  and vice versa. The Fourier transform of Eq. (B.14) yields:

$$\tilde{\mathcal{E}}(\omega) = \frac{\mathcal{E}_0 \sqrt{\pi} \tau_G}{\sqrt{1 + \alpha^2}} \exp \left\{ -i\Phi(\omega) - \frac{\omega^2 \tau_G^2}{4(1 + \alpha^2)} \right\}, \quad (\text{B.19})$$

where the spectral phase is a quadratic function of frequency:

$$\Phi(\omega) = \frac{1}{2} \arctan \alpha + (\phi_2/2) \omega^2 \quad \text{with } \phi_2 = \frac{-\alpha \tau_G^2}{2(1 + \alpha^2)}. \quad (\text{B.20})$$

The spectral intensity also has the Gaussian shape and reads:

$$S(\omega + \omega_0) = \frac{|\eta|^2 \pi \mathcal{E}_0^2 \tau_G^2}{\sqrt{1 + \alpha^2}} \exp \left\{ -\frac{\omega^2 \tau_G^2}{2(1 + \alpha^2)} \right\} \quad (\text{B.21})$$

with a FWHM-bandwidth:

$$\Delta\omega_p = (1/\tau_G)\sqrt{8\ln 2(1+\alpha^2)}. \quad (\text{B.22})$$

The pulse duration-bandwidth product is now given by:

$$\Delta\nu_p\tau_p = (\Delta\omega_p/2\pi)\tau_p = \frac{2\ln 2}{\pi}\sqrt{1+\alpha^2}. \quad (\text{B.23})$$

The presence of a linear chirp results in significant different delays between the different spectral components of laser pulse, leading to pulse broadening effect and a duration-bandwidth product exceeding the Fourier-limit ( $c_B = 2\ln 2/\pi \approx 0.441$ ) by a factor  $\sqrt{1+\alpha^2}$ . This conclusion holds also for the statistical definitions of pulse duration and bandwidth given by Eqs. (B.10) and (B.11):

$$\Delta\omega_p^{(s)}\Delta\tau_p^{(s)} = \frac{\sqrt{1+\alpha^2}}{2}. \quad (\text{B.24})$$

## B.3 Nonlinear Optics

### B.3.1 Wave Equations

The theoretical framework for the description and study of nonlinear optical phenomena remains the same as for other optical phenomena in general, i.e., the macroscopic Maxwell equations. In the absence of the sources of the fields, the Maxwell equations for an electromagnetic pulse propagating in an infinite medium are [177]

$$\nabla \times \tilde{\mathbf{E}} = -\frac{\partial \tilde{\mathbf{B}}}{\partial t} \quad (\text{B.25})$$

$$\nabla \times \tilde{\mathbf{H}} = \frac{\partial \tilde{\mathbf{D}}}{\partial t} \quad (\text{B.26})$$

$$\nabla \cdot \tilde{\mathbf{D}} = 0 \quad (\text{B.27})$$

$$\nabla \cdot \tilde{\mathbf{B}} = 0 \quad (\text{B.28})$$

and the material equations

$$\tilde{\mathbf{D}} = \epsilon_0\tilde{\mathbf{E}} + \tilde{\mathbf{P}} \quad (\text{B.29})$$

$$\tilde{\mathbf{B}} = \mu_0(\tilde{\mathbf{H}} + \tilde{\mathbf{M}}), \quad (\text{B.30})$$

where

$\tilde{\mathbf{E}}$ :	the electric field	$\tilde{\mathbf{H}}$ :	the magnetic field
$\tilde{\mathbf{D}}$ :	the electric displacement	$\tilde{\mathbf{B}}$ :	the magnetic induction
$\tilde{\mathbf{P}}$ :	the polarization vector	$\tilde{\mathbf{M}}$ :	the magnetization vector
$\epsilon_0$ :	the dielectric constant of vacuum	$\mu_0$ :	the permeability of vacuum.

The polarization vector  $\tilde{\mathbf{P}}$  describes the field-material interactions and generally depends upon the electric field  $\tilde{\mathbf{E}}$  as follows [121]:

$$\begin{aligned}\tilde{\mathbf{P}} = & \quad \epsilon_0 \underline{\chi}^{(1)} : \tilde{\mathbf{E}} && \text{the linear polarization} && \text{(B.31)} \\ & + \epsilon_0 \underline{\chi}^{(2)} : \tilde{\mathbf{E}}^2 && \text{the second-order nonlinear polarization} \\ & + \epsilon_0 \underline{\chi}^{(3)} : \tilde{\mathbf{E}}^3 && \text{the third-order nonlinear polarization} \\ & + \dots && \dots\end{aligned}$$

Here the  $i$ -order susceptibility  $\underline{\chi}^{(i)}$  are the  $(i+1)$ -order tensors determined by the symmetry properties of the nonlinear medium.

The optical medium is assumed to be nonmagnetic, so that

$$\tilde{\mathbf{B}} = \mu_0 \tilde{\mathbf{H}}. \quad \text{(B.32)}$$

Introducing the material Eqs. (B.29) and (B.32) into the Maxwell's equations, we obtain the wave equation

$$\nabla \times \nabla \times \tilde{\mathbf{E}} + \mu_0 \frac{\partial^2 \tilde{\mathbf{D}}}{\partial t^2} = 0. \quad \text{(B.33)}$$

The first term in Eq. (B.33) can be written as:

$$\nabla \times \nabla \times \tilde{\mathbf{E}} = \nabla(\nabla \cdot \tilde{\mathbf{E}}) - \nabla^2 \tilde{\mathbf{E}}. \quad \text{(B.34)}$$

For vanishing gradient in the dielectric constant and hence  $\nabla \cdot \tilde{\mathbf{E}} = 0$ , we have

$$\nabla \times \nabla \times \tilde{\mathbf{E}} = -\nabla^2 \tilde{\mathbf{E}}. \quad \text{(B.35)}$$

It is usually convenient to split  $\tilde{\mathbf{P}}$  into linear and nonlinear parts as

$$\tilde{\mathbf{P}} = \tilde{\mathbf{P}}^{(1)} + \tilde{\mathbf{P}}^{\text{NL}}, \quad \text{(B.36)}$$

and write

$$\tilde{\mathbf{D}} = \tilde{\mathbf{D}}^{(1)} + \tilde{\mathbf{P}}^{\text{NL}} \quad \text{with} \quad \tilde{\mathbf{D}}^{(1)} = \epsilon_0 \tilde{\mathbf{E}} + \tilde{\mathbf{P}}^{(1)}. \quad \text{(B.37)}$$

Here  $\tilde{\mathbf{P}}^{(1)}$  is the linear polarization vector, depending linearly upon the electric field  $\tilde{\mathbf{E}}$ . In terms of these quantities, the wave equation (B.33) becomes:

$$\nabla^2 \tilde{\mathbf{E}} - \mu_0 \frac{\partial^2 \tilde{\mathbf{D}}^{(1)}}{\partial t^2} = \mu_0 \frac{\partial^2 \tilde{\mathbf{P}}^{\text{NL}}}{\partial t^2}. \quad \text{(B.38)}$$

For dispersive media we must consider each frequency component of the wave separately. Therefore, we represent the electric field, the linear displacement, and the nonlinear polarization by their Fourier-transforms:

$$\tilde{\mathbf{E}}(t) = \frac{1}{2\pi} \int \tilde{\mathbf{E}}(\omega) e^{i\omega t} d\omega \quad \text{(B.39)}$$

$$\tilde{\mathbf{D}}^{(1)}(t) = \frac{1}{2\pi} \int \tilde{\mathbf{D}}^{(1)}(\omega) e^{i\omega t} d\omega \quad \text{(B.40)}$$

$$\tilde{\mathbf{P}}^{\text{NL}}(t) = \frac{1}{2\pi} \int \tilde{\mathbf{P}}^{\text{NL}}(\omega) e^{i\omega t} d\omega. \quad \text{(B.41)}$$

As well-known from classical electrodynamics [177], the linear displacement of a medium and the electric field are related by:

$$\tilde{\mathbf{D}}^{(1)}(\omega) = \epsilon_0 \epsilon^{(1)}(\omega) \tilde{\mathbf{E}}(\omega) \quad (\text{B.42})$$

Introducing the Eqs. (B.39)–(B.42) into the Eq. (B.38), we obtain the inhomogeneous Helmholtz wave equation in the frequency domain:

$$\nabla^2 \tilde{\mathbf{E}}(\omega) + \frac{\omega^2}{c^2} \epsilon^{(1)}(\omega) \tilde{\mathbf{E}}(\omega) = -\mu_0 \omega^2 \tilde{\mathbf{P}}^{\text{NL}}(\omega). \quad (\text{B.43})$$

For further simplicity, we assume the field to be linearly polarized and propagating in the  $z$ -direction as a plane wave. The wave equation now becomes:<sup>3</sup>

$$\left[ \frac{\partial^2}{\partial z^2} + \frac{\omega^2}{c^2} \epsilon^{(1)}(\omega) \right] \tilde{E}(\omega) = -\mu_0 \omega^2 \tilde{P}^{\text{NL}}(\omega) \quad (\text{B.44})$$

This is the fundamental equation in solving the problem of ultrashort pulse propagating in a dispersive medium. In a linear medium, phenomena such as absorption, dispersion, group velocity dispersion, and diffraction effects, etc., are concerned and have been detailed elsewhere [53, 124]. We now proceed to study in detail the *sum-frequency generation* (SFG) which is important to understand the second- and third-harmonic generation processes in the pulse characterization procedures (section 2.1.3), as well as in our recent reports [98, 101]. Typical third-order effects such as *Kerr-lens effect* and *self phase modulation* account for the self-focusing and spectral phase distortions of ultrashort pulses propagating in nonlinear media (e.g., in the air) and will be discussed briefly in appendix B.3.3.

## B.3.2 Second-order Susceptibility

### Sum-Frequency Generation

Considering the case of SFG in an isotropic lossless medium with a quadratic optical nonlinearity. The applied waves,  $E_1(z, t)$  and  $E_2(z, t)$ , are assumed to fall onto the nonlinear medium at normal incidence. Within the *slowly varying envelope approximation* (SVEA), the solution to the wave equation (B.38) has the form of

$$E_3(z, t) = A_3(z, t) e^{i(\omega_3 t - k_3 z)} + \text{c.c.}, \quad (\text{B.45})$$

where

$$k_3 = k_3(\omega_3) = \frac{n_3 \omega_3}{c}, \quad n_3 = \sqrt{\epsilon^{(1)}(\omega_3)}. \quad (\text{B.46})$$

Here  $A_3(z, t)$  satisfies the inequality of SVEA in space

$$\left| \frac{\partial^2 A_3}{\partial z^2} \right| \ll \left| k_3 \frac{\partial A_3}{\partial z} \right|, \quad (\text{B.47})$$

---

<sup>3</sup>For convenience, we are working in the scalar field approximation.

and time domain

$$\left| \frac{\partial^2 A_3}{\partial t^2} \right| \ll \left| \omega_3 \frac{\partial A_3}{\partial t} \right|. \quad (\text{B.48})$$

Similarly, we represent the nonlinear polarization and the incident waves as

$$\mathcal{P}_3^{\text{NL}}(z, t) = \mathcal{P}_3^{\text{NL}}(z, t)e^{i(\omega_3 t - k_3 z)} + \text{c.c.} \quad (\text{B.49})$$

$$E_j(z, t) = A_j(z, t)e^{i(\omega_j t - k_j z)} + \text{c.c.} \quad (j = 1, 2) \quad (\text{B.50})$$

and the amplitude of the nonlinear polarization [215]

$$\mathcal{P}_3^{\text{NL}} \equiv \mathcal{P}_3^{(2)} = 4\epsilon_0 d_{\text{eff}} A_1 A_2 e^{-i(k_1 + k_2)z}, \quad (\text{B.51})$$

where  $d_{\text{eff}}$  is the so-called effective  $d$ -coefficient, which depends on structure of the nonlinear medium and is tabulated elsewhere [215].

Introducing the Eqs. (B.45) through (B.51) into (B.38), we obtain the *coupled-amplitude equation* in the first-order approximation of dispersion theory

$$\frac{\partial A_3}{\partial z} + \frac{1}{u_3} \frac{\partial A_3}{\partial t} = \frac{2\omega_3 d_{\text{eff}}}{in_3 c} A_1 A_2 e^{-i\delta k z}, \quad (\text{B.52})$$

where  $u_3$  is the group velocity of the sum-frequency wave  $\omega_3$ , defined by [53]

$$\frac{1}{u_j} = \frac{\partial k}{\partial \omega} \Big|_{\omega_j} = \frac{n(\omega_j)}{c} + \frac{\omega_j}{c} \frac{\partial n}{\partial \omega} \Big|_{\omega_j} \quad (\text{with } j = 1, 2, 3), \quad (\text{B.53})$$

and  $\delta k = k_1 + k_2 - k_3$  is called the *wave vector mismatch*. When the variation of the  $\omega_1$  and  $\omega_2$  waves must also be taken into consideration, we can derive the analogous equations for each wave:

$$\frac{\partial A_1}{\partial z} + \frac{1}{u_1} \frac{\partial A_1}{\partial t} = \frac{2\omega_1 d_{\text{eff}}}{in_1 c} A_3 A_2^* e^{i\delta k z}, \quad (\text{B.54})$$

$$\frac{\partial A_2}{\partial z} + \frac{1}{u_2} \frac{\partial A_2}{\partial t} = \frac{2\omega_2 d_{\text{eff}}}{in_2 c} A_3 A_1^* e^{i\delta k z}. \quad (\text{B.55})$$

For monochromatic planar incident waves,<sup>4</sup> the time-derivative terms  $\partial A_j / \partial t$  (with  $j = 1, 2, 3$ ) in the coupled-amplitude equations vanish and the resulting equations can be solved exactly using the Jacobi elliptic function [216]. By assuming the applied waves to be undepleted by the nonlinear interaction, Boyd [121] has shown that the intensity of the sum-frequency wave is proportional to product of the input intensities

$$I_3 \sim I_1 I_2 L^2 \text{sinc}^2(\delta k L / 2), \quad (\text{B.56})$$

where  $I_j$  (with  $j = 1, 2$ ) are the intensity of the  $\omega_j$ -wave, respectively, and  $L$  is the distance of the nonlinear medium, over which the waves interact with each other. The intensity  $I_3$  reaches its maximum value  $I_3^{\text{max}}$  when  $\delta k = 0$  or also called the *perfect phase-matching* (PM) condition. A more detailed discussion of phase-matching will be given below in the section of conversion efficiency consideration.

For ultrashort laser pulses, an exact analytic solution to these equations is impossible.

<sup>4</sup>Also called the Infinite Plane Wave Approximation.

These short pulses have an appropriate spectral bandwidth and it is not possible to satisfy the phase-matching condition for all of the available spectral components within the spectrum. Here the group velocity mismatch comes into play and complicates the conversion processes. For simplicity, we will next consider the case of identical input waves or the second-harmonic generation, which is in many respects similar to the sum-frequency process. More discussions about SFG of ultrashort pulses can be found in [121, 215, 217] and the references therein.

## Second-Harmonic Generation

We now proceed to derive the coupled-amplitude equations for the second-harmonic (SH) process. The fundamental  $\omega$  and second-harmonic  $2\omega$  waves can also be represented as

$$E_1(z, t) = A_1(z, t)e^{i(\omega t - k_1 z)} + \text{c.c.} \quad (\text{B.57})$$

$$E_2(z, t) = A_2(z, t)e^{i(2\omega t - k_2 z)} + \text{c.c.} \quad (\text{B.58})$$

We then write the electric field in the medium as

$$\begin{aligned} E(z, t) &= E_1(z, t) + E_2(z, t) \\ &= A_1(z, t)e^{i(\omega t - k_1 z)} + A_2(z, t)e^{i(2\omega t - k_2 z)} + \text{c.c.}, \end{aligned} \quad (\text{B.59})$$

and the corresponding nonlinear polarization

$$\begin{aligned} P^{\text{NL}}(z, t) &= P_1^{\text{NL}}(z, t) + P_2^{\text{NL}}(z, t) \\ &= \mathcal{P}_1^{\text{NL}}(z, t)e^{i(\omega t - k_1 z)} + \mathcal{P}_2^{\text{NL}}(z, t)e^{i(2\omega t - k_2 z)} + \text{c.c.}, \end{aligned} \quad (\text{B.60})$$

where  $\mathcal{P}_j^{\text{NL}}$  (with  $j = 1, 2$ ) are given by [215]

$$\mathcal{P}_1^{\text{NL}} = 4\epsilon_0 d_{\text{eff}} A_2 A_1^* e^{i(k_1 - k_2)z} \quad (\text{B.61})$$

$$\mathcal{P}_2^{\text{NL}} = 2\epsilon_0 d_{\text{eff}} A_1^2 e^{-2ik_1 z}. \quad (\text{B.62})$$

Substituting Eqs. (B.59) and (B.60) into Eq. (B.38), we obtain the coupled-amplitude equations for SHG

$$\frac{\partial A_1}{\partial z} + \frac{1}{u_1} \frac{\partial A_1}{\partial t} = -i\gamma_1 A_2 A_1^* e^{i\delta k z} \quad (\text{B.63})$$

$$\frac{\partial A_2}{\partial z} + \frac{1}{u_2} \frac{\partial A_2}{\partial t} = -i\gamma_2 A_1^2 e^{-i\delta k z}, \quad (\text{B.64})$$

with the phase mismatch

$$\delta k = 2k_1 - k_2, \quad (\text{B.65})$$

and

$$\gamma_j = \frac{2\omega d_{\text{eff}}}{n_j c} \quad \text{with } j = 1, 2. \quad (\text{B.66})$$

**Group velocity matching.** We first consider the simplest case, where the phase-matching and group velocity matching conditions are simultaneously satisfied, i.e.,

$$\delta k = 0 \quad \text{and} \quad u = u_1 = u_2. \quad (\text{B.67})$$

For convenient reasons, we transfer to a coordinate system  $(\eta, \xi)$  moving with the group velocity  $u$ :

$$\xi = z, \quad \eta = t - \frac{z}{u}, \quad (\text{B.68})$$

and introduce the real amplitudes and phases  $A_j(\eta, \xi) = a_j(\eta, \xi)e^{i\varphi_j}$  (with  $j = 1, 2$ ). The solutions to set of Eqs. (B.63) and (B.64) are [218]

$$a_1(\eta, \xi) = a_{10}(\eta)\text{sech}[\gamma a_{10}(\eta)\xi], \quad (\text{B.69})$$

$$a_2(\eta, \xi) = a_{10}(\eta)\tanh[\gamma a_{10}(\eta)\xi], \quad (\text{B.70})$$

$$\varphi_1(\eta, \xi) = \varphi_{10}(\eta), \quad (\text{B.71})$$

$$\varphi_2(\eta, \xi) = 2\varphi_1(\eta) - \pi/2, \quad (\text{B.72})$$

where  $a_{10}(\eta) = a_1(\eta, 0)$  and  $\gamma = \gamma_1 = \gamma_2$ .

In the *undepleted-pump approximation* (UPA), the fundamental wave is assumed almost constant along the whole interaction length. The SH wave then becomes

$$a_2(\eta, \xi) = \gamma z a_{10}^2(\eta). \quad (\text{B.73})$$

Using Eq. (B.3), we have the appropriate intensity relation between the interacting waves:

$$I_2(t, z) = \frac{\gamma^2 z^2}{2\epsilon_0 c n_1} I_1^2\left(t - \frac{z}{u}\right) \quad (\text{B.74})$$

The intensity of the second-harmonic wave is *quadratically proportional* to that of the fundamental and to the interaction length, which makes the SHG a widely-used process for optical autocorrelation techniques. Further, this feature leads to shortening the second-harmonic pulse duration. For a fundamental Gaussian-shaped pulse  $a_{10}(\eta) = a_0 e^{-t^2/\tau_G^2}$  with pulse duration  $\tau_1 = \sqrt{2 \ln 2} \tau_G$ , the second-harmonic pulse duration is  $\tau_2 = \tau_1/\sqrt{2}$ .

**Group velocity mismatch.** In fact the group velocity matching condition is not always satisfied ( $u_1 \neq u_2$ ). Applying the undepleted-pump approximation for Eqs. (B.63) and (B.64), we obtain the solution for the second-harmonic [218]

$$A_2(t, z) = -i\gamma_2 \int_0^z A_{10}^2\left(t - z/u_2 + \Delta u^{-1}\xi\right) e^{i\delta k \xi} d\xi, \quad (\text{B.75})$$

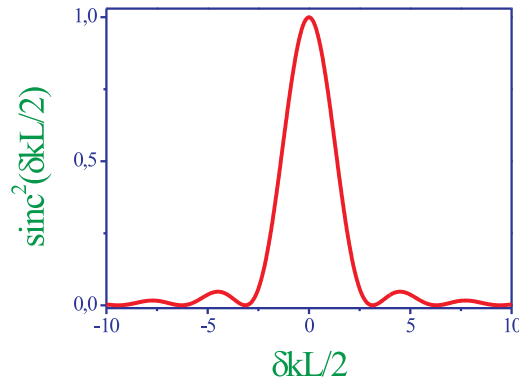
where

$$\Delta u^{-1} = \frac{1}{u_2} - \frac{1}{u_1} \quad (\text{B.76})$$

is termed as the group velocity mismatch and  $A_{10}(t) = A_1(t, 0)$ . For simplicity, we assume the fundamental amplitude is a Gaussian linearly chirped pulse

$$A_{10}(t) = a_0 e^{-(1+i\alpha)t^2/\tau_G^2}. \quad (\text{B.77})$$

**Figure B.2:** The effect of phase-mismatch on conversion efficiency of the SFG.



The SH intensity can be obtained from (B.75) for the case of perfect phase-matching,  $\delta k = 0$ ,

$$I_2(t, z) = \frac{\gamma_2^2 z^2}{2\epsilon_0 c n_1} I_1^2\left(t - \frac{z}{u_2}\right) \text{sinc}^2\left[\frac{\alpha z \Delta u^{-1}}{\tau_G^2} \left(t - \frac{z}{u_2}\right)\right]. \quad (\text{B.78})$$

For unchirped Gaussian pulses, i.e.,  $\alpha = 0$ , the SH intensity does not depend on the group mismatch  $\Delta u^{-1}$ . For strongly chirped pulses, due to the group velocity mismatch effect, the nonlinear medium acts as a spectral filter, whose bandwidth is reversely proportional to the group mismatch. Generally, the filter function depends on both the fundamental and SH frequencies.

### Conversion Efficiency in Second-Order Processes

**Phase-matching.** In relationship with the other aspects which are important for achieving high conversion efficiency, the phase-matching condition briefly discussed in the SFG-process (Appendix B.3.2) will be considered here in more details. The conversion efficiency of the SFG is defined from Eq. (B.56) as:

$$\Pi = \frac{I_3}{I_3^{\max}} = \text{sinc}^2(\delta k L / 2) \quad (\text{B.79})$$

where

$$\delta k = k_1 + k_2 - k_3 = \frac{1}{c} [n_1 \omega_1 + n_2 \omega_2 - n_3 \omega_3]. \quad (\text{B.80})$$

If  $\delta k = 0$ , i.e.,

$$n_1 \omega_1 + n_2 \omega_2 - n_3 \omega_3 = 0, \quad (\text{B.81})$$

the SFG-process is said to be perfect phase-matching and the conversion efficiency reaches its maximal value 1. When phase-mismatch occurs,  $\delta k \neq 0$ , the conversion efficiency decreases severely as seen in Fig. B.2. By replacing  $\omega_3 = \omega_1 + \omega_2$ , we obtain:

$$n_3 - n_2 = (n_1 - n_2) \frac{\omega_1}{\omega_3}. \quad (\text{B.82})$$

As shown by Boyd [121], in the normally dispersive materials the phase-matching condition is impossible because of the increase of the refractive index with frequency. One of the most commonly used techniques for achieving the phase-matching is *angle*



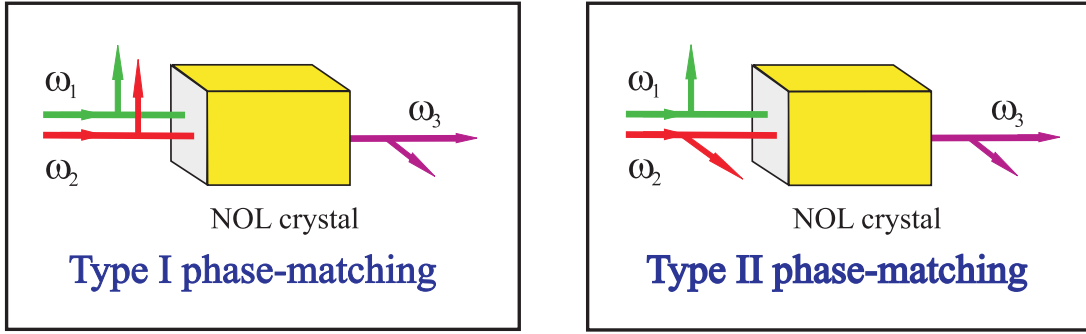


**Figure B.3:** Type I and II of phase-matching of the SFG process. The  $\omega_1$  and  $\omega_2$ -waves are the input waves, and  $\omega_3$ -wave is the generated sum-frequency wave ( $\omega_3 = \omega_1 + \omega_2$ ). The arrows indicate the polarization vectors of respective waves (NOL crystal:  $\chi^{(2)}$  crystals).

*tuning*, which exploits the birefringent property of nonlinear crystals. Birefringence is the dependence of the refractive index on the direction of polarization of the input wave. By tuning the angular orientation of the crystal with respect to the propagation direction of input waves, one can find the polarized direction of the highest-frequency  $\omega_3$  which provides the lower of the two possible refractive indices. There are two types of angle phase-matching [219] illustrated in figure B.3: (i) Type I phase-matching: the input waves have the same polarization. (ii) Type II phase-matching: the polarizations of the input waves are orthogonal.

For instance, **B**eta **B**arium **B**orate (BBO) crystal is a negative uniaxial crystal ( $n^e < n^o$ ). Therefore, the polarization direction of the  $\omega_3$  wave in the BBO crystal is in the extraordinary direction and the phase-matching equations for type I and II, respectively, are [121]:

$$n_3^e \omega_3 = n_1^o \omega_1 + n_2^o \omega_2 \quad (\text{Type I: } ooe) \quad (\text{B.83})$$

$$n_3^e \omega_3 = n_1^e \omega_1 + n_2^o \omega_2 \quad (\text{Type II: } eoe), \quad (\text{B.84})$$

where the indices  $o$  and  $e$  indicate the ordinary and extraordinary axes in the crystal, respectively. By each nonlinear crystal with certain polarization of the input waves, there is an optimum phase-matching angle  $\theta_m$  made of the propagation direction and the optical axis of the nonlinear crystal. For practical reasons, some useful angle phase-matching formulas for BBO crystal are given in table B.2.

**Crystal acceptance angle.** If the input wave propagates with an angle  $\theta$  deviating from the phase-matching angle  $\theta_m$ ,  $\delta k$  is different from zero leading to an inefficient harmonic generation. The angular sensitivity is determined by an acceptance angle  $\Delta\theta$  defined by the condition<sup>5</sup>

$$|\delta k L| = 2\pi, \quad (\text{B.85})$$

at which the  $\text{sinc}^2$ -function in Eq.(B.79) gets its first zero. For the case of SHG in a negative uniaxial crystal, the acceptance angle is given as [215]:

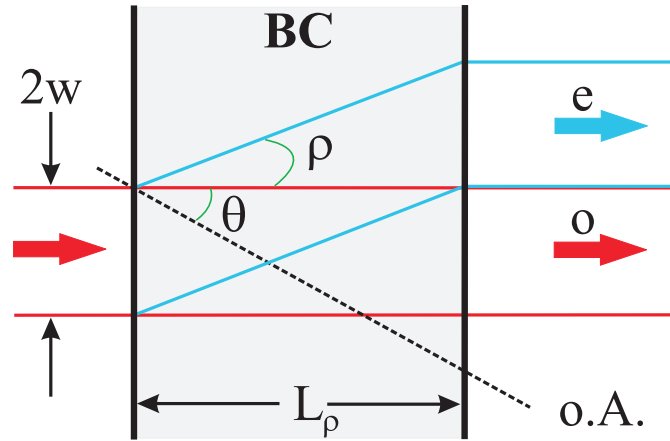
$$\Delta\theta = \frac{2(\lambda_\omega/L)}{(n_\omega^o)^2[(n_{2\omega}^e)^{-2} - (n_{2\omega}^o)^{-2}] \sin 2\theta_m}. \quad (\text{B.86})$$

<sup>5</sup>In some literatures, the acceptance angle is determined by the equation:  $|\delta k L| = \pi$ .

NL process	Phase-matching angle
SHG( <i>ooe</i> )	$\sin^2 \theta_m = \frac{(n_{2\omega}^e)^2}{(n_\omega^o)^2} \left[ \frac{(n_{2\omega}^o)^2 - (n_\omega^o)^2}{(n_{2\omega}^o)^2 - (n_{2\omega}^e)^2} \right]$
SFG( <i>oeo</i> )	$\frac{n_3^o}{\sqrt{1 + \left[ \frac{(n_3^o)^2}{(n_3^e)^2} - 1 \right] \sin^2 \theta_m}} - \frac{(\lambda_3/\lambda_1)n_1^o}{\sqrt{1 + \left[ \frac{(n_1^o)^2}{(n_1^e)^2} - 1 \right] \sin^2 \theta_m}} = (\lambda_3/\lambda_2)n_2^o$

**Table B.2:** The phase-matching angles of BBO crystals for the SHG (Type I) and SFG (Type II) processes [215].

**Figure B.4:** The spatial walk-off effect due to the double refraction in birefringent crystals (BC: birefringent crystal; o.A.: optical axis;  $w$ : beam radius;  $\theta = (\vec{k}, \text{o.A.})$ ).



**Walk-off.** Due to the birefringence of nonlinear crystals, the extraordinary wave  $n^e$  experiences Pointing vector walk-off (Fig. B.4). As the result, if the input laser beam size is small, the generated harmonic beam and the fundamental beam will be separated at a walk-off angle  $\rho$  in the crystal, causing low conversion efficiency. Therefore, the walk-off effect must be taken into account when one tries to decrease the beam size (e.g., by focusing the laser beam) to enhance the efficient conversion due to increase in intensity.

The walk-off angle for negative uniaxial crystals is given as [215]:

$$\tan \rho = \frac{[(n^o)^2 - (n^e)^2] \tan \theta}{(n^e)^2 + (n^o)^2 \tan^2 \theta}. \quad (\text{B.87})$$

The  $e$ - and  $o$ -beams become physically separated in a so-called *walk-off length*  $L_\rho$  given as:

$$L_\rho = \frac{2w}{\tan \rho}. \quad (\text{B.88})$$

For a BBO crystal with  $n^o = 1.69298$ ,  $n^e = 1.66051$ ,  $\theta_m = 29.2^\circ$  (phase matching angle-type I) at 400 nm central wavelength and 1 mm beam diameter, we have:

$$\rho = 16.7 \text{ mrad} \quad \text{and} \quad L_\rho = 6 \text{ cm}. \quad (\text{B.89})$$

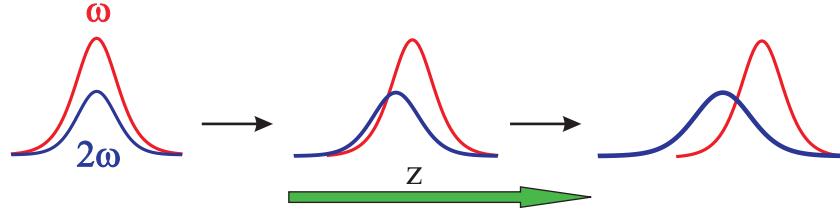


**Figure B.5:** The pulse broadening effect due to group velocity mismatch of the SGH process

**Group velocity mismatch.** Generally, the interacting pulses travel with different group velocities in nonlinear medium resulting in pulse broadening effect (Fig. B.5). Over a certain distance, they may no longer physically overlap and hence the conversion efficiency will dramatically be reduced.

To keep the efficient conversion without significant pulse broadening, it is recommended to use nonlinear crystals, whose thickness is less than a critical value  $L_c$  determined by

$$L_c \leq \frac{\tau_p}{\Delta u^{-1}}. \quad (\text{B.90})$$

For example for BBO:

$$\begin{aligned} 800 \text{ nm:} & \quad \frac{1}{u_1} = 56.09 \quad \text{ps/cm} \\ 400 \text{ nm:} & \quad \frac{1}{u_2} = 58.01 \quad \text{ps/cm} \\ & \quad \Delta u^{-1} = 1.92 \quad \text{ps/cm} \\ & \quad \tau_p = 30 \quad \text{fs} \\ \Rightarrow & \quad L_c \leq 150 \quad \mu\text{m}. \end{aligned} \quad (\text{B.91})$$

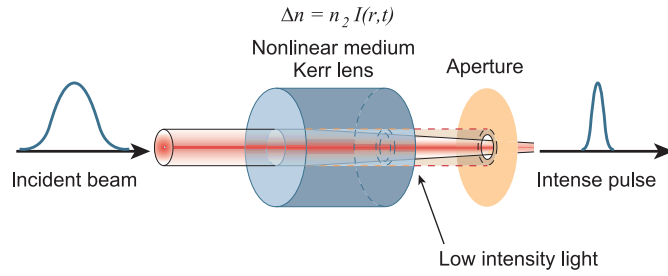
### B.3.3 Third-order Susceptibility

The third-order effects, which can be found in both centrosymmetric and noncentrosymmetric materials, are related to the third-order susceptibility term in the expression of the polarization vector (Eq. (B.31)). When an intense ultrashort laser pulse passes into an isotropic medium, the nonlinear refractive index can be written in a simple form

$$n = n_0 + n_2 I(\vec{r}, t), \quad (\text{B.92})$$

where  $n_0$  is the linear refractive index of the medium,  $n_2$  is the nonlinear index coefficient and usually given in  $[\text{cm}^2/\text{W}]$ . We will separately consider the effects caused by the spatial and temporal dependence of the laser intensity. The general treatments for ultrashort laser pulses are very complicated and beyond the scope of the present work. Detailed discussions can be found in, e.g., Refs. [61, 121, 218]. Here, for the sake of simplicity, we will investigate the propagation of a Gaussian laser beam in a third-order nonlinear material. The results however still hold for ultrashort laser pulses.

**Figure B.6:** Illustration of the Kerr-lens modelocking in fs oscillators. Only the intense pulse modes experience self-focusing, and thus low spatial losses through the hard aperture, and consequently contribute to the mode-locked operation. For further details, see Appendix B.1. Adapted from [39]



## Kerr-Lens Effect

The refractive index distribution in this case is

$$n(r) = n_0 + n_2 I(r), \quad \text{with} \quad I(r) = e^{-2r^2/w^2}. \quad (\text{B.93})$$

As seen from Eq. (B.93), for a positive  $n_2$ , the refractive index has a maximum value at the beam center  $r = 0$  and decreases with increasing  $r$ . After propagating over a distance  $e$  the beam has an optical path  $L(r) = n(r)e$ . To visualize the Kerr-lens effect the constant thickness  $e$  is replaced by a variable one such that its product with a constant refractive index remains the same optical path:

$$L(r) = n(r)e = e(r)n \quad (\text{B.94})$$

or

$$e(r) = \frac{en(r)}{n}. \quad (\text{B.95})$$

That means, the medium reacts as a Gaussian lens, which focuses the laser beam. This focusing process becomes stronger along the propagation because the focused beam increases the focal power of the dynamical lens. The increase of the focusing stops when the diameter is so small that the linear diffraction is large enough to balance the Kerr effect. This effect, also termed as *self-focusing*, is very important in understanding of the self-mode-locking, which occurs for instance in Ti:Al<sub>2</sub>O<sub>3</sub> femtosecond oscillators (see, Fig. B.6). If the path through the medium is sufficiently long, the beam will be focused to a small filament (beam collapse), and the medium will be usually damaged via avalanche ionization. The critical power level for Gaussian beam over which beam collapse will happen is given by [220]

$$P_{\text{cr}} = \frac{\kappa\lambda^2}{8\pi n_0 n_2}, \quad (\text{B.96})$$

where  $\kappa$  is a correction factor accounting for the severity of nonlinear phase distortion.<sup>6</sup>

## Self Phase Modulation

If the time-dependent laser intensity must be taken into account, we can write the refractive index in the form of

$$n(t) = n_0 + n_2 I(t), \quad \text{with} \quad I(t) = e^{-2t^2/\tau_G^2}. \quad (\text{B.97})$$

<sup>6</sup>The initial Gaussian profile is deformed during the self-focusing process.

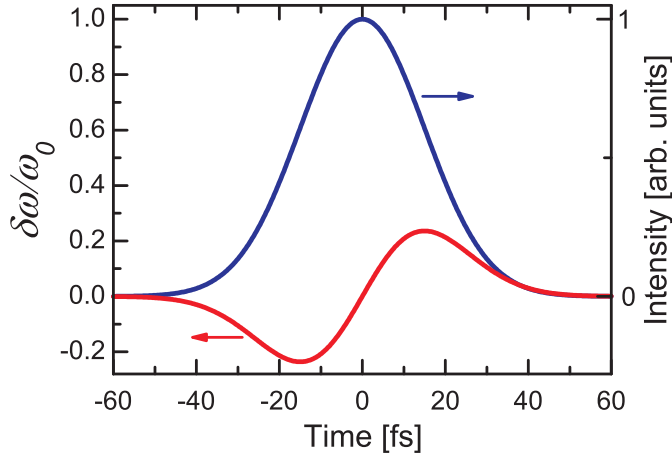


**Figure B.7:** Frequency variation vs. time as the result of self phase modulation for the case of  $n_2 > 0$ .

To study the influence of this time-varying index on the frequency of laser beam, we consider now a simple case of a plane wave propagating in the  $z$  direction of a nonlinear medium:

$$E(t, z) = A_0 e^{i(\omega_0 t - kz)}, \quad k = \frac{\omega_0 n(t)}{c}. \quad (\text{B.98})$$

The instantaneous frequency is

$$\omega(t) = \frac{\partial}{\partial t}(\omega_0 t - kz) = \omega_0 \left[ 1 - \frac{n_2 z}{c} \frac{\partial I(t)}{\partial t} \right] \quad (\text{B.99})$$

and the frequency variation

$$\delta\omega(t) = \omega(t) - \omega_0 = -\frac{n_2 \omega_0 z}{c} \frac{\partial I(t)}{\partial t}. \quad (\text{B.100})$$

With  $n_2 > 0$ , new low frequencies are created in the leading edge of the pulse envelope and new high frequencies are created in the trailing edge (Fig. B.7). These new frequencies are created inside the original pulse envelope, and therefore give rise to spectral broadening. Upon applying the SPM combined with optical compression techniques intense few-cycle laser pulses have been achieved [221].

A cumulative measure of the nonlinear interaction, e.g., in high-power lasers, due to  $n_2$  is given by the dimensionless  $B$ -integral [131]:

$$B = \frac{2\pi}{\lambda_{\text{las}}} \int n_2(z) I(z) dz, \quad (\text{B.101})$$

taking into account the changes in diameter and power of the laser beam through the whole system. Generally, the  $B$ -integral must be kept below  $\sim 3$  to avoid significant optical damage and distortions due to self-focusing or SPM.

## B.4 AOPDF: A Mathematical Approach

### B.4.1 Coupled-wave Analysis

The coupled wave equations for acousto-optic interactions in AOPDF can be derived using a similar approach for nonlinear optical processes (Appendix B.3). Here we will

follow Verluise *et al.* [222] to consider a frequency-modulated acoustic wave launched into a birefringent crystal along the  $z$  axis inducing a dielectric perturbation. Since the optical velocity much larger than the acoustic velocity the dielectric perturbation is nearly fixed and given as

$$\epsilon(z) = \epsilon + 2\epsilon_1(z) \cos[\psi(z)], \quad (\text{B.102})$$

with the acoustic phase described by

$$\psi(z) = \int_0^z K(z) dz. \quad (\text{B.103})$$

Here  $\epsilon$  denotes the unperturbed dielectric tensor,  $\epsilon_1(z)$  is the perturbed term of the dielectric tensor that leads to the coupling of the optical modes, and  $K(z)$  is the instantaneous spatial frequency of the acoustic wave. For simplicity,  $K(z)$  is assumed a monotonic function of  $z$ , i.e., it is either increasing or decreasing. Further,  $\epsilon_1(z)$  is usually much smaller than  $\epsilon$ , so that only its off-diagonal terms need to be taken into account.

The propagation of an ultrashort optical pulse  $\mathbf{E}(\omega, \mathbf{r})$  can be described through the wave equation [222]:

$$\frac{d^2}{dz^2} \mathbf{E}(\omega, \mathbf{r}) + \omega^2 \mu_0 \epsilon(z) \mathbf{E}(\omega, \mathbf{r}) = 0 \quad (\text{B.104})$$

Its general solution of the wave is given as the superposition of the plane waves of the two possible modes (mode 1 and 2):

$$\mathbf{E}(\omega, \mathbf{r}) = \sqrt{S(\omega)} \{A_1(z) \mathbf{e}_1 \exp[-ik_1(\omega)z] + A_2(z) \mathbf{e}_2 \exp[-ik_2(\omega)z]\}, \quad (\text{B.105})$$

where  $A_m(z)$  (with  $m = 1, 2$ ) are arbitrary but slowly varying functions of  $z$ ,  $k_m(\omega) = n_m(\omega)\omega/c$ , and where

$$\mathbf{e}_m = \left[ \frac{2\mu_0\omega}{k_m(\omega)} \right]^{1/2} \mathbf{p}_m. \quad (\text{B.106})$$

$\mathbf{p}_m$  ( $m = 1, 2$ ) are the orthogonal unit vectors representing the polarization of the optical waves along the ordinary and extraordinary axes, respectively.  $n_1 = n^o$  and  $n_2 = n^e$  are the corresponding refractive indices.  $\mathbf{e}_m$  is a normalized term which gives a power flow of  $1 \text{ W cm}^{-2}$  in the  $z$  direction [85], and  $S(\omega)$  is the spectral distribution of the optical pulse.

By inserting Eqs. (B.102) and (B.105) into Eq. (B.104) we have the following coupled-wave equations:

$$\frac{d}{dz} A_1(z) = -i\kappa(z) A_2(z) [e^{-i\phi_+(z)} + e^{-i\phi_-(z)}], \quad (\text{B.107})$$

$$\frac{d}{dz} A_2(z) = -i\kappa(z) A_1(z) [e^{i\phi_+(z)} + e^{i\phi_-(z)}], \quad (\text{B.108})$$

with

$$\phi_{\pm}(z) = [k_2(\omega) - k_1(\omega)]z \pm \psi(z), \quad (\text{B.109})$$

$$\kappa(z) = \frac{\omega^2 \mu_0}{2[k_1(\omega)k_2(\omega)]^{1/2}} \mathbf{p}_1 \cdot \epsilon_1(z) \cdot \mathbf{p}_2. \quad (\text{B.110})$$

The phase matching condition,

$$\frac{d}{dz}\phi_{\pm}(z) = 0, \quad (\text{B.111})$$

leads to the equation<sup>7</sup>

$$K(z(\omega)) = k_1(\omega) - k_2(\omega) = \frac{\omega}{c}[n_1(\omega) - n_2(\omega)]. \quad (\text{B.112})$$

From the monotonicity of  $K(z)$  as assumed above, for each optical frequency  $\omega$  there is only one position  $z(\omega)$  in the crystal in which energy transfer between the two modes happens significantly.

An exact solution to the coupled-wave equations (B.107) and (B.108) can be obtained by numerical simulation. But much insight can already be gained with some minor approximations. First, at the entrance of the crystal all energy is stored in mode 1, i.e.,  $A_1(0) = 1$  and  $A_2(0) = 0$  and the repartition occurs only in the vicinity of  $z(\omega)$  and then stays nearly unchanged. Second, in the vicinity of  $z(\omega)$  where the phase matching condition is fulfilled,  $\kappa(z)$  and  $\phi(z)$  remain almost constant. As shown in Ref. [85], the solution to Eqs. (B.107) and (B.108) can be then obtained analytically and reads as

$$A_2(z) \approx a(\omega)e^{i\phi[z(\omega)]}, \quad z > z(\omega), \quad (\text{B.113})$$

with  $|a(\omega)| < 1$ .

At the output of the position  $z = L$ , the spectral phase of mode 2 is given by three terms corresponding to (i) propagation on mode 1 for distance  $z(\omega)$ , (ii) interaction with the acoustic wave, and (iii) propagation on mode 2 for distance  $L - z(\omega)$ , respectively:

$$\varphi(\omega) = k_1(\omega)z(\omega) - \psi(z(\omega)) + k_2(\omega)[L - z(\omega)]. \quad (\text{B.114})$$

The derivative of the spectral phase  $\varphi(\omega)$  gives the group delay:

$$\tau(\omega) = \frac{dz(\omega)}{d\omega}\{k_1(\omega) - k_2(\omega) - K[z(\omega)]\} + \frac{dk_1(\omega)}{d\omega}z(\omega) + \frac{dk_2(\omega)}{d\omega}[L - z(\omega)]. \quad (\text{B.115})$$

The first term is vanished according to the phase-matching condition, see Eq. (B.112). With the group velocity defined by  $v_g = d\omega/dk(\omega)$  [53], the group delay becomes

$$\tau(\omega) = \frac{z(\omega)}{v_{g1}(\omega)} + \frac{L - z(\omega)}{v_{g2}(\omega)}. \quad (\text{B.116})$$

This equation illustrates a clear picture as discussed in the phenomenological approach (see section 2.1.2): For each optical frequency  $\omega$ , propagation occurs first at velocity  $v_{g1}(\omega)$  in mode 1 for distance  $z(\omega)$  and subsequently at velocity  $v_{g2}(\omega)$  in mode 2.

---

<sup>7</sup>Note that the choice of the sign in this equation depends on the sign of  $k_2 - k_1$ , i.e., on the sign of the optical anisotropy  $\Delta n = n^e - n^o$ . In our case, we consider only  $\phi(z) = \phi_+(z)$  corresponding to a negative sign.

### B.4.2 Group-Delay Control

Equation (B.116) can be rewritten as

$$z(\omega) = \Delta v_g(\omega) \left[ \tau(\omega) - \frac{L}{v_{g2}(\omega)} \right], \quad (\text{B.117})$$

where the differential group velocity between the two modes

$$\Delta v_g(\omega) = \left[ \frac{1}{v_{g1}(\omega)} - \frac{1}{v_{g2}(\omega)} \right]^{-1}. \quad (\text{B.118})$$

For a desired group-delay distribution, Eq. (B.116) defines the position of phase matching for every frequency. The phase-matching condition in Eq. (B.112) then specifies the form of the acoustic signal and can be rewritten as

$$K[z(\omega)] = \frac{\omega}{\Delta v_p(\omega)}, \quad (\text{B.119})$$

where  $\Delta v_p(\omega) = c/[n_2(\omega) - n_1(\omega)]$  is the differential phase velocity between the two modes. Eqs. (B.117) and (B.119) determine completely the form of the acoustic wave when an arbitrary group delay is given. The first step is to specify  $\tau(\omega)$  as a function of  $\omega$ , then to compute  $z(\omega)$  from Eq. (B.117), and finally to obtain  $K[z(\omega)]$  from Eq. (B.119).

For instance, in case of a linear chirp,  $\tau(\omega) = D\omega + \tau_0$ , with  $D$  being the group-delay dispersion ([fs<sup>2</sup>]) and  $\tau_0$  some constant delay time. The spatial frequency of the acoustic wave then becomes

$$K[z(\omega)] = \frac{1}{D\Delta v_p(\omega)} \left[ \frac{z(\omega)}{\Delta v_g(\omega)} + \frac{L}{v_{g2}(\omega)} - \tau_0 \right]. \quad (\text{B.120})$$

If the different velocities involved have constant values (usually the cases for small bandwidths) then the acoustic signal is also linearly chirped, with a slope given by  $(D\Delta v_p \Delta v_g)^{-1}$ .

### B.4.3 Amplitude-and-Phase Tailoring with AOPDF

The AOPDF performs for low values of acoustic power density as a convolution between the amplitude of the input optical wave form  $E_{\text{in}}(t)$  and a programmable acoustical signal  $S(t/\alpha)$ , where  $S(t)$  is proportional to the electrical signal applied to the piezoelectric transducer of the device,

$$E_{\text{out}}(t) = E_{\text{in}}(t) \otimes S(t/\alpha). \quad (\text{B.121})$$

The scaling factor

$$\alpha = \frac{V}{c} \Delta n \quad (\text{B.122})$$

is the ratio of the speed of sound to the speed of light multiplying with the optical anisotropy ( $\alpha \simeq 10^{-7}$  in TeO<sub>2</sub>). In the frequency domain,

$$E_{\text{out}}(\omega) = E_{\text{in}}(\omega) \cdot S(\alpha\omega). \quad (\text{B.123})$$

By generating a proper function  $S(t)$  one can achieve any arbitrary convolution with a temporal resolution given by the inverse of the available filter bandwidth. The following



parameters are crucial in dealing with an AOPDF.

- The maximum time window in which the pulse can be shaped corresponds to the difference of the complete propagations along the ordinary and extraordinary axis [91]

$$T_{\max} = \Delta n_g \cos^2(\theta_{\text{in}}) \frac{L}{c}, \quad (\text{B.124})$$

where  $L$  is the length of the crystal and  $\Delta n_g$  the group index difference.  $\theta_{\text{in}}$  is the angle between the incident wave vector and a reference crystallographic axis [89]. For instance, a 25 mm TeO<sub>2</sub> crystal gives  $T_{\max} \simeq 3$  ps at 800 nm [90] or a 72 mm KDP<sup>8</sup> crystal has  $T_{\max} \simeq 7$  ps at 300 nm [92].

- The spectral resolution is given as [91]

$$\delta\lambda = \frac{0.8}{\Delta n \cos^2(\theta_{\text{in}})} \frac{\lambda^2}{L}, \quad (\text{B.125})$$

where  $\theta_{\text{in}}$  is the angle between the incident wave vector and a reference crystallographic axis. The resolution is typically equal to 0.25 nm at 800 nm and down to 0.1 nm at 266 nm for commercially available devices.

- The number of controllable parameters  $N_{\text{cp}}$  is given by the number of resolution points in the programmed diffracted bandwidth. In the case of phase-only shaping, this bandwidth has to be broad enough to diffract all the optical components with a nearly constant amplitude. Experimentally, it is set to three times the optical bandwidth, i.e.,

$$N_{\text{cp}} = \frac{\Delta\lambda}{\delta\lambda} = \frac{\Delta n L}{0.8} \cos^2 \theta_{\text{in}} \frac{3\Delta\lambda}{\lambda^2}. \quad (\text{B.126})$$

For a 72 mm KDP crystal ( $\theta_{\text{in}} = 48.5^\circ$ ,  $\Delta n = 0.045$  and  $\Delta\lambda = 3$  nm at 410 nm), this gives  $N_{\text{cp}} \simeq 100$  and around 400 in the IR [91].

- The output light intensity relates to the incident light intensity and the actual acoustic power density  $P$  present in the interaction area through

$$I_{\text{out}}(\omega) = I_{\text{in}}(\omega) \cdot \frac{P}{P_0} \cdot \frac{\pi^2}{4} \cdot \text{sinc}^2 \left[ \frac{\pi}{2} \sqrt{\frac{P}{P_0} + \Delta\Phi^2} \right], \quad (\text{B.127})$$

where  $\Delta\Phi$  is an asynchronism factor dependent on the crystal length and the phase-mismatch,  $P_0$  denotes the acoustic power given by  $P_0 = 4.5 \times 10^6 (\lambda/L)^2$  in [W mm<sup>-2</sup>]. For  $P \ll P_0$ , the AOPDF response is linear with  $P$  and

$$I_{\text{out}}(\omega) = \frac{\pi^2}{2} \cdot \frac{P}{P_0} \cdot I_{\text{in}}(\omega). \quad (\text{B.128})$$

By increasing  $P \approx P_0$ , a higher diffraction efficiency can be achieved but the response of the AOPDF with  $P$  is not anymore linear.

---

<sup>8</sup>Potassium dihydrogen phosphate KH<sub>2</sub>PO<sub>4</sub>.

## B.5 Evolutionary Operators

### B.5.1 Selection

Selection is a process which imitates natural selection by giving *fitter* individuals higher opportunity for reproduction or survival in an evolutionary algorithm (parent- or survivor selection). It is usually inserted right after the initialization step.

**Fitness-Proportional Selection** was first proposed by Holland [109], also called *roulette wheel selection* [108]. Within this concept, an individual with the highest fitness has the greatest probability of being selected while the individual with the lowest fitness has the lowest probability of mating. The expected value of an individual, i.e., the expected number of times an individual will be selected to reproduce, is that individual's fitness divided by the average fitness of the population. If  $f_i$  is the fitness of individual  $i$  in the population, the selection probability  $p_i$  is defined according to

$$p_i = \frac{f_i}{\sum_{i=1}^N f_i}. \quad (\text{B.129})$$

A major drawback of fitness-proportionate selection is that it strongly depends on the scaling of the fitness function [223], i.e., the evolution rate relies very much on the variance of the fitness's in the population. Typically, early in the search the fitness variance in the population is large and a few *bad* individuals<sup>9</sup> are much fitter than the others. Under proportional selection they will produce several offsprings and thus will quickly broaden in the population. Later in the search, when all individuals in the population are very similar (low fitness variance), there are no real fitness differences for selection to exploit. Consequently, this hinders the EA from doing any further exploration and possibly runs into local optimum. This procedure is known as *premature convergence* and is a result of early putting too much selection pressure on highly fit individuals. The fitness-proportional selection is presented here just for a complete description, but will not be used in our EA program.

**Rank-based Selection** uses the rank of the fitness, rather than the absolute fitness, of the individuals in the current population to determine the probability of selection. Ranking is to sort the individuals based on their fitness first and then use their ranks to grant the selection probability. Under rank-based selection every individual obtains its fitness from ranking: The worst has fitness 1 and the best has fitness  $N$ . Ranking therefore results in a slow convergence, but avoids the "premature convergence" which usually happens in the fitness-proportional selection. It keeps up the selection pressure when the fitness variance is low and reduces the selection pressure when the fitness variance is high. It preserves diversity and thus leads to a successful search.

We introduce two fitness assignment methods:

- *Linear ranking*

Selection probability of each individual is proportional to its rank in the population [224]. The fitness value of individual  $i$  is determined according to

$$\text{Fitness}(i) = 2 - SP + 2 \cdot (SP - 1) \cdot \frac{i - 1}{N - 1}, \quad (\text{B.130})$$

---

<sup>9</sup>They are bad only when compared to the optimal solution.

where  $SP$  is the selection pressure possible in the range [1.0, 2.0].

- *Nonlinear ranking*

The method allows a higher selection pressure than what possible under the linear ranking method. Here selection probabilities are also based on each individual's rank but not proportional to the rank [113].

$$\text{Fitness}(i) = \frac{N \cdot X^{i-1}}{\sum_{i=1}^N X^{i-1}}. \quad (\text{B.131})$$

$X$  can be calculated as the solution to the following polynomial function:

$$0 = (SP - 1) \cdot X^{N-1} + SP \cdot X^{N-2} + \dots + SP \cdot X + SP, \quad (\text{B.132})$$

where selection pressure  $SP$  is possible in the range [1, N-2]. Generally, under nonlinear ranking the worst individuals obtain a somewhat higher fitness than under linear ranking with the same selection pressure. For a detailed description about different fitness-scaling methods see [113, 225].

**Elitism** was introduced by De Jong in 1975 [226] to ensure the survival of the found optimum during the optimization search. Some of the *best* individuals are retained at each generation in another memory place. Such individuals can be lost if they are not selected to reproduce or destroyed through crossover or mutation. After a new population is created, check whether *best* is in the population. If not, replace any individual in the population with the *best*. It has been proven that elitism significantly improves the performance, e.g., the search speed, of EAs.

**Tournament Selection:** Rank scaling requires sorting the entire population by rank, and therefore it is a potentially time-consuming procedure. Similar to rank-based selection in terms of selection pressure, but *tournament selection* is more efficient and more amenable to parallel computing. Under tournament selection a group of  $N_t$  (tournament size) individuals is randomly chosen from the population and performs a "tournament". The best individual with the highest fitness is usually chosen through a *stochastic* selection. The winner is inserted into the mating pool and the process is repeated until the mating pool for generating new offsprings is filled. Usually, tournament selection can be held between two individuals (binary tournament). But in general  $N_t$  can take any integer value between 1 and  $N$ .

**Truncation Selection** (also known as threshold selection) is one of the most strongest (most elitist) approaches of selection in that only a fraction  $T$  fittest individuals are selected from the population and they are equally likely to be used. The others are removed, and thus have no chance to produce offspring. Similar to tournament selection, here only the rank of an individual in the population is used for selection, not the absolute fitness value. Truncation selection is usually used in breeder genetic algorithms [227] and considered to be very similar to the  $(\mu, \lambda)$ -strategy in Evolution Strategy [228]. According to Ref. [227],  $T$  should be chosen in the range [0.1, 0.5].

**$(\mu + \lambda)$ - and  $(\mu, \lambda)$ -Selection** are completely *deterministic* rank-based methods, first introduced to evolution strategies by Schwefel [229]. The  $(\mu + \lambda)$ -selection selects the best  $\mu$  individuals out of the union of parents and offsprings to form the next parent generation while the  $(\mu, \lambda)$  chooses the  $\mu$  best individuals out of the offsprings only. The former seems to be more effective in terms of ensuring the survival of the best individuals (elitism),

which might lead the search to local optima. On the contrary, by limiting lifetimes of individuals to only one generation, the latter is able of leaving local optimum.  $(\mu + \lambda)$ -selection prevents the self-adaptation mechanism with respect to strategy parameters to work effectively. In case of changing environment the former preserves (outdated) solutions and is not able to follow the *moving optimum*. The ratio  $\mu/\lambda$  provides the basic parameterization instrument for controlling the character of the search. Decreasing  $\mu$  emphasizes on path-oriented search and convergence velocity while increasing  $\mu$  leads to a more volume-oriented search.

## B.5.2 Recombination

*Recombination* is the process of creating an offspring from two or more selected parent-individuals. It is sometimes distinguished from *crossover* based on how the variables are treated. The mixing of the variables is called recombination and the mixing of the values of a variable is termed as crossover. For simplicity, we use string-representation to describe individuals in the population. Three different recombination operators, which have been used successfully in genetic algorithms and evolution strategies, are presented as follows.

**Discrete Recombination** creates corners of a hypercube defined by the components of the parents ( $x$  and  $y$ ). Let  $x = (x_1, x_2, \dots, x_{\text{Nvar}})$  and  $y = (y_1, y_2, \dots, y_{\text{Nvar}})$  be the parent strings with the number of variables  $\text{Nvar}$ . Then the variables of the offspring  $z = (z_1, z_2, \dots, z_{\text{Nvar}})$  are determined through

$$\begin{aligned} z_i &= x_i \cdot a_i + y_i \cdot (1 - a_i) & i \in (1, 2, \dots, \text{Nvar}), \\ a_i &\in \{0, 1\} \text{ with probability } 0.5 \\ a_i &\text{ is renewed for each } i. \end{aligned} \tag{B.133}$$

**Extended Intermediate Recombination** can generate any point within a slightly larger hypercube.

$$\begin{aligned} z_i &= x_i \cdot a_i + y_i \cdot (1 - a_i) & i \in (1, 2, \dots, \text{Nvar}), \\ a_i &\text{ is chosen uniform randomly in the interval } [-0.25, 1.25] \\ a_i &\text{ is renewed for each } i. \end{aligned} \tag{B.134}$$

**Extended Line Recombination** produces a point in the line defined by  $x$  and  $y$ . The new point may lie outside  $[x_i, y_i]$ .

$$\begin{aligned} z_i &= x_i \cdot a + y_i \cdot (1 - a) & i \in (1, 2, \dots, \text{Nvar}), \\ a &\text{ is chosen uniform randomly in the interval } [-0.25, 1.25]. \end{aligned} \tag{B.135}$$

## B.5.3 Crossover

Crossover is recombination with individuals represented by *binary* strings. After selection (reproduction) the population is enriched with better individuals. The new individuals are first generated through crossover by proceeding in three steps: (i) randomly select a pair of individual strings for mating, (ii) randomly select a cross-site along the string length, and (iii) swap the position values between the two strings following the cross-site.

**Single-point crossover** is used by the traditional genetic algorithms. A cross-point is selected randomly along the length of the mated strings and bits next to the cross-points are exchanged to form children. With single-point crossover the head and the tail of a string (an individual) cannot be passed together to the offspring. Therefore multi-point crossover is necessary.

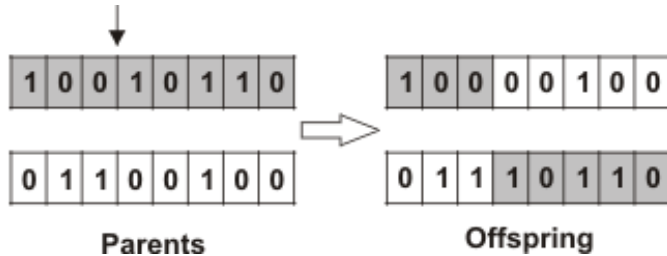


Figure B.8: Single-point crossover.

**Multi-point crossover** randomly distributes a number of chosen cross-points along the string length. Then the variables between successive cross-sites are exchanged between the two parent-strings to create two new offspring, keeping the first section (between the first variable and the first cross-point) of the both parent-strings fixed.

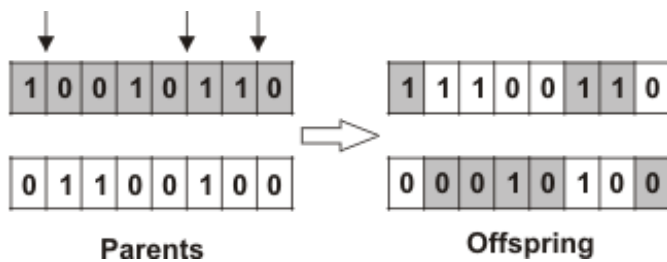


Figure B.9: Multi-point crossover.

**Uniform crossover** is quite different from the multi-point crossover. A binary *crossover mask* of the same length as the individuals is randomly generated. On producing child 1, where there is a 1 in the crossover mask, the gene is copied from the first parent-string, and where there is a 0 in the mask the gene is copied from the second parent-string. On producing child 2, where there is a 1 in the mask, the gene is copied from parent 2, else from parent 1. A new crossover mask is randomly for each pair of parent. An example with a random mask (1, 0, 1, 0, 0, 1, 1, 0) is illustrated in Fig. B.10.

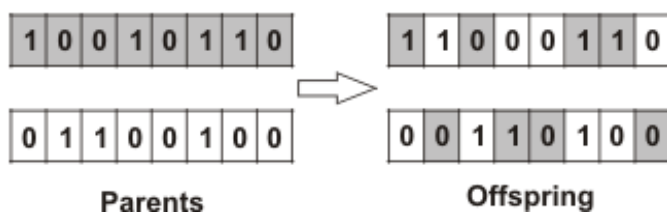


Figure B.10: Uniform crossover.

**Shuffle crossover** is related to uniform crossover. Before crossover, the variables are randomly shuffled in both parents. A single-point crossover is then performed. After recombination, the variables in the offspring are unshuffled. This avoids the positional bias since the variables are randomly reassigned each time crossover is applied.

### B.5.4 Mutation

After crossover the individuals are subjected to mutation. Mutation prevents the algorithm to be trapped in a local optimum. If crossover is supposed to exploit the current solution to find better ones, mutation is supposed to help for the exploration of the whole search space. Mutation is viewed as a background operator to maintain genetic diversity in the population. It introduces new genetic structures in the population by randomly modifying some of its building blocks. If there is no mutation, offsprings are generated immediately after crossover (or directly copied) without any change. An important parameter in the mutation technique is the *mutation probability*. If mutation probability 100%, whole chromosome (string) is changed, if it is 0%, nothing is changed. Though supposed to prevent the EA from falling into local extremes, mutation should not occur very often, because then EA will in fact change to random search.

There are several forms of mutation for different kinds of representation. For binary representation, a simple mutation can consist in inverting the value of each gene with a small probability. The probability is usually taken about  $1/L$ , where  $L$  is the length of the string.

**Flipping:** Mutation of a bit involves flipping a bit, changing 0 to 1 and vice versa.

**Interchanging:** Two random positions of the string are chosen and the bits corresponding to those positions are interchanged.

**Reversing:** A random position is chosen and the bits next to that position are reversed and a child string is produced.

**Breeder Genetic Algorithm (BGA) Mutation [227]:** A variable  $x_i$  is selected with probability  $p_m$  for mutation. Typically, the BGA uses  $p_m = 1/Nvar$  that is at least one variable will be mutated. BGA mutation occurs by modifying the selected variable with a value chosen within an interval  $[-range_i, range_i]$ .  $range_i$  defines the mutation range and is usually set to  $0.1 \cdot searchinterval_i$ , with  $searchinterval_i$  to be the search domain of variable  $x_i$ . The new value  $z_i$  is computed according to

$$z_i = x_i \pm range_i \cdot \delta. \quad (\text{B.136})$$

The  $+$  or  $-$  sign is chosen with probability 0.5.  $\delta$  is computed from a distribution which prefers small values:

$$\delta = \sum_{k=0}^{15} \alpha_k 2^{-k} \quad \text{with } \alpha_k \in \{0, 1\} \quad (\text{B.137})$$

Before mutation we set  $\alpha_k = 0$ . Then each  $\alpha_k$  is mutated to 1 with probability  $1/16$ . Only  $\alpha_k = 1$  contributes to the sum. On average there will be just one  $\alpha_k$  with value 1, say  $\alpha_j$ . Then  $\delta$  is given by

$$\delta = 2^{-j}. \quad (\text{B.138})$$

The standard BGA mutation operator is able to generate any point in the hypercube with center  $x$  defined by  $x_i \pm range_i$ . But it tests more often in the neighborhood of  $x$ . In the above standard setting, the mutation operator is able to locate the optimal  $x_i$  up to a precision of  $range_i \cdot 2^{-15}$ .

# List of Publications

## A Refereed Articles and Book Chapters

- **Control of chirped pulse trains: A *speedway* for free-optimization experiments**  
N. X. Truong, J. Tiggesbäumker, and K. H. Meiwes-Broer, submitted to *Appl. Phys. B*, 2011
- **A Study of the Global Chirp Dependence on the Interaction of Intense Colored Double Pulses with Clusters**  
N. X. Truong, S. Göde, J. Tiggesbäumker, and K. H. Meiwes-Broer, *Eur. Phys. J. D*, 2011 (in press)
- **Intense colored pulse trains: generation, characterization, and applications**  
N. X. Truong, J. Tiggesbäumker, and K. H. Meiwes-Broer, In *J. Opt.* **12**:115201, 2010
- **Shaper-assisted removal of the direction-of-time ambiguity in second-harmonic generation frequency-resolved optical gating**  
N. X. Truong, J. Tiggesbäumker, T. Döppner, In *Meas. Sci. Technol.* **21**:085303, 2010
- **Optimal control of the strong-field ionization of silver clusters in helium droplets**  
N. X. Truong, P. Hilse, S. Göde, A. Przystawik, T. Döppner, Th. Fennel, Th. Bornath, J. Tiggesbäumker, M. Schlanges, G. Gerber, and K. H. Meiwes-Broer, In *Phys. Rev. A* **81**:013201, 2010
- **Soft X-ray scattering using FEL radiation for probing near-solid density plasmas at few electron volt temperatures**  
S. Toleikis, R. R. Fäustlin, L. Cao, T. Döppner, S. Düsterer, E. Förster, C. Fortmann, S. H. Glenzer, S. Göde, G. Gregori, R. Irsig, T. Laarmann, H. J. Lee, B. Li, J. Mithen, K. -H. Meiwes-Broer, A. Przystawik, P. Radcliffe, R. Redmer, F.

- Tavella, R. Thiele, J. Tiggesbäumker, N. X. Truong, I. Uschmann, U. Zastra, and Th. Tschentscher, In *High Energy Density Phys.* **6**:15, 2010
- **Resolving the Ion and Electron Dynamics in Finite Systems Exposed to Intense Optical Laser Fields**  
J. Tiggesbäumker, T. Fennel, N. X. Truong, and K.-H. Meiwes-Broer, Chapter in *Metal-to-Nonmetal Transitions* (R. Redmer, F. Hensel, B. Holst, eds.), Springer Series in Materials Science **132**:85, 2010
  - **Soft X-Ray Thomson Scattering in Warm Dense Matter at FLASH**  
R. R. Fäustlin, S. Toleikis, Th. Bornath, L. Cao, T. Döppner, S. Düsterer, E. Förster, C. Fortmann, S. H. Glenzer, S. Göde, G. Gregori, A. Höll, R. Irsig, T. Laarmann, H. J. Lee, K. H. Meiwes-Broer, A. Przystawik, P. Radcliffe, R. Redmer, H. Reinholz, G. Röpke, R. Thiele, J. Tiggesbäumker, N. X. Truong, I. Uschmann, U. Zastra, and Th. Tschentscher, Chapter in *Ultrafast Phenomena XVI* (P. Corkum, S. Silvestri, K. A. Nelson, E. Riedle, R. W. Schoenlein, eds.), Springer Series in Chemical Physics **92**:241, 2009
  - **Bremsstrahlung and line spectroscopy of warm dense aluminum plasma heated by xuv free-electron-laser radiation**  
U. Zastra, C. Fortmann, R. R. Fäustlin, L. F. Cao, T. Döppner, S. Düsterer, S. H. Glenzer, G. Gregori, T. Laarmann, H. J. Lee, A. Przystawik, P. Radcliffe, H. Reinholz, G. Röpke, R. Thiele, J. Tiggesbäumker, N. X. Truong, S. Toleikis, I. Uschmann, A. Wierling, T. Tschentscher, E. Förster, and R. Redmer, In *Phys. Rev. E* **78**:066406, 2008
  - **Thomson scattering from near-solid density plasmas using soft X-ray free electron lasers**  
A. Höll, Th. Bornath, L. Cao, T. Döppner, S. Düsterer, E. Förster, C. Fortmann, S. H. Glenzer, G. Gregori, T. Laarmann, K.-H. Meiwes-Broer, A. Przystawik, P. Radcliffe, R. Redmer, H. Reinholz, G. Röpke, R. Thiele, J. Tiggesbäumker, S. Toleikis, N. X. Truong, T. Tschentscher, I. Uschmann, and U. Zastra, In *High Energy Density Phys.* **3**:120, 2007
  - **Charging of metal clusters in helium droplets exposed to intense femtosecond laser pulses**  
T. Döppner, Th. Diederich, A. Przystawik, N. X. Truong, Th. Fennel, J. Tiggesbäumker, and K.-H. Meiwes-Broer, In *Phys. Chem. Chem. Phys.* **9**:4639, 2007

## B In Preparation



- **Systematically Shaped Laser Pulses for Intense Laser-Cluster Studies**  
N. X. Truong, S. Göde, J. Tiggesbäumker, and K. H. Meiwes-Broer, to be submitted to *J. Phys. B: At. Mol. Opt. Phys.*
- **Charge State Bleaching in Intense Laser-Cluster Interactions**  
N. X. Truong, S. Göde, J. Tiggesbäumker, and K. H. Meiwes-Broer, to be submitted to *New. J. Phys.*
- **Magnetization dynamics of thin Fe-films after ultrashort laser excitation**  
S. Polei, N. X. Truong, J. Tiggesbäumker, K. H. Meiwes-Broer, and A. Kleibert, in preparation
- **Appearance Intensity Thresholds in Intense Laser-Cluster Interactions**  
N. X. Truong, Ch. Peltz, Th. Fennel, S. Göde, J. Tiggesbäumker, and K. H. Meiwes-Broer, in preparation

## C Other Publications

- **Setup and characterization of a high-dynamic range, third-order correlator for 1 kHz laser system**  
N. X. Truong, Master's thesis, at the Institute of Optics and Quantum Electronics, Friedrich-Schiller-University Jena, 2004

# Curriculum vitae

## Personal Information

Name: Nguyen Xuan Truong  
Date of birth: August 9<sup>th</sup> 1978 in Hai Duong-Vietnam

## Education and training

1993–1996      Gifted high-school of Hai Duong, Vietnam

1996–2000      Student of physics at Hanoi Pedagogic University, Vietnam  
Bachelor of Science with the theoretical work:  
*Studying resistance of metals using pseudopotential methods.*

2002–2004      Student of physics at the FSU-Jena, Germany  
Diplom in physics with the experimental work:  
*Setup and characterization of a high-dynamic range, third-order correlator for 1 kHz laser system,*  
at the Institute of Optics and Quantum Electronics, FSU-Jena.

2004-2005      Researching assistant at the group of Prof.Dr.Dr.h.c. Sauerbrey,  
at the Institute of Optics and Quantum Electronics, FSU-Jena.

2005-present    PHD-student of Physics at the University of Rostock, Germany  
Researching assistant at the group of Prof.Dr. Meiwes-Broer.

# Erklärung

Ich erkläre hiermit ehrenwörtlich, dass ich die vorliegende Arbeit selbständig angefertigt und ohne fremde Hilfe verfasst habe, keine außer den von mir angegebenen Hilfsmitteln und Quellen dazu verwendet habe und die den benutzten Werken inhaltlich und wörtlich entnommenen Stellen als solche kenntlich gemacht habe.

Rostock, den 29.12.2010

---

Nguyen Xuan Truong



# Acknowledgements

A long journey to the *title* since 2002 has come to a happy ending. This is a great opportunity to express my respect to all individuals, friends and colleagues, who have assisted me all along, one way or another.

I would like first to thank Dr. Tran Anh Vu, Dr. H.-G. Walther, and Prof. R. Sauerbrey for the chance to join the Master's program in FSU Jena and to work in the ultrashort laser laboratories at the Institute of Optics and Quantum Electronics. I have learnt a lot of experimental skills, e.g., in nonlinear optics, laser physics, as well as femtosecond pulse shaping. Within this context, I also would like to acknowledge the Vietnam Overseas Scholarship Program for the respective financial support.

For the PHD-project, most thanks should go to Prof. K. H. Meiwes-Broer, my dissertation advisor, who found me in hard life that time in May, 2005. Prof. Meiwes-Broer gave me a job, a new sweet home, and a brightest future ever, as I now can say. I am deeply indebted for the possibility to develop my scientific knowledge in his group in Rostock, to do what I am really interested in, and to fulfill my great dream since I was still a young boy listening to lectures of physics at school in Vietnam. Once, when he was so excited with the very first optimal control measurements on clusters at about midnight, he bought me a meal from the Vietnamese restaurant nearby so that I could keep experiments going on to the next morning.

During my stay in the group, I am very pleased to thank Dr. Josef Tiggesbäumker, my beloved group's leader, for his continuous support and fruitful discussions, and for sharing great ideas. I greatly appreciate his sympathy and patience of explaining things in detail. I have learnt a lot from him, not only in science but also in life. I loved to join his family and colleagues, doing BBQ and cheering on the German football team at the EU- or World cups.

I thank Dr. Tilo Döppner for his support from the beginning of the PHD-time and his interest in my work after his move to Livermore. I must acknowledge Dr. Andreas Przystawik and, especially, to Sebastian Göde for preparing the clusters, and maintaining the source healthy, as well as numerous help by the experiments. Many thanks go to Robert Irsig for coworking on the laser system and interesting discussions. I would like to express appreciation to the whole Clusters and Nanostructures group for the friendly working environment and nice experiences together in the laboratories. Some of those are Andreas, Sebastian, Johannes, Christian, Robert, and Slawomir. Technical helps by Jan Dittrich and the workshop-team led by Mr. Tofaute, as well as official assistances from Mrs. Schädel are very much appreciated.

I am very grateful for the cooperation, support, and interest of Prof. G. Gerber, Prof. Th. Fennel, Prof. G. Röpke, Prof. M. Schlanges, Dr. P. Hilde, Dr. Th. Bornath, and Dr. A. Kleibert. Professional collaboration within the project "Thomson scattering and correlations in warm dense matter" meant a great deal to me. Simulations performed by

groups of Prof. Th. Fennel and Prof. M. Schlanges have also made important contributions to the analysis of the results in this dissertation. By introducing me to visit his group at the university of Würzburg, Prof. G. Gerber marked a crucial influence on my work. I have benefited very much after getting to know about the research there.

I wish to thank my senior friend Herbert, a wonderful kind person, who has really cared about me in everyday life. He has been with me everywhere, and taught me playing table tennis to keep me fit for several day-and-night shifts of experiments. With him my life has become much better than ever. Besides, I should thank the Vietnamese student group in Rostock, who have shared with me *thick and thin* moments in personal life. With them by my sides I am distracted from homesick for being alone abroad a long time.

Special thanks go to Thanh Nga, who means a lot to me. She showed me the world, taught me how to sense things, and encouraged me in doing research. I could not remember exactly how many times she stayed up all night with me (online), when I did experiments alone in the labs.

Last but never the least, I am pleased to thank all members of my big family in Vietnam for their patience, forbearance and belief. My parents have continuously inspired me a lot to science, with their love and wishes. They have no idea about research. But they know for sure that science is something good for life, and they have worked hard to be able to support me on my way. Absolutely, this dissertation is dedicated to them, to their lifelong dreams.